THEORETICAL LIMITS OF LUNAR VISION AIDED NAVIGATION WITH INERTIAL NAVIGATION SYSTEM

THESIS

David W. Jones, Capt, USAF

AFIT-ENG-MS-15-M-020

DEPARTMENT OF THE AIR FORCE
AIR UNIVERSITY

AIR FORCE INSTITUTE OF TECHNOLOGY

Wright-Patterson Air Force Base, Ohio

AFIT-ENG-MS-15-M-020

THEORETICAL LIMITS OF LUNAR VISION AIDED NAVIGATION WITH INERTIAL NAVIGATION SYSTEM

THESIS

Presented to the Faculty
Department of Electrical and Computer Engineering
Graduate School of Engineering and Management
Air Force Institute of Technology
Air University
Air Education and Training Command
in Partial Fulfillment of the Requirements for the
Degree of Master of Science in Electrical Engineering

David W. Jones, B.S.E.E.
Capt, USAF

March 2015

AFIT-ENG-MS-15-M-020

THEORETICAL LIMITS OF LUNAR VISION AIDED NAVIGATION WITH INERTIAL NAVIGATION SYSTEM

THESIS

David W. Jones, B.S.E.E.
Capt, USAF

Committee Membership:

Dr. K.J. Kauffman
Chair

Dr. J.F. Raquet
Member

Maj M. D. Seal
Member

AFIT-ENG-MS-15-M-020

Abstract

The precision navigation capabilities of the Global Positioning System (GPS) are used extensively within US military operations. However, GPS is highly vulnerable to intentional and unintentional external interference. Therefore, a need exists to develop a non-GPS precision navigation method to operate in GPS degraded environments. This research effort presents the theoretical limits of a precision navigation method based on an inertial navigation system (INS) aided by angle measurements with respect to lunar surface features observed by a fixed camera. To accomplish this task, an extended Kalman filter (EKF) was implemented to estimate INS drift errors and bring in simulated lunar feature angle measurements to correct error estimates. The research scope focused solely on the feasibility of lunar vision aided navigation with INS where only measurement noise effects from a simulated CCD camera and barometer were considered. Various scenarios based on camera specifications, lunar feature quantity, INS grade, and lunar orbital parameters were conducted to observe the INS drift correction by lunar feature angle measurements. The resulting trade spaces presented by the scenarios showed theoretical substantial improvement in the navigation solution with respect to a stand alone INS.

AFIT-ENG-MS-15-M-020

I would first like to thank Jesus, my fixed star. Secondly, thank you to Dr. Kauffman for his patience and excellent mentorship in advising me through this research effort. I would also like to thank Col Grondin for her support in allowing me to have this amazing opportunity. A thank you to Mr. Brian Roadruck and Capt James Kawecki for their teamwork and steadfast support given in times when encouragement was needed. Lastly, thank you to my parents for their ever present rallying; impressing upon me a drive to advance even when the trials become rough. Thank you.

Table of Contents

List of Figures

Figure Page

Figure Page

Figure Page

THEORETICAL LIMITS OF
LUNAR VISION AIDED NAVIGATION
WITH INERTIAL NAVIGATION SYSTEM

I. Introduction

1.1 Purpose

The development of non-Global Positioning System (GPS) based precision navigation methods is vitally important. This is due to GPS's high vulnerability to intentional and unintentional external interference coupled with the US military's heavy reliance on GPS. The following research develops the theoretical limits of a navigation method integrating inertial sensors and lunar feature angle measurements. The goal is to provide immutable, robust, self-contained, autonomous precision navigation in GPS degraded environments.

Since ancient times, the ability to travel from one's present location to an intended destination has been practiced on land and sea [28]. Over time, this ability and its associated methods became the field of study called *navigation* derived from the Latin word *navis* for sea faring ship [3][12]. Of the ancient navigation methods employed, around two millennia ago, the Polynesians are known to have developed a form of celestial navigation whereby determining one's position based on careful observation of celestial bodies [28]. The Chinese and the Italians are recorded to have independently developed the compass during the 12th and 13th centuries CE [28][34]. Later developments in celestial navigation techniques in Europe during the

18th century allowed for latitude and longitude to be estimated with the development of the sextant and the chronometer respectively [34].

Technological advances around the beginning of the 20th century brought about new possibilities for precision navigation methods. New understanding behind rotational motion and acceleration paved the way for navigation based upon inertial measurements in the form of an inertial navigation system (INS) [28]. The manipulation of radio waves in the 1930s proved that navigation by radio waves was another viable method of navigation known as the American long range navigation system (Loran) [9].

With the advent of the space age in the 1950s, the US and Soviet Union realized the capability to navigate by their own manufactured celestial bodies (or satellites) rather than rely on natural celestial bodies (e.g. moon and stars). The navigation satellite constellation developed by the US was known as Navstar GPS. The first GPS satellite was launched in 1978 [9]. The core positioning methodology of GPS is based upon streaming and receiving transmitted GPS signals from the satellite constellation to ground receivers [12]. The detected timing differences due to the signal propagation from satellite transmitter to a ground based receiver can be multiplied by the speed of light to get a pseudorange [12]. A pseudorange is a range containing error from the ground based receiver's position to the satellite transmitter's position [12]. A position fix can be attained from knowing the receiver's respective timing of received signals in relation to at least four satellites [9].

The Gulf War in 1991 acted as the debut of GPS in an armed conflict through the use of GPS based precision guided munitions and ground unit navigation [25]. GPS's level of precision and robust navigation qualities are said by McLendon to have enabled the "left hook" maneuver by Coalition forces which destroyed the Iraqi armored divisions [22]. By the end of the 20th century, GPS had become an integral navigation system for the US military [27]. GPS was not without fault and weakness. Over time, the system has been found to be degraded in certain circumstances. Urban canyons and jamming systems are known to subdue the effect of GPS in said areas [9][12]. Thus, the need to counter such weakness exists and can be achieved through the development of other navigation means independent of GPS.

1.2 Problem Statement

This research effort assumes GPS has been degraded and other means of trajectory estimation are required for an aircraft to properly navigate. Trajectory is defined as the position, velocity, and attitude of a vehicle over time [30].

The non-GPS precision navigation system chosen for this research effort is an INS. An INS performs *dead reckoning* navigation meaning that a trajectory estimate can be made based on an INS's initial position in combination with direction and speed measurements [28]. Direction and speed measurements are given by accelerometers and gyroscopes which are inertial sensors within an INS. Accelerometers measure specific forces acting upon a vehicle body and gyroscopes measure changes in rotational velocity also with respect to a vehicle body [28]. INSs are highly accurate for short time periods but accumulate drift error for an extended time length [5]. An optical sensor with a view of the Moon can provide aiding angular measurements to decrease the accumulated drift error in the INS.

The goal of this research effort is to explore the theoretical improvement upon an INS estimated trajectory aided by angular measurements with respect to lunar features observed by a camera. The improvement of the trajectory estimation will be measured in terms of the reduction of position state errors over time. The aircraft trajectory, INS errors, lunar features, and optical sensor measurements will be simulated.

1.3 Research Contributions

The following are the research contributions for this thesis:

1. Model the drift errors for an INS (commercial, tactical, and navigation grade).
2. Construct a model of an Earth-based aircraft trajectory with features simulated at lunar surface locations.
3. Simulate INS drift errors aided by lunar feature angle measurements to demonstrate a decrease in trajectory error over various scenarios where measurement noise effects are only considered (e.g. INS grade, pixel size, lens focal length, feature quantity, and lunar distance and geometry).

As only measurement noise effects upon the system are considered within this research effort, the results in Chapter 4 are not indicative of realistic lunar vision aided navigation with INS. However, the results present plausible trade spaces for lunar vision aided navigation with INS that exist with respect to the various scenario parameters mentioned above in the research contributions.

1.4 Research Assumptions

To limit the scope of the research effort to consider only measurement noise effects upon lunar vision aided navigation with INS, the following simplifying assumptions were made:

1. The lunar feature angular measurements observed by the camera were modeled with unbiased Gaussian white noise. This research effort does not include the more complicated error contained in more realistic feature extraction and matching techniques such as the Scale Invariant Feature Transform algorithm (SIFT).

2. In a realistic scenario, there will be error in the camera alignment with respect to the local navigation frame. However, in this research effort, it is assumed that the alignment to the horizon and/or fixed stars was available and known. Therefore, the camera alignment error was not included.

3. The camera was modeled as fixed to the vehicle body. For a dynamic vehicle, this scenario would typically induce feature smearing over the duration of the camera exposure. However, this affect was not considered in the scope of this research, as wings-level flight was assumed.

4. All objects are assumed to be in the camera's field of view. In a realistic scenario, the effects of wide field of view optics or multiple optics would need to be considered.

1.5 Thesis Overview

The following section outlines the remainder of this thesis. Chapter 2 proceeds through the mathematical basis behind the research and discusses alternative current methods of non-GPS navigation and feature extraction. Chapter 3 presents the methodology of how the research was conducted and the specific mathematical models that were incorporated. Chapter 4 shows the results of the trajectory estimation based on an INS aided by lunar feature angle measurements. Chapter 5 presents the conclusion and suggestions for future work on this subject.

II. Background

2.1 Introduction

The following section discusses the theory and various techniques supporting inertial navigation integrated with lunar feature angle measurements. Section 2.2 presents mathematical notation and constructs. Section 2.3 lays out the frames of reference and how they will be annotated. Section 2.4 discusses the Kalman Filter, Extended Kalman Filter, and error state estimation. Section 2.5 covers computer vision and camera projection theory. Section 2.6 covers the Sun, Moon, and Earth's orbital parameters as well as a brief description of the lunar surface features. Section 2.7 presents the literature review covering various image-aided navigation techniques and current use of natural passive signals to gain navigation information. Lastly, Section 2.8 summarizes the topics discussed in this Chapter.

2.2 Arithmetic Notation

The following notation will be used for the rest of this thesis:

- Upper and lower case italicized letters are representative of scalar variables.
- Bold lower case letters represent arrays.
- Upper case rectified letters denote a cartesian coordinate axis.
- Bold upper case letters represent matrices.
  - $\mathbf{I}$ is an identity matrix with 3 rows and 3 columns.
  - A zero $\mathbf{0}$ in bold font is a symbol for a 3 rows by 3 columns matrix of zeros.
  - T as a superscript of a matrix or an array denotes a transpose, i.e. $\mathbf{A}^{\mathrm{T}}$.

  - Direction Cosine Matrices (DCM) are matrices containing information which is used to move a vector from one frame of reference to another. DCMs are represented in the matrix notation form with a bold upper case letter containing a superscript and a subscript variable as shown in Equation 2.1 [28]. The subscript variable n is the current frame of reference. The superscript variable b is the reference frame to be transitioned to. By transposing a DCM, the transition from one frame to another is reversed as in Equation 2.2 where the transition from the n-frame to the b-frame is reversed. Section 2.3 provides an explanation for the frames of reference used in this research effort.

$$\mathbf{C}_{\mathrm{n}}^{\mathrm{b}} \tag{2.1}$$

$$\mathbf{C}_{\mathrm{b}}^{\mathrm{n}} = (\mathbf{C}_{\mathrm{n}}^{\mathrm{b}})^{\mathrm{T}} \tag{2.2}$$

- Skew symmetric matrices are matrices populated by the elements of a single vector or array [28]. An array variable next to a × symbol is representative of a skew symmetric matrix. Specifically, in this research effort, a skew symmetric matrix is shown as a 3 rows by 3 columns matrix formed from the elements of a 3 rows by 1 column vector as shown in Equations 2.3 and 2.4.

$$\boldsymbol{\gamma} = \begin{bmatrix} \gamma_1 \\ \gamma_2 \\ \gamma_3 \end{bmatrix} \tag{2.3}$$

$$\boldsymbol{\gamma}\times = \begin{bmatrix} 0 & -\gamma_3 & \gamma_2 \\ \gamma_3 & 0 & -\gamma_1 \\ -\gamma_2 & \gamma_1 & 0 \end{bmatrix} \tag{2.4}$$

2.3 Reference Frames

In navigation, distinct frames of reference are needed to explain an aircraft's trajectory with respect to different origin points. The following subsections discuss each frame used in this research effort as described in [28].

Earth Centered Inertial Frame (i-frame).

The i-frame is a cartesian coordinate reference frame with origin centered at the Earth's center $\mathrm{O_i}$. The three axes within the coordinate system are non-rotating being considered fixed to the stars [28]. Figure 2.1 shows the three axes as solid black lines with axes denoted with the subscript i. The Z-axis is pointed through the Earth's north pole, the X-axis is pointed through the Earth's equator towards the star Aries, and the Y-axis points perpendicular to the X-axis vector along the Earth's equator plane [28].

Earth Centered Earth Fixed Frame (ECEF) (e-frame).

The e-frame is a cartesian coordinate reference frame with origin fixed at the Earth's center $\mathrm{O_e}$ as shown in Figure 2.1. The e-frame axes are denoted by a subscript e. The Z-axis lies through the center of the Earth and the poles shared by the i-frame Z-axis. The X-axis lies perpendicular to the Z-axis through the center of the Prime Meridian, and the Y-axis lies at longitude 90°E pointing through the Earth's equator [30]. The X and Y axes rotate around the Z-axis at the Earth's rate of rotation (Ω), which is $7.292115 \times 10^{-5} \frac{\mathrm{rad}}{\mathrm{s}}$ (WGS-84) [28].

Earth Fixed Navigation Frame (n-frame).

The n-frame is a three dimensional (3D) cartesian coordinate reference frame that is aligned to the local area directions of north, east, and down (NED) forming a plane tangent to the Earth's surface [30]. The down direction corresponds to the direction of the Earth's gravity towards the center of the Earth. In this research effort, the orientation of the n-frame is fixed to the aircraft's trajectory starting position. Figure 2.1 illustrates the n-frame axes with a subscript n. The n-frame origin is at $\mathrm{O_n}$ along the Earth's surface.

Body Frame (b-frame).

The b-frame follows a 3D cartesian coordinate system. Figure 2.2 presents an aircraft body with the origin at the vehicle body center $\mathrm{O_b}$ [28]. The body frame axes are denoted by a subscript b. The X-axis corresponds to the roll axis and points through the nose of the vehicle body. The Y-axis corresponds to the aircraft pitch and points through the aircraft wing direction. The Z-axis is tied to the aircraft yaw and points vertically through the center of the aircraft.

Sensor Frame (s-frame).

The s-frame is a reference frame constructed on the orientation of a sensor (CCD camera) fixed to the aircraft body. Figure 2.3 shows the sensor with the origin at $\mathrm{O_s}$. For this research effort, the sensor will be fixed to the b-frame with the lens and Z-axis pointed towards the sky to view the Moon. The X and Y axes point perpendicularly to each other along a plane parallel to the image plane. The three sensor axes are denoted by a subscript s.

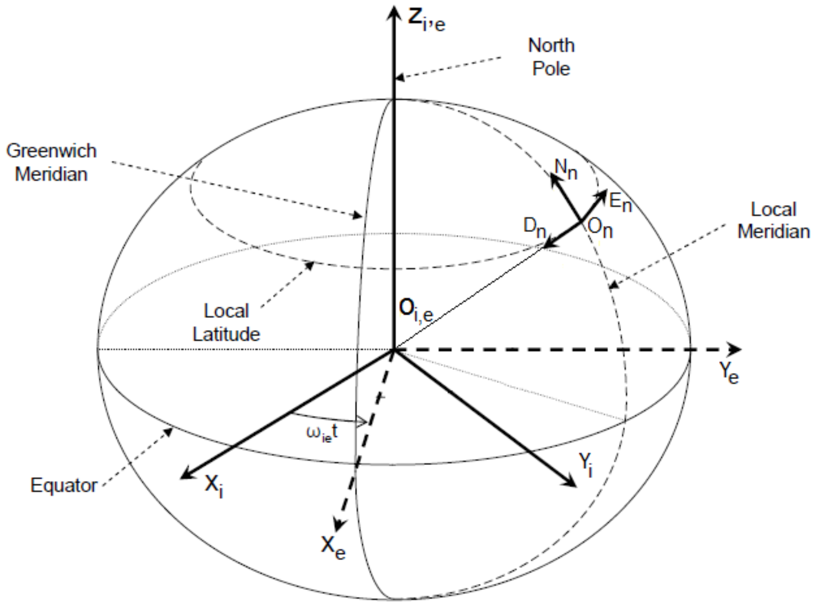

Figure 2.1. ECEF and Navigation Frames. Used with permission [30].

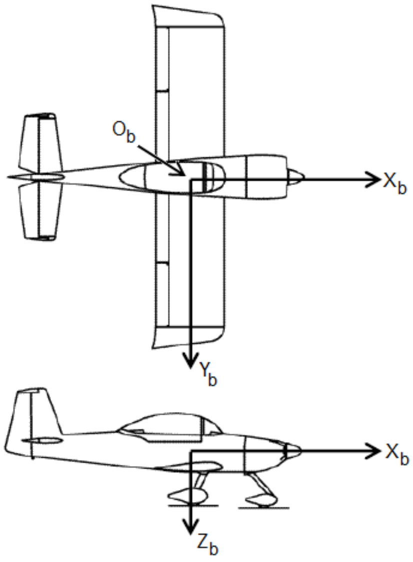

Figure 2.2. Vehicle Body Frame. Used with permission [30].

Figure 2.3. Sensor Frame.

2.4 Estimation

Estimation is the process by which an unknown quantity can be predicted within a margin of error [20]. The following subsections discuss dynamic systems, the Kalman Filter (KF), the Extended Kalman Filter (EKF), and error state estimation.

Dynamic Systems.

Equation 2.5 represents a time invariant dynamic system in the form of a linear differential equation characterized by continuous time [5][20]. The dynamic system models state behavior as it is propagated over time [5]. A state is a phenomena of interest, e.g. position, velocity, or attitude [5]. $\mathbf{F}\mathbf{x}(t)$ in Equation 2.5 represents the states mapped to the dynamic system where $\mathbf{x}(t)$ is the state vector and $\mathbf{F}$ is the state mapping matrix. $\mathbf{Bu}(t)$ represents the system inputs mapped onto the dynamic system where $\mathbf{u}(t)$ is the system input vector and $\mathbf{B}$ is the system input mapping matrix [20]. $\mathbf{Gw}(\mathrm{t})$ represents the system noise where $\mathbf{w}(t)$ is the noise vector and $\mathbf{G}$ is the system noise mapping matrix. Equation 2.6 presents $\mathbf{Q}(t)$ as the input noise covariance matrix where the Dirac delta function is represented by $\delta(t)$ [21][30].

$$\dot{\mathbf{x}}(t) = \mathbf{Fx}(t) + \mathbf{Bu}(t) + \mathbf{Gw}(t) \tag{2.5}$$

$$\mathbf{Q}(t)\delta(\tau) = \mathrm{E}\left[\mathbf{w}(t)\mathbf{w}^{\mathrm{T}}(t+\tau)\right] \tag{2.6}$$

Equation 2.7 represents the state uncertainty where $\mathbf{P}(t)$ is the state covariance matrix. The state covariance propagation equation is shown in Equation 2.8 [20].

$$\mathbf{P}_{\mathbf{xx}}(t) = \mathrm{E}\left[\mathbf{x}(t)\mathbf{x}^{\mathrm{T}}(t)\right] \tag{2.7}$$

$$\dot{\mathbf{P}}_{\mathbf{xx}}(t) = \mathbf{FP}_{\mathbf{xx}}(t) + \mathbf{P}_{\mathbf{xx}}(t)\mathbf{F}^{\mathrm{T}} + \mathbf{GQ}(t)\mathbf{G}^{\mathrm{T}} \tag{2.8}$$

Equations 2.9-2.12 represent the continuous dynamic system from Equations 2.5 and 2.8 brought into discrete form. This conversion is needed, because the EKF algorithm used in this research effort operates in discrete time [5]. For the rest of this thesis, all discrete form equations hold a time step of $(\Delta t)_k$ where k is the time step index number. In Equations 2.9 and 2.10, $\mathbf{\Phi}$ is the state transition matrix and $\mathbf{Q}_{\mathrm{d}}$ is the discrete input noise covariance matrix respectively [5][20]. Equation 2.11 shows the discrete propagation of the state mean and Equation 2.12 shows the discrete propagation of the state variance.

$$\mathbf{\Phi} = e^{\mathbf{F}(\Delta t)_k} \tag{2.9}$$

$$\mathbf{Q}_{\mathrm{d}} = \mathrm{E}\left[\mathbf{w}_k \mathbf{w}_k^{\mathrm{T}}\right] \tag{2.10}$$

$$\mathbf{x}_k = \mathbf{\Phi}\mathbf{x}_{k-1} + \mathbf{w}_k \tag{2.11}$$

$$\mathbf{P}_k = \mathbf{\Phi}\mathbf{P}_{k-1}\mathbf{\Phi}^{\mathrm{T}} + \mathbf{Q}_{\mathrm{d}} \tag{2.12}$$

Kalman Filter.

The KF is a recursive algorithm that performs minimum mean square error (MMSE) estimation of state dynamics [5]. The KF's algorithm design assumes a Gaussian distribution for the state dynamics to be estimated. This assumption allows the filter to completely describe a state's dynamics by estimating the state's mean and variance or uncertainty [5]. Three components comprise the KF: the propagation phase in Equations 2.13 and 2.14, the measurement model in Equation 2.15, and the update phase shown in Equations 2.18-2.20.

Propagation Phase.

The propagation phase is comprised of propagating the state mean $\hat{\mathbf{x}}_k$ and variance $\mathbf{P}_k$ estimates through discrete time steps. When no measurement update is present, the propagation equations recursively use the previous state mean $\hat{\mathbf{x}}_k^-$ and variance $\mathbf{P}_k^-$ estimates to obtain its current estimation of the state mean $\hat{\mathbf{x}}_k^+$ and variance $\mathbf{P}_k^+$ as shown in Equations 2.13 and 2.14 [5].

$$\hat{\mathbf{x}}_k^- = \mathbf{\Phi}\hat{\mathbf{x}}_{k-1}^+ + \mathbf{w}_k \tag{2.13}$$

$$\mathbf{P}_k^- = \mathbf{\Phi}\mathbf{P}_{k-1}^+\mathbf{\Phi}^{\mathrm{T}} + \mathbf{Q}_{\mathrm{d}} \tag{2.14}$$

Measurements.

KF estimation operates through the introduction of sensor measurements $\mathbf{z}_k$ into the filter at specified discrete times [5]. The measurements aid the filter by providing information about the states. Equation 2.15 below is characteristic of a linear measurement model [5]. $\mathbf{H}_k\mathbf{x}_k$ represents the relationship between the sensor and the states where $\mathbf{H}_k$ is the measurement matrix. The level of information to which the sensor knows about the states is dependent upon the sensor specifications denoted by the state observability quantities in $\mathbf{H}_k$ [5]. The measurement noise $\mathbf{v}_k$ is assumed to be white Gaussian noise. Equation 2.16 is the measurement noise covariance matrix $\mathbf{R}_k$.

$$\mathbf{z}_k = \mathbf{H}_k\mathbf{x}_k + \mathbf{v}_k \tag{2.15}$$

$$\mathbf{R}_k = \mathrm{E}\left[\mathbf{v}_k\mathbf{v}_k^{\mathrm{T}}\right] \tag{2.16}$$

Update Phase.

The final component of the KF algorithm is the update phase. During the update phase, aiding measurements $\mathbf{z}_k$ are input into the algorithm to bring about an optimal estimate of the state mean and variance. The criterion held to determine an optimal estimate within the KF is an estimate with minimal mean square error $\mathbf{P}_k$ [5]. To achieve this aim, an estimator based upon Bayes rule is used where the optimal estimate $\hat{\mathbf{x}}_k^+$ of the states $\mathbf{x}_k$ is conditioned on the measurement $\mathbf{z}_k$ [5].

$$\hat{\mathbf{x}}_k^+ = \mathrm{E}(\mathbf{x}_k|\mathbf{z}_k) \tag{2.17}$$

Based on the above Bayesian estimator, the associated updated mean and covariance equations are shown in Equations 2.18-2.20 where $\mathbf{K}_k$ is the Kalman gain. The Kalman gain is a blending factor that works to blend the measurement with the *a* *priori* state estimate to bring about the optimal updated estimate [5].

$$\hat{\mathbf{x}}_k^+ = \hat{\mathbf{x}}_k^- + \mathbf{K}_k(\mathbf{z}_k - \mathbf{H}_k\hat{\mathbf{x}}_k^-) \tag{2.18}$$

$$\mathbf{P}_k^+ = (\mathbf{I} - \mathbf{K}_k\mathbf{H}_k)\mathbf{P}_k^- \tag{2.19}$$

$$\mathbf{K}_k = \mathbf{P}_k^-\mathbf{H}_k^{\mathrm{T}}(\mathbf{H}_k\mathbf{P}_k^-\mathbf{H}_k^{\mathrm{T}} + \mathbf{R}_k)^{-1} \tag{2.20}$$

Extended Kalman Filter.

A modified KF algorithm called an EKF is designed to process non-linear measurement models [5]. Equations 2.21-2.26 represent the EKF algorithm [5]. The propagation phase consists of Equations 2.21 and 2.22 which are the estimated state mean and variance propagation equations respectively. Equation 2.21 shows the states propagated by a non-linear function $\mathbf{f}(\hat{\mathbf{x}}_k)$ [21]. The EKF covariance propagation equation in Equation 2.22 holds the same form as the KF covariance propagation equation in Equation 2.14.

$$\hat{\mathbf{x}}_k^- = \mathbf{f}(\hat{\mathbf{x}}_{k-1}^+) \tag{2.21}$$

$$\mathbf{P}_k^- = \mathbf{\Phi}\mathbf{P}_{k-1}^+\mathbf{\Phi}^{\mathrm{T}} + \mathbf{Q}_d \tag{2.22}$$

The EKF update phase consists of Equations 2.23 and 2.24. The residual holds a non-linear function $\mathbf{h}(\hat{\mathbf{x}}_k)$ in Equation 2.23 within its calculation [21]. The Kalman gain $\mathbf{K}_k$ in both equations is the same form as the Kalman gain equation in the KF algorithm shown in Equation 2.20. The covariance update equation in Equation 2.24 holds the same form as the covariance update equation in the KF algorithm in Equation 2.19. The form of the linear measurement matrix $\mathbf{H}_k$ accommodating the non-linear measurement function will be presented in Equation 2.26.

$$\hat{\mathbf{x}}_k^+ = \hat{\mathbf{x}}_k^- + \mathbf{K}_k(\mathbf{z}_k - \mathbf{h}(\hat{\mathbf{x}}_k^-)) \tag{2.23}$$

$$\mathbf{P}_k^+ = (\mathbf{I} - \mathbf{K}_k\mathbf{H}_k)\mathbf{P}_k^- \tag{2.24}$$

The measurement model for an EKF is likewise non-linear as shown in Equation 2.25. The linear mapping of the state observabilities onto the state estimate vector $\mathbf{H}_k\hat{\mathbf{x}}_k$ within the KF algorithm is replaced by passing the estimated states through a non-linear function $\mathbf{h}(\hat{\mathbf{x}}_k)$ which holds information about the states [5][21].

$$\mathbf{z}_k = \mathbf{h}(\mathbf{x}_k) + \mathbf{v}_k \tag{2.25}$$

To process the non-linear measurement function $\mathbf{h}(\hat{\mathbf{x}}_k)$ through the EKF, the non-linearity of the function must be accounted for as the EKF algorithm requires a linear measurement matrix $\mathbf{H}_k$ when calculating the Kalman gain $\mathbf{K}_k$ and updated variance estimate $\mathbf{P}_k^+$ as shown in Equations 2.20 and 2.24 respectively [21]. During the update phase, a method is used to linearly approximate around the non-linear measurement function $\mathbf{h}(\hat{\mathbf{x}}_k)$ to approximate $\mathbf{H}_k$. A linear approximation of a non-linear function can be found through the use of a first-order Taylor series expansion known as a Jacobian which consists of partial differentiation applied to the non-linear measurement function as seen in Equation 2.26 [21].

$$\mathbf{H}_k = \frac{\partial}{\partial \hat{\mathbf{x}}_k}\mathbf{h}(\hat{\mathbf{x}}_k) \tag{2.26}$$

Error States.

So far, modeling and estimation has been discussed with regard to direct states $\mathbf{x}_k$. In the case of an INS, the system performance is characterized by the amount of trajectory drift error over time [28]. Thus, modeling of the INS error states $\delta\mathbf{x}_k$ are more suitable for the INS design. Also, a relationship can be constructed between the errors $\delta\mathbf{x}_k$, errant truth $\mathbf{x}_{\text{INS},k}$, and true states $\mathbf{x}_k$ as shown in Equation 2.27 [5][21].

Lastly, the error states can be modeled in the same way as the direct states just by modifying the state vector $\mathbf{x}_k$ to incorporate state errors as shown in Equation 2.28 [28].

$$\mathbf{x}_k = \mathbf{x}_{\text{INS},k} + \delta\mathbf{x}_k \tag{2.27}$$

$$\delta\mathbf{x}_k = \mathbf{\Phi}\delta\mathbf{x}_{k-1} + \mathbf{w}_k \tag{2.28}$$

2.5 Computer Vision

This section provides an overview of basic optical sensor configuration, camera projection theory, angular field of view, and angular resolution within diffraction limited systems.

Camera Projection Theory.

Figure 2.4 illustrates a pinhole camera model. Light reflected or projected from objects in the scene of the outside world is taken in by the aperture (or opening) shaped as a double convex lens into a dark space where the image is projected [10]. Based upon the behavior of light rays entering the aperture, the image is naturally an inverted projection of the outside scene [10]. Depending on the focal length f, the projected arrow image can be manipulated. A large focal length will create a magnified image of the scene with a small field of view. A small focal length will cause the scene to be viewed from a wide field of view. Equation 2.29 shows the relationship between the scene, image, and focal length where s_1 is the distance from the scene to the aperture and s_2 is the distance from the lens to the projected scene [10].

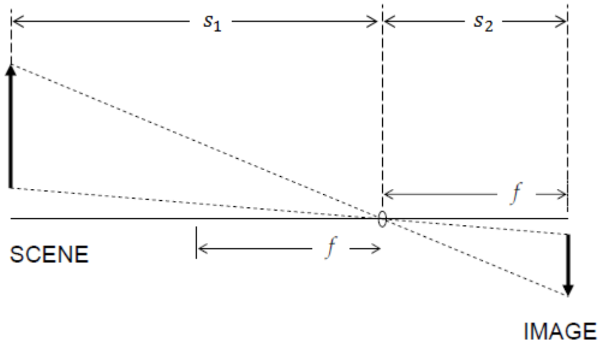

Figure 2.4. Pinhole Camera Model. Used with permission [30].

$$\frac{1}{s_1} + \frac{1}{s_2} = \frac{1}{f} \tag{2.29}$$

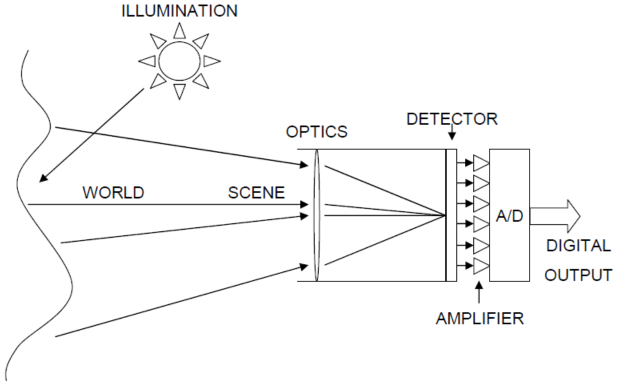

Figure 2.5. Optical Sensor Model. Used with permission [30].

Figure 2.5 follows the pinhole camera concepts presented in Figure 2.4, but builds upon the model's analog aspects with an analog-to-digital interface converting raw images of the outside world scene into digital information a computer can use to reconstruct the image. Within Figure 2.6, the image projection from Figure 2.4 is placed in the context of the 3D outside scene projected onto a 2D image plane. In Figure 2.6, $\mathbf{s}^{\mathrm{c}}$ is the object location in the outside scene and $\mathbf{s}^{\mathrm{proj}}$ is the object location on the 2D projection [30]. The 2D image axes are represented by a 2D cartesian coordinate system with x_{proj} and y_{proj} as the horizontal and vertical axes respectively. The relationship between the object location in the 3D scene $\mathbf{s}^{c}$ and the object projection on to the image $\mathbf{s}^{proj}$ is shown in Equation 2.30 where z_c is the direction from the camera to the 3D scene.

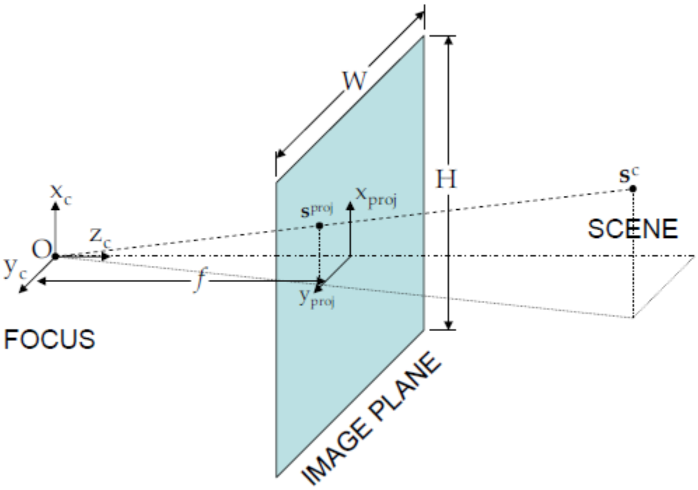

Figure 2.6. Camera Projection Model. Used with permission [30].

$$\mathbf{s}^{\text{proj}} = \left(\frac{f}{\mathbf{s}^{\text{c}}_{\text{z}}}\right)\mathbf{s}^{\text{c}} \tag{2.30}$$

The object projection location needs to be determined with respect to pixel locations in the digital image as shown in Equation 2.31 [30]. M and N serve as the digital array horizontal and vertical axes respectively of width W and height H. Figure 2.7 shows the 2D digital image array coordinate system relating the projected object location $\mathbf{s}^{proj}$ coordinates onto the digital image array coordinate system [30].

$$\mathbf{s}^{\text{pix}} = \begin{bmatrix} -\frac{M}{H} & 0 & 0 \\ 0 & \frac{N}{W} & 0 \end{bmatrix} \mathbf{s}^{\text{proj}} + \begin{bmatrix} \frac{M+1}{2} \\ \frac{N+1}{2} \end{bmatrix} \tag{2.31}$$

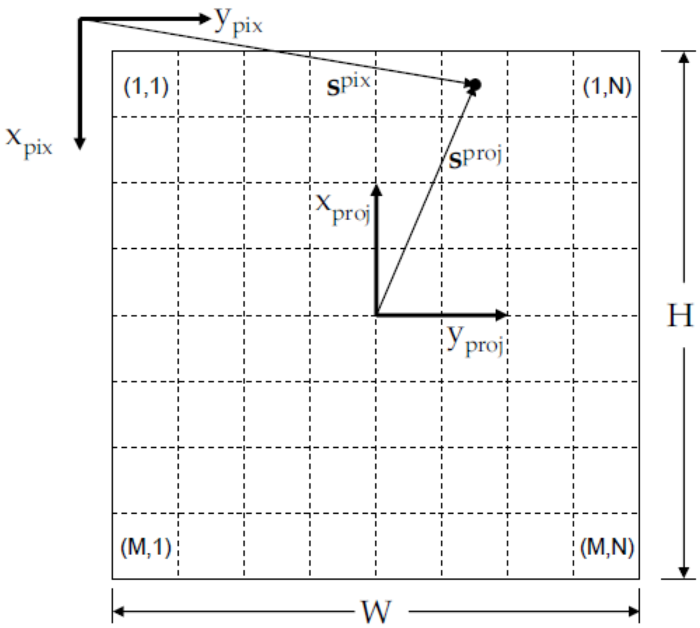

Figure 2.7. Digital Image Coordinate System. Used with permission [30].

Angular Field of View.

The angular field of view is the angle of the world scene observed by a camera's lens [10]. For a camera with a rectangular image array, the resulting angular field of view is described by two angles: a width angle α_{w} and a height angle α_{h} [1]. Figure 2.8 presents a side view of a camera model showing only the height field of view parameters. Equation 2.32 shows the height angle field of view equation with respect to the image array height h_{f} and focal length [1][10].

$$\alpha_{\mathrm{h}} = 2\tan^{-1}\left(\frac{h_{\mathrm{f}}}{2f}\right) \tag{2.32}$$

Equation 2.33 shows the determination of the height of the world scene h_{scene} observed by the camera where d_{scene} is the distance from the lens to the world scene.

$$h_{\mathrm{scene}} = 2d_{\mathrm{scene}}\tan\left(\frac{\alpha_{\mathrm{h}}}{2}\right) \tag{2.33}$$

To determine the angular field of view for width α_{w}, Equation 2.32 can be used and the image array height replaced by the image array width w_{f}.

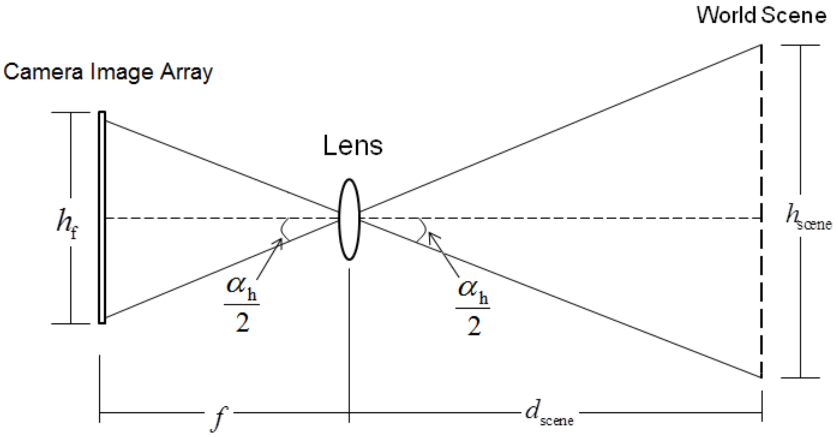

Figure 2.8. Angular field of view based on image array height (Side View).

Diffraction Limited Spot Size.

This subsection discusses the resolution of a point source within an image constrained by lens diffraction. In ideal circumstances, a lens would perfectly transfer a point source in the world scene to its detected location on an image array as shown in Figure 2.9 [10]. $\Delta\ell$ denotes the center to center pixel separation or pixel size.

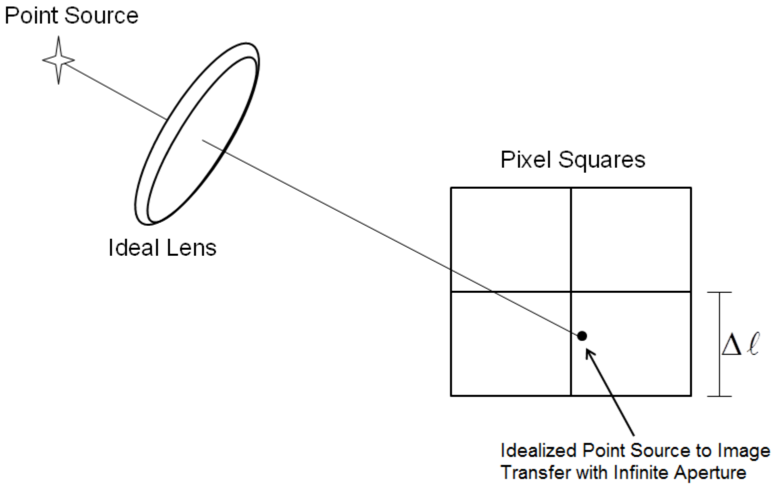

Figure 2.9. Ideal Resolution of Point Source Along Image Array.

Unfortunately, due to diffraction caused by a camera's finite aperture (neglecting atmospheric effects), the light of the point source is spread over the detector [10]. The diffraction limitation of the lens causes angular variance $\Delta\theta_{\mathrm{q}}$ in the location of the point source projection within the pixels [10]. The resulting projection of the point source on the image results in an Airy disk or diffraction limited spot, meaning that the point source projection can be located somewhere within the first ring of the Airy disk radius q_1 [10]. Figure 2.10 showcases the angular resolution of a point source in the world scene upon pixel squares within an image distorted by diffraction.

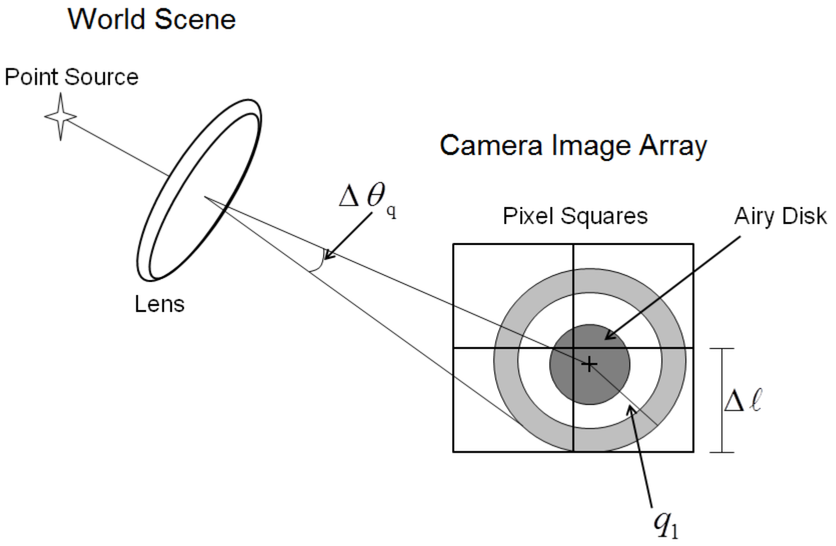

Figure 2.10. Angular Resolution of Point Source Along the Image Array.

The conversion between q_1 and $\Delta\theta_{\mathrm{q}}$ is shown in Equation 2.34 [10]. Equations 2.35 and 2.36 describe the relationships between the angle of resolution $\Delta\theta_{\mathrm{q}}$ and Airy disk radius q_1 to the focal length f, light wavelength λ_{q}, and lens diameter D respectively [10].

$$\Delta\theta_{\mathrm{q}} \approx \sin\Delta\theta_{\mathrm{q}} = \frac{q_1}{f} \tag{2.34}$$

$$\Delta\theta_{\mathrm{q}} = \frac{1.22\lambda_{\mathrm{q}}}{D} \tag{2.35}$$

$$q_1 = \frac{1.22 f \lambda_{\mathrm{q}}}{D} \tag{2.36}$$

Depending on the pixel size $\Delta\ell$, a mismatch in sampling could occur [10]. Figure 2.11 presents three cases of sampling. Case A shows an over sampled case where the Airy disk size is spread over multiple pixels. Case B presents the critically sampled case where the sampling size is equal to the Airy disk diameter cordoning the point source projection to one pixel. Case C is an under sampled case where the pixel size is much larger than the point source projection creating ambiguity to where the projection is located within the pixel itself. To obtain sub-pixel resolution of the Airy disk, it is preferred to have the Airy disk spread over many pixels [10][18] .

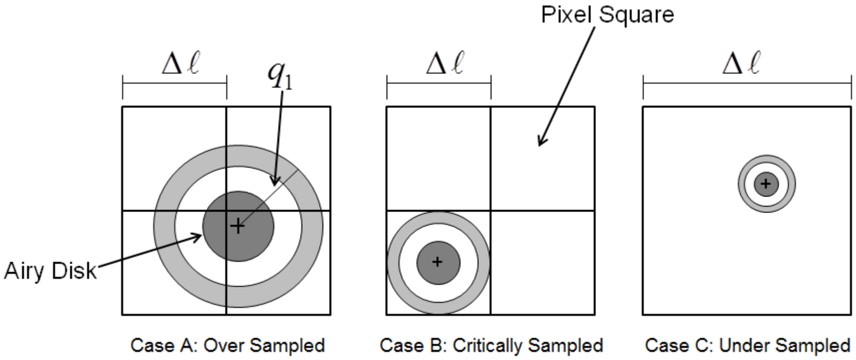

Figure 2.11. Angular resolution of diffraction limited spots with respect to sample size along the image plane.

2.6 Overview of Moon, Sun, and Earth Orbital Parameters

The following section provides a high level overview of the celestial orientation between the Sun, Moon, and Earth. Table 2.1 presents the key parameters which summarize the relationship between the three bodies.

Figures 2.12-2.14 illustrate the Earth holding an axial tilt of 23.44° with respect to its orbit plane around the Sun [31]. The Earth's sidereal orbit period around the Sun is 365.256 days traveling in a counter clockwise direction [31]. The Earth performs a

Table 2.1. Sun [32], Moon [33], and Earth [31] Parameters.

Celestial Body	Radius (km)	Distance to Earth (km)	Inclination to Equator (°)	Inclination to Ecliptic (°)	Obliquity to Orbit (°)
Sun	696,000	149,600,000	N/A	N/A	N/A
Moon	1,738.1	378,000	18.28-28.58	5.145	6.7
Earth	6,378.1	N/A	N/A	0	23.44

revolution around its own axis every 23.93 hours [31]. The ecliptic is the plane of the Earth's orbit around the Sun [31].

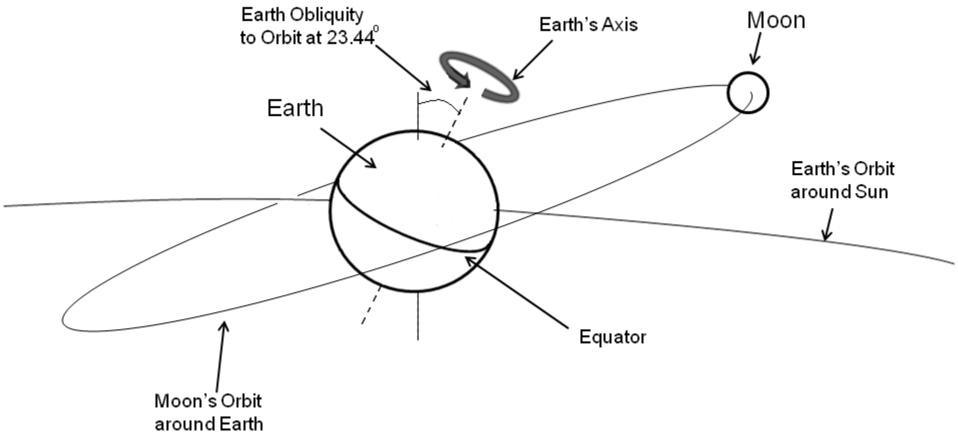

Figure 2.12. View of Orientation of Earth, Moon, and Sun Orbits [31].

The Moon's revolution period around the Earth is 27.32 days [33]. Figure 2.14 presents the Moon's orbit inclination with respect to the Earth's equator ranging from 18.28° to 28.58° [33]. During the Moon's orbit around the Earth, the Moon's axial tilt varies in librations along its latitude and longitude. Latitude librations occur at 6.7°, and longitude librations occur at 7.7° [11].

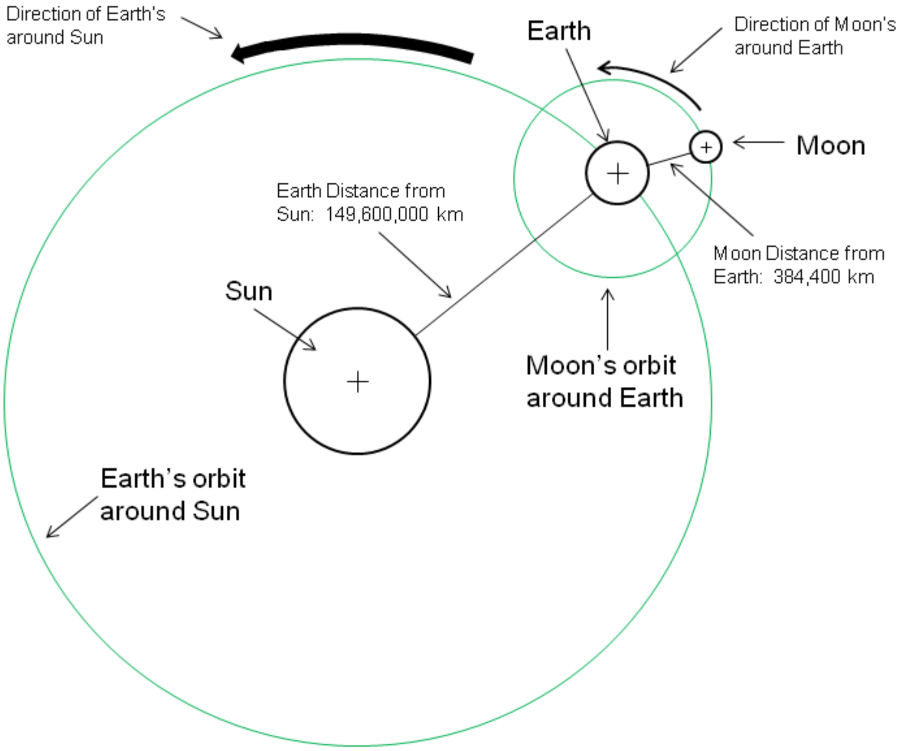

Figure 2.13. Top View of Orientation of Earth [31], Moon [33], and Sun [32] Orbits.

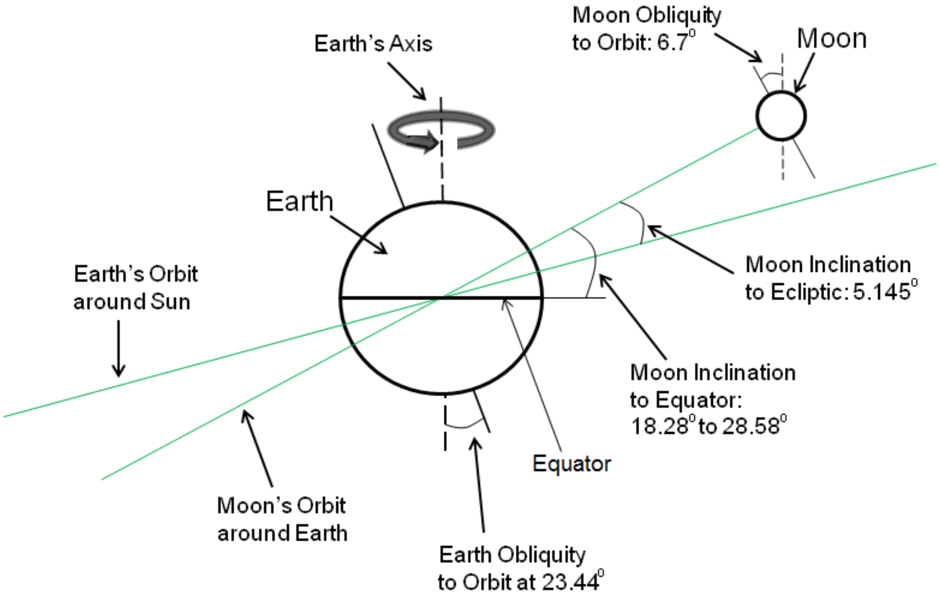

Figure 2.14. Side View of Orientation of Earth [31], Moon [33], and Sun [32] Orbits.

Figure 2.15 presents a high resolution image of the Moon's near side captured by the Lunar Reconnaissance Orbiter wide angle camera (LROC WAC) in partnership between NASA and Arizona State University. The lunar near side surface contains unique characteristics defined by smooth basins called seas or mare, craters, channels, mountains, ejecta rays, and ridges [11]. The lunar mare are the dark smooth areas along the Moon's surface in Figure 2.15 [11]. Ejecta rays are the displaced materials of impact craters that have fallen into place radially around the impact crater [11]. Ejecta rays can be seen in Figure 2.15 as the lighter straight lines oriented radially around the crater named Mount Copernicus in the middle to left portion of the image lying surrounded by the dark mare (south of Mare Ibrium) [11].

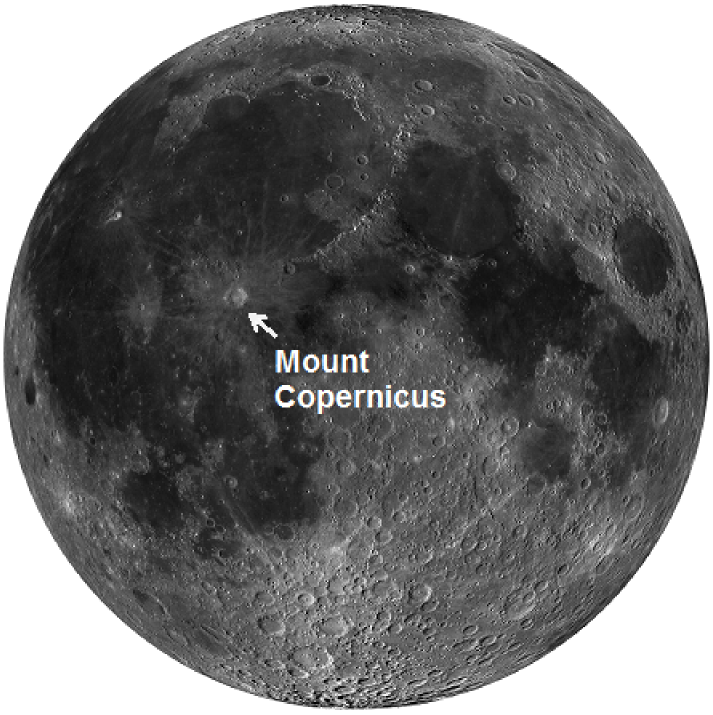

Figure 2.15. Lunar Near Side. Used with Permission [26].

2.7 Literature Review

This section discusses current non-GPS navigation sensors found in open literature which extract navigation information from natural phenomena. The first subsection presents attitude determination by computer vision techniques based upon lunar and planetary features. The second subsection discusses other various attitude determination techniques derived from knowledge of the Sun's position, Earth's magnetic field, and Earth's horizon, etc. Attitude refers to a vehicle's orientation in the b-frame represented by the Euler angles: roll ϕ, pitch θ, and yaw ψ [28]. Aiding attitude updates have been shown to improve the uncertainty of KF estimated INS position error states [2].

Attitude Determination by Lunar or Planetary Features.

Three processes in lunar or planetary image-aided navigation methods are: image collection, navigation data extraction, and attitude determination [7]. Planetary and lunar images have been identified as an attitude information source with respect to a vehicle's body frame [6][24].

In space, a vehicle's body frame attitude could be found with respect to a reference frame based on a plane consisting of the vehicle and two celestial bodies denoted by the p-frame in Figure 2.16. The p-frame origin $\mathrm{O_p}$ and the b-frame origin of the vehicle $\mathrm{O_b}$ share the same location. The pitch θ and yaw ψ angles of the b-frame with respect to the p-frame can be estimated based on the plane established by the three bodies as shown in Figure 2.16 [8]. The plane in Figure 2.16 consists of the Moon, Sun, and a vehicle with the plane's origin at $\mathrm{O_p}$. The roll angle ϕ of the vehicle body with respect to the p-frame is estimated based upon the measured rotation angle ϑ of the vehicle body in relation to the Moon. Mortari and Park propose using a stored catalog Moon image to compare with the observed Moon image. This would allow a translation and rotation calculation between the images to be performed to determine ϑ [24]. Enright's method to determine ϑ differed due to his use of over-exposed star tracker Moon images instead [8].

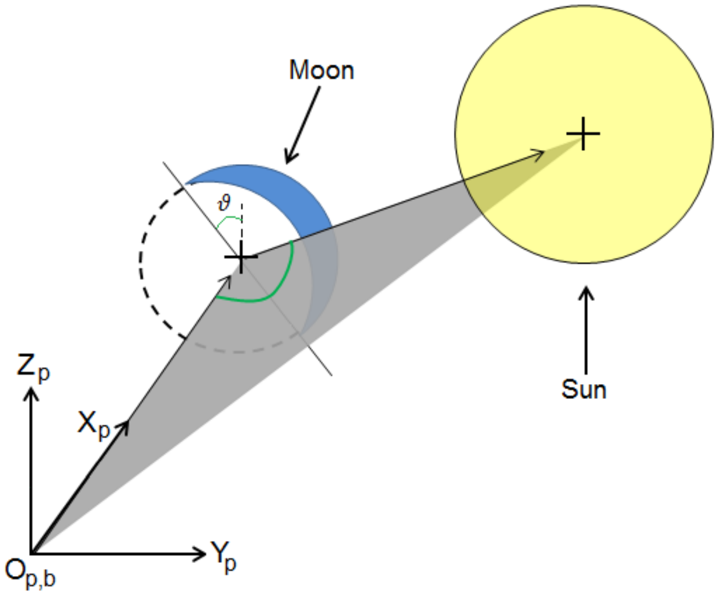

Figure 2.16. Attitude Determination by Celestial Bodies [8].

Key Points Feature Detection.

Key points feature detection and extraction is characterized by the detection and tracking of features of interest. Absolute attitude sensors such as second generation star trackers use the method to detect and track celestial bodies, i.e. stars [18]. The method can also be used on planetary features [15]. The process works by having key points information stored within a processing software database or catalog. The database holds information about each key point's unique characteristics and can be compared with an observed image of the same terrain or star pattern to gain rotation and translation information in a vehicle's body frame [7].

For the star tracker, a star's magnitude and brightness serve as unique qualities and are stored in a star catalog [16]. The star catalog holds information about each stars arrangement in relation to the nearest stars. A set of three stars in close proximity is called a Triangle Feature (TF) [16]. This can be seen in Figure 2.17. TFs are the basic pattern from which meaningful attitude information can be extracted within a star tracker [16]. The unique characteristics of a TF are listed in Equation 2.37 derived from Figure 2.17 where Star C is the center star, Star A is the first nearest star to Star C, and Star B is the second nearest neighbor to Star C. Within [16], the star catalog stores a vast number of TF combinations. Liebe in [16] performs a quantization on the TF combinations to conserve memory. Under quantization, the stored TF reference listed in Figure 2.17 would read [55, 81, 32]. A star averages 180 star catalog references in relation to the TFs its contained in [16].

$$\begin{bmatrix} \text{Distance to Star A}, & \text{Distance to Star B}, & \text{Angle between Stars A and B} \end{bmatrix} \tag{2.37}$$

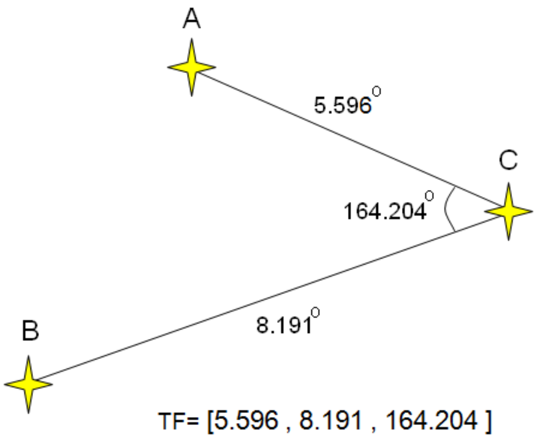

Figure 2.17. Star Tracker Triangle Feature [16].

In many cases, it is not enough to locate key points based at given pixel locations. Subpixel resolution quality is needed to determine exactly where the key point is located within an image. This is called hyperacuity or subpixel precision [18]. To achieve this goal, the process of centroiding can be used. At the pixel level, a key point can appear to be uniform in intensity. Centroiding consists of slightly blurring an image to obtain a Gaussian form of pixel intensities around a key point [18]. The tighter mean extracted from the key point intensity distribution provides a more accurate subpixel level data point supporting an improved attitude determination [18].

Van Bezooijen's key point extraction method doesn't solely rely on TFs for correspondence between the observed key points and its key point catalog [7]. Van Bezooijen's algorithm works from the premise that an increase of stars in view creates a more unique star pattern to improve attitude determination. Based upon Van Bezooijen's algorithm, researchers in [7] are working on the statistics and viability of an N-star pattern recognition algorithm for attitude determination.

Key points extraction and detection methods can be used in extracting planetary features for navigational purposes [15][17]. Liebe's criteria in [15] for a robust feature extraction algorithm upon planet terrain is for the algorithm to operate proficiently withstanding changes in vantage points, occlusion, lighting, and rotation. He reaches the conclusion that this aim can be achieved through the use of token-based closed contour tracking very similar to key points extraction and detection used in star trackers. According to Liebe, the features must hold a distinguishable quality that allows them to be recognized from a wide range of vantage points and lighting conditions [15]. From images of Jupiter, he was able to extract features to be used for a closed contour feature constellation while rotation and occlusion separately occurred [17].

Hough Transform.

Another method of feature detection and extraction that has been explored for attitude determination purposes is the Hough Transform. The Hough Transform is a robust algorithm used to detect specified shapes within images, particularly, lines and circles [6][14]. In [6], a circular crater on Saturn's moon, Mimas, was successfully detected using the Hough Transform. Both [6] and [14] voice that although the transform's performance is high at detecting shapes within an image, an increase in the parameters and complexity of the detectable image shapes would greatly increase the computational memory needed. In [14], the suggestion is made that extensions to the Hough Transform exist which reduce the inefficient algorithm needs. However, the stripping away of the algorithm leads to instability in the algorithm when processing shapes slightly different than the specified template [14].

Gray Level Cooccurance (GLC) Matrices.

In [29], a feature detection method utilizing GLC matrices was implemented to extract planetary features, e.g. mountains, volcanoes, and valleys. The research in [29] was conducted in the context of providing extracted features for planetary terrain tracking and navigation purposes. A GLC matrix scans a defined image region and estimates the second-order probability for a specified gray level change between adjoined pixels [29]. Each GLC is tuned to extract a type of image feature. Equation 2.38 represents a type of GLC tested in [29] where the gray levels are represented by L_{g}, δ_{g} is the separation between any two pixels within the local region T_{g}, and i_{g} and j_{g} are the gray levels. The Inertia GLC matrix below suited identifying random gray-leveled areas, and the Entropy GLC matrix was found to be the most robust GLC matrix [29]. The Cluster Shade GLC matrix was found to favor feature extraction within high contrasting gray level regions which are characterized by craters. Although, not holding high performance as the specialized GLCs in their respective environments, it was consistent in its performance over various local regions and features.

Inertia:

$$I(\delta_{\mathrm{g}}, T_{\mathrm{g}}) = \sum_{i_{\mathrm{g}}=0}^{L\mathrm{g}-1} \sum_{j_{\mathrm{g}}=0}^{L\mathrm{g}-1} (i_{\mathrm{g}} - j_{\mathrm{g}})^2 s(i_{\mathrm{g}}, j_{\mathrm{g}}, \delta_{\mathrm{g}}, T_{\mathrm{g}}) \tag{2.38}$$

Following the GLC matrix tests conducted on images of moons, Triton and Miranda, Udomkesmalee and Antonio concluded that although GLC matrices provided distinct feature detection results, the quality and the method fell short. This was due in part to the difficulty of sorting out shadow areas causing mis-characterizations of planetary features and the complexity surrounding the recognition of numerous feature types [29].

Template Matching.

Template Matching is another method used in feature detection of planetary terrain and attitude determination as read in [4] and [6]. In [24], a method of template matching is performed on Moon images. The algorithm called the *Moon-Sun Attitude Sensor* works by matching an observed image of the Moon to a stored reference image. The resulting captured image is then translated and rotated until it matches the reference Moon image. Equation 2.39 characterizes the match of the two Moon images through the quantity r which represents the correlation quantity [24]. Once r equals 0, then a perfect match has been reached. Once the perfect match is achieved, the phase angle ϑ, which the template was rotated to match the observed image, can provide information to aid in attitude determination. This was briefly discussed in the beginning of this section and shown as the end result of Mortari and Park's attitude algorithm in Figure 2.18. In Equation 2.39, the image correlation equation is presented where I_{m} and J_{m} represent the respective Moon images to be matched. $\bar{I}_{\mathrm{m}}$ and $\bar{J}_{\mathrm{m}}$ are stated to be the mean value of each image. c and d are the pixel index numbers.

$$r = \frac{\sum_{c,d}(I_{\mathrm{m},(c,d)} - \bar{I}_{\mathrm{m}})(J_{\mathrm{m},(c,d)} - \bar{J}_{\mathrm{m}})}{\sqrt{\sum_{c,d}\left(I_{\mathrm{m},(c,d)} - \bar{I}_{\mathrm{m}}\right)^2 \sum_{c,d}\left(J_{\mathrm{m},(c,d)} - \bar{J}_{\mathrm{m}}\right)^2}} \tag{2.39}$$

A similar equation to Equation 2.39 was found in [6] showing the commonality of the correlation equation within the template matching method of feature detection. To increase the efficiency of correlation, [6] suggests that correlation can be carried out in the Frequency Domain with Fast Fourier Transform.

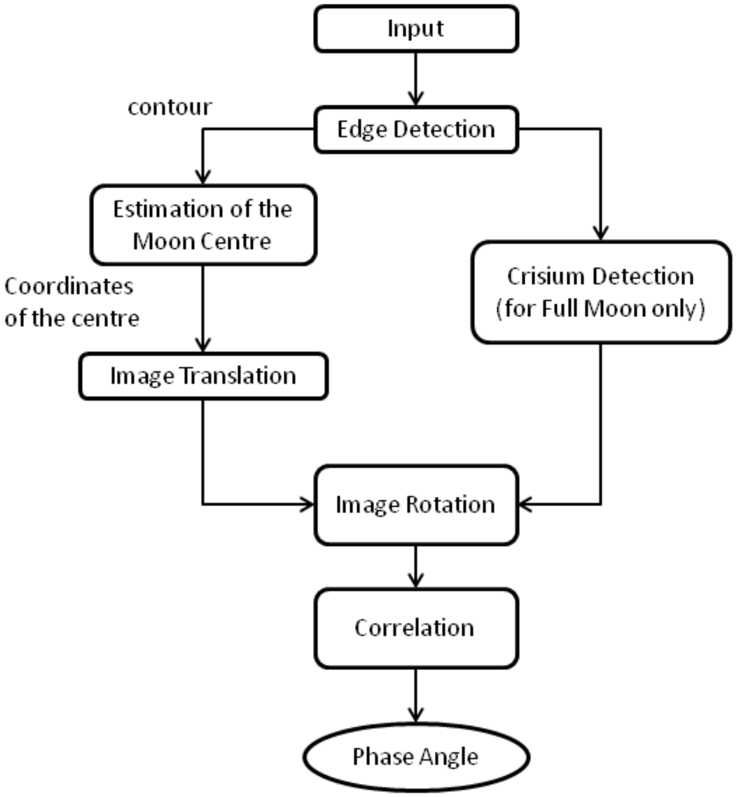

Figure 2.18. Mortari and Park's Image Processing Outline. Used with permission [24].

Figure 2.18 is a feature detection algorithm example involving template matching. From this figure, the various stages of image processing involved in template matching feature detection can be viewed. Mortari and Park first perform median filtering to remove noise [24]. From here, a binary image can be created from the observed image and edge detection conducted. As unique to [24], if the Moon is full and symmetric, the sea of Crisium will be selected as to perform edge detection upon. At this point, the captured edge is translated and rotated to gain the match and phase angle ϑ as mentioned earlier in this section. Lastly, Mortari admits that the *Moon-Sun Attitude Sensor* performance would not match the performance of modern star trackers; however, the sensor could be viable in budget constrained environments [23]. Also, a *Moon-Sun Attitude Sensor* aided INS system could have the potential to match a star tracker's performance.

Natural Passive Signals Sensor Methods.

The following subsection covers different sensor types which derive position and attitude information from natural phenomena. Each listed sensor does not provide a complete navigation solution on its own, but provides separate angle or range measurements when coupled together can be used in trajectory estimation or to gain a position fix. Sensor combination addresses this issue by combining the measurements of disparate sensors to form a complete navigation solution [13].

Sun Sensor.

The Sun holds a predictable ephemeris track across the Earth each day. From this constant motion, angle measurements can be derived from different Earth locations with respect to the Sun and the horizon to gain an *elevation* angle measurement which holds latitude position information [9]. Modern sun sensors also follow a similar *elevation* angle angle concept, however, using the Sun's angles for attitude determination instead [18][19]. Liebe has continued research into enhancing the ancient sun sensor methodology to develop a micro sun sensor providing solar angle information based around MEMS technology and a centroiding technique [19]. Liebe's micro sun sensor consists of a miniature enclosed box with an aperture at the top to create a well where the Sun's rays can enter. Based upon the direction that the Sun's rays strike the wafers aligned along the well floor, an angle of the Sun's rays can be obtained which leads to a unique attitude solution. Liebe in [18] lists sun sensors with an accuracy of 1 arcminute for attitude determination.

Magnetometer.

Magnetometers are sensors which employ the Earth's magnetic field to gain magnetic measurements corresponding to a unique attitude determination. The readings consist of the size and orientation of the magnetic field lines [18]. The reported accuracy for magnetometers is around 1 arcminute [18].

Horizon Sensor.

Utilizing measurements based upon the limb of the Earth, navigation information can be derived to gain a unique attitude determination [18]. The limb measurements are typically captured through an infrared camera [18]. Liebe lists the accuracy of horizon sensors at 5 arcminutes which is the least accurate as compared to the other sensors listed in [18].

Star Tracker.

Referenced in the previous subsection, star trackers are optical sensors which capture constellation information to gain an attitude determination. In this research effort, second generation star trackers are referred to. Second generation star trackers consist of a charge coupled device (CCD) camera and an associated software package which holds a star database and star catalog [16][18]. The captured constellation images are compared to a stored catalog image of the observed constellation, and a unique set of angles can be computed which provide a navigation solution [18]. Star trackers hold an accuracy of 1 arcsecond as shown in [18]. This is the highest accuracy in comparison to the other sensors listed.

2.8 Summary

Chapter 2 provided the necessary theoretical background to support the methodology approach discussed in Chapter 3. Dynamics models, computer vision techniques, and camera projection theory were discussed as well as KF and EKF estimation methods. An overview of the lunar orbital parameters and the lunar surface was covered. Various open literature methods of non-GPS navigation sensors were presented as well.

III. Methodology

3.1 Introduction

The methodology chapter discusses the models and methods that were put into practice to perform drift correction on INS errors aided by lunar feature angle measurements. Section 3.2 discusses the overall system model. Section 3.3 describes the truth model used to simulate the flight trajectory. Section 3.4 presents the error state motion model that was used to simulate INS errors. Section 3.5 shows the validation of the error state motion model. Section 3.6 covers the measurement model used to correct the INS errors. Section 3.7 presents the lunar feature model. Section 3.8 discusses the EKF implementation process. Section 3.9 provides the summary of the section.

3.2 System Overview

To gain an understanding of the system as a whole, the following section discusses the error state model, the error state estimation model, and presents the system block diagram.

The INS error model in Equation 3.1 shows the relationship between the INS error states $\delta\mathbf{x}_k$, errant truth $\mathbf{x}_{\text{INS},k}$, and true states $\mathbf{x}_k$ [5]. The true states $\mathbf{x}_k$ hold direct trajectory information and the trajectory model is presented in Section 3.3. The INS error states $\delta\mathbf{x}_k$ are based on the Pinson 15 error state dynamics model described in Section 3.4. Equation 3.2 shows how the subtraction of the INS errors from the true states is used to create the simulated INS trajectory $\mathbf{x}_{\text{INS},k}$. With the error states modeled on INS error noise strengths (see Table 3.1), the corrupted truth can act as a realistic INS modeled trajectory.

$$\mathbf{x}_k = \mathbf{x}_{\text{INS},k} + \delta\mathbf{x}_k \tag{3.1}$$

$$\mathbf{x}_{\text{INS},k} = \mathbf{x}_k - \delta\mathbf{x}_k \tag{3.2}$$

With the INS trajectory and INS errors simulated, estimation of the true states $\mathbf{x}_k$ can be performed. This research effort utilizes an indirect truth estimation approach called error state estimation whereby the INS error states $\delta\mathbf{x}_k$ are estimated as shown in discrete form $\delta\hat{\mathbf{x}}_k$ in the error estimation propagation equation below [5].

$$\delta\hat{\mathbf{x}}_k^- = \mathbf{\Phi}\delta\hat{\mathbf{x}}_{k-1}^+ + \mathbf{w}_k \tag{3.3}$$

Once the INS error states are estimated, Equation 3.4 shows the quantities are added to the errant INS trajectory $\mathbf{x}_{\text{INS},k}$ to bring about an estimation $\hat{\mathbf{x}}_k$ of the true states $\mathbf{x}_k$.

$$\hat{\mathbf{x}}_k = \mathbf{x}_{\text{INS},k} + \delta\hat{\mathbf{x}}_k \tag{3.4}$$

Figure 3.1 presents the system block diagram containing the INS trajectory, lunar vision measurements, and the EKF working together to estimate an aircraft's true trajectory based upon the error state estimation model. The system follows an indirect feed forward format [20].

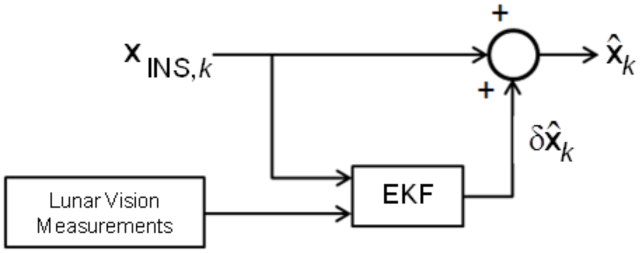

Figure 3.1. Lunar Vision Aided Navigation with INS Block Diagram.

3.3 Truth Model

The truth model of aircraft motion is simulated by a circular trajectory with radius 20km along the north and east plane in the n-frame as shown in Equations 3.5-3.8 with distance in meters. μ is the circle central angle. The truth along the north and east position states was kept unchanged to act a baseline throughout the various scenarios that were conducted. $\mathbf{p}_{\mathrm{N},k}$ and $\mathbf{v}_{\mathrm{N},k}$ are the position and velocity of the aircraft along the north axis respectively.

$$\mathbf{p}_{\mathrm{N},k} = \mathbf{p}_{\mathrm{N},0} + 20000\mathrm{sin}(\mu) \tag{3.5}$$

$$\mathbf{v}_{\mathrm{N},k} = \frac{\mathbf{p}_{\mathrm{N},k} - \mathbf{p}_{\mathrm{N},k-1}}{(\Delta t)_k} \tag{3.6}$$

$$\mathbf{p}_{\mathrm{E},k} = \mathbf{p}_{\mathrm{E},0} + 20000\mathrm{cos}(\mu) \tag{3.7}$$

$$\mathbf{v}_{\mathrm{E},k} = \frac{\mathbf{p}_{\mathrm{E},k} - \mathbf{p}_{\mathrm{E},k-1}}{(\Delta t)_k} \tag{3.8}$$

The down axis motion is generated by a First Order Gauss Markov (FOGM) acceleration model which represents aircraft motion in a realistic fashion [5]. Figure 3.2 is the FOGM acceleration model block diagram representing the down axis of motion over continuous time. τ is the system's correlation time constant [20].

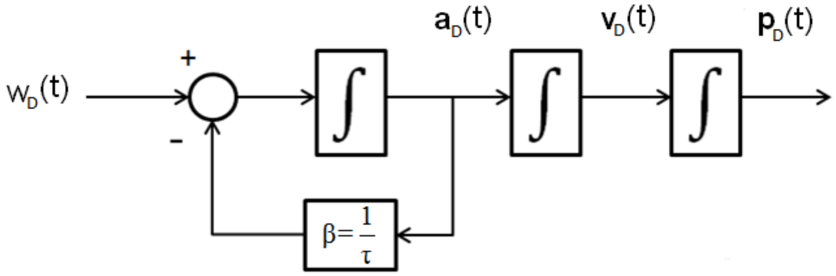

Figure 3.2. n-frame Down axis FOGM acceleration model Block Diagram [20].

The set of first order linear differential equations describing the down axis motion are shown in Equations 3.9 through 3.11 where each differential equation is defined by the motion states of acceleration $\mathbf{a}$, velocity $\mathbf{v}$, or position $\mathbf{p}$ [20]. $\mathbf{w}(t)$ is white Gaussian noise on the acceleration state.

$$\dot{\mathbf{a}}_{\mathrm{D}}(t) = \left(-\frac{1}{\tau}\right)\mathbf{a}_{\mathrm{D}}(t) + \mathbf{w}_{\mathrm{D}}(t) \tag{3.9}$$

$$\dot{\mathbf{v}}_{\mathrm{D}}(t) = \mathbf{a}_{\mathrm{D}}(t) \tag{3.10}$$

$$\dot{\mathbf{p}}_{\mathrm{D}}(t) = \mathbf{v}_{\mathrm{D}}(t) \tag{3.11}$$

The first order differential equation form of the down axis truth model is shown in Equation 3.12 with incorporated random noise [20]. However, due to research scope, the control inputs $\mathbf{u}(t)$ are not being evaluated in the state propagation. Therefore, the control inputs are set to zero in Equation 3.13.

$$\dot{\mathbf{x}}(t) = \mathbf{F}\mathbf{x}(t) + \mathbf{B}\mathbf{u}(t) + \mathbf{G}\mathbf{w}(t) \tag{3.12}$$

$$\dot{\mathbf{x}}(t) = \mathbf{F}\mathbf{x}(t) + \mathbf{G}\mathbf{w}(t) \tag{3.13}$$

Equation 3.14 represents the down axis state space truth model.

$$\begin{bmatrix} \dot{\mathbf{p}}_{\mathrm{D}} \\ \dot{\mathbf{v}}_{\mathrm{D}} \\ \dot{\mathbf{a}}_{\mathrm{D}} \end{bmatrix} = \begin{bmatrix} 0 & 1 & 0 \\ 0 & 0 & 1 \\ 0 & 0 & -\frac{1}{\tau} \end{bmatrix} \begin{bmatrix} \mathbf{p}_{\mathrm{D}} \\ \mathbf{v}_{\mathrm{D}} \\ \mathbf{a}_{\mathrm{D}} \end{bmatrix} + \begin{bmatrix} 0 \\ 0 \\ \mathbf{w}_{\mathrm{D}} \end{bmatrix} \tag{3.14}$$

Equation 3.15 is the down axis input noise covariance matrix $\mathbf{Q}(t)$ representing the input noise for the down axis state space truth model. The input noise is white Gaussian noise with zero mean [20]. The relationship between the input noise and the process noise can be seen in Equation 3.16 where σ_{D} is the process noise standard deviation [20].

$$\mathbf{Q}(t) = \mathrm{E}\left[\mathbf{w}_{\mathrm{D}}(t)\mathbf{w}_{\mathrm{D}}^{\mathrm{T}}(t)\right] = \mathrm{E}\left[\mathbf{w}_{\mathrm{D}}^{2}\right] \tag{3.15}$$

$$\mathbf{Q}(t) = \frac{2\sigma_{\mathrm{D}}}{\tau} \tag{3.16}$$

3.4 Error State Motion Model

To simulate realistic INS errant behavior, a dynamics model following the continuous time first order linear differential equation form with incorporated random noise input was implemented as shown in Equation 3.17 [28]. The control inputs $\mathbf{u}(t)$ are not being evaluated in the error state propagation and are set to zero in Equation 3.18. The error states are seen in Equation 3.19 which is the error state vector $\delta\mathbf{x}$. The five error state categories are position error $\delta\mathbf{p}$, velocity error $\delta\mathbf{v}$, tilt $\boldsymbol{\psi}$, accelerometer bias $\delta\mathbf{a}$, and gyroscope bias $\delta\mathbf{b}$. The error state vector holds fifteen error states as each of the five error state categories are propagated in three directions (NED) [28][30].

$$\delta\dot{\mathbf{x}}(t) = \mathbf{F}\delta\mathbf{x}(t) + \mathbf{B}\mathbf{u}(t) + \mathbf{G}\mathbf{w}(t) \tag{3.17}$$

$$\delta\dot{\mathbf{x}}(t) = \mathbf{F}\delta\mathbf{x}(t) + \mathbf{G}\mathbf{w}(t) \tag{3.18}$$

$$\delta\mathbf{x}(t) = \begin{bmatrix} \delta\mathbf{p}(t) \\ \delta\mathbf{v}(t) \\ \boldsymbol{\psi}(t) \\ \delta\mathbf{a}(t) \\ \delta\mathbf{b}(t) \end{bmatrix} \tag{3.19}$$

The state space form of the INS error state motion model is shown in Equation 3.20 along with the random noise inputs [28][30]. The position states do not contain any input noise entering into them due to fact that the position error states are integrated directly from the velocity error states which do contain input noise. The $\delta\mathbf{v}$ and $\boldsymbol{\psi}$ error states both are random walk processes [13][30]. The $\delta\mathbf{a}$ and $\delta\mathbf{b}$ error states follow a FOGM process [13][30]. It should be noted that the system noise mapping matrix $\mathbf{G}$ is located along the second line of Equation 3.20.

$$
\begin{aligned}
\begin{bmatrix} \delta\dot{\mathbf{p}}(t) \\ \delta\dot{\mathbf{v}}(t) \\ \dot{\boldsymbol{\psi}}(t) \\ \delta\dot{\mathbf{a}}(t) \\ \delta\dot{\mathbf{b}}(t) \end{bmatrix} &= \begin{bmatrix} \mathbf{0} & \mathbf{I} & \mathbf{0} & \mathbf{0} & \mathbf{0} \\ \mathbf{C}_{\mathrm{e}}^{\mathrm{n}}\mathbf{D}\mathbf{C}_{\mathrm{n}}^{\mathrm{e}} & -2\mathbf{C}_{\mathrm{e}}^{\mathrm{n}}\boldsymbol{\Omega}_{\mathrm{ie}}^{\mathrm{e}}\mathbf{C}_{\mathrm{n}}^{\mathrm{e}} & (\mathbf{f}^{\mathrm{n}}\times) & \mathbf{C}_{\mathrm{b}}^{\mathrm{n}} & \mathbf{0} \\ \mathbf{0} & \mathbf{0} & -(\mathbf{C}_{\mathrm{e}}^{\mathrm{n}}\omega_{ie}^{\mathrm{e}})\times & \mathbf{0} & -\mathbf{C}_{\mathrm{b}}^{\mathrm{n}} \\ \mathbf{0} & \mathbf{0} & \mathbf{0} & -\frac{1}{\tau_{\mathrm{a}}}\mathbf{I} & \mathbf{0} \\ \mathbf{0} & \mathbf{0} & \mathbf{0} & \mathbf{0} & -\frac{1}{\tau_{\mathrm{b}}}\mathbf{I} \end{bmatrix} \begin{bmatrix} \delta\mathbf{p}(t) \\ \delta\mathbf{v}(t) \\ \boldsymbol{\psi}(t) \\ \delta\mathbf{a}(t) \\ \delta\mathbf{b}(t) \end{bmatrix} \\
&\quad + \begin{bmatrix} \mathbf{0} & \mathbf{0} & \mathbf{0} & \mathbf{0} \\ \mathbf{C}_{\mathrm{b}}^{\mathrm{n}} & \mathbf{0} & \mathbf{0} & \mathbf{0} \\ \mathbf{0} & -\mathbf{C}_{\mathrm{b}}^{\mathrm{n}} & \mathbf{0} & \mathbf{0} \\ \mathbf{0} & \mathbf{0} & \mathbf{I} & \mathbf{0} \\ \mathbf{0} & \mathbf{0} & \mathbf{0} & \mathbf{I} \end{bmatrix} \begin{bmatrix} \mathbf{w}_{\delta\mathbf{v}}(t) \\ \mathbf{w}_{\boldsymbol{\psi}}(t) \\ \mathbf{w}_{\delta\mathbf{a}}(t) \\ \mathbf{w}_{\delta\mathbf{b}}(t) \end{bmatrix}
\end{aligned} \tag{3.20}
$$

The input noise covariance matrix $\mathbf{Q}(t)$ for the error state motion model in Equation 3.21 has input noise entering into the last four error state categories $\delta\mathbf{v}$, $\boldsymbol{\psi}$, $\delta\mathbf{a}$, and $\delta\mathbf{b}$ [30]. The pre-defined error noise strength values for these states used in INS error state simulation are presented in Table 3.1. The correlation time constant τ for the accelerometer bias $\delta\mathbf{a}$ and the gyroscope bias $\delta\mathbf{b}$ for an INS are 3600 seconds for error state simulation of each INS grade [13].

$$\mathbf{Q}(t) = \begin{bmatrix} \mathbf{0} & \mathbf{0} & \mathbf{0} & \mathbf{0} & \mathbf{0} \\ \mathbf{0} & \frac{2\sigma_{\delta\mathbf{v}(t)}}{\tau} & \mathbf{0} & \mathbf{0} & \mathbf{0} \\ \mathbf{0} & \mathbf{0} & \frac{2\sigma_{\boldsymbol{\psi}(\mathbf{t})}}{\tau} & \mathbf{0} & \mathbf{0} \\ \mathbf{0} & \mathbf{0} & \mathbf{0} & \frac{2\sigma_{\delta\mathbf{a}(t)}}{\tau} & \mathbf{0} \\ \mathbf{0} & \mathbf{0} & \mathbf{0} & \mathbf{0} & \frac{2\sigma_{\delta\mathbf{b}(t)}}{\tau} \end{bmatrix} \tag{3.21}$$

Table 3.1. Noise Strength values of INS Grades for use in error simulation [13]

INS Grade	$\sigma_{\delta\mathbf{b}(t)}\left(\frac{\text{rad}}{\text{s}}\right)$	$\sigma_{\delta\mathbf{a}(t)}\left(\frac{\text{m}}{\text{s}^2}\right)$	$\sigma_{\delta\mathbf{v}(t)}\left(\frac{\text{rad}}{\text{s}^{\frac{1}{2}}}\right)$	$\sigma_{\boldsymbol{\psi}(t)}\left(\frac{\text{m}}{\text{s}^{\frac{3}{2}}}\right)$
Commercial (Cloudcap Crista)	8.7×10^{-3}	1.96×10^{-1}	6.5×10^{-4}	4.3×10^{-3}
Tactical (HG1700)	4.8×10^{-6}	9.8×10^{-3}	8.7×10^{-5}	9.5×10^{-3}
Navigation (HG 9900 - H764G)	7.2×10^{-9}	2.45×10^{-4}	5.8×10^{-7}	2.3×10^{-4}

Equation 3.23 is the b-frame to n-frame DCM used in the error state motion model [30]. The inputs to the DCM are vehicle body Euler angle rotations roll ϕ, pitch θ, and yaw ψ which are measured in radians as shown in Equation 3.22. The DCM can be used to rotate a vector from the b-frame to the n-frame which is in meters [28][30]. A transpose of the DCM $\mathbf{C}_{\text{b}}^{\text{n}}$ will result in the reverse DCM $\mathbf{C}_{\text{n}}^{\text{b}}$.

$$\boldsymbol{\omega}_{\text{b}} = \begin{bmatrix} \phi \\ \theta \\ \psi \end{bmatrix} \tag{3.22}$$

$$\mathbf{C}_{\text{b}}^{\text{n}} = \begin{bmatrix} \cos(\psi)\cos(\theta) & -\sin(\psi)\cos(\phi) + \cos(\psi)\sin(\theta)\sin(\phi) & \sin(\psi)\sin(\phi) + \cos(\psi)\sin(\theta)\cos(\phi) \\ \sin(\psi)\cos(\theta) & \cos(\psi)\cos(\phi) + \sin(\psi)\sin(\theta)\sin(\phi) & -\cos(\psi)\sin(\phi) + \sin(\psi)\sin(\theta)\cos(\phi) \\ -\sin(\theta) & \cos(\theta)\sin(\phi) & \cos(\theta)\cos(\phi) \end{bmatrix} \tag{3.23}$$

Equation 3.24 is the DCM that rotates position information from the e-frame to the n-frame [28][30]. The DCM takes in latitude L and longitude λ coordinates in radians.

$$\mathbf{C}_{\mathrm{e}}^{\mathrm{n}} = \begin{bmatrix} -\sin(L)\cos(\lambda) & -\sin(L)\sin(\lambda) & \cos(L) \\ -\sin(\lambda) & \cos(L) & 0 \\ -\cos(L)\cos(\lambda) & -\cos(L)\sin(\lambda) & -\sin(L) \end{bmatrix} \tag{3.24}$$

The Earth's rotation must be taken into account when computing errors for an aircraft traversing over the Earth [30]. Equation 3.25 represents the Earth's rotation with respect to the i-frame [30]. In the INS error state motion model, this is rotated into the n-frame and affects the tilt error state. Equation 3.26 is the skew symmetric matrix of Equation 3.25. Equation 3.26 accounts for the Earth's rotation in the velocity error states [30]. The Earth rotation rate Ω used in this research effort is $7.292115 \times 10^{-5} \frac{\mathrm{rad}}{\mathrm{s}}$ (WGS-84) [28].

$$\boldsymbol{\omega}_{\mathrm{ie}}^{\mathrm{e}} = \begin{bmatrix} 0 \\ 0 \\ \Omega \end{bmatrix} \tag{3.25}$$

$$\boldsymbol{\Omega}_{\mathrm{ie}}^{\mathrm{e}} = \begin{bmatrix} 0 & -\Omega & 0 \\ \Omega & 0 & 0 \\ 0 & 0 & 0 \end{bmatrix} \tag{3.26}$$

Gravity over the surface of the Earth varies slightly based upon a region's elevation [30]. To account for this phenomenon within the position error component of the velocity error state, a gradient value **D** is used as a unique regional approximation of gravity [30]. **D** in Equation 3.27 represents a gravitational constant unique to a specific region based around the aircraft's current position with respect to the e-frame

$\check{\mathbf{p}}^{\mathrm{e}}$ and the skew symmetric of the earth's rotation vector from Equation 3.26 [30]. The gravitational constant g is 9.8 $\frac{\mathrm{m}}{\mathrm{s}^2}$ [31].

$$\mathbf{D} = \nabla g\big|_{\mathbf{p}^{\mathrm{n}}} = \frac{g}{\left\|\mathbf{p}^{\mathrm{e}}\right\|^3}\left[3\check{\mathbf{p}}^{\mathrm{e}}(\check{\mathbf{p}}^{\mathrm{e}})^{\mathrm{T}} - \mathbf{I}\right] - (\boldsymbol{\Omega}^{\mathrm{e}}_{\mathrm{ie}})^2 \tag{3.27}$$

Accelerometers within INS units output specific force measurements which in this research effort are within vector $\mathbf{f}^{\mathrm{b}}$ with respect to the b-frame as shown in Equation 3.28 [30]. For the velocity error states, the specific force measurements are taken into account through rotation into the n-frame as seen in Equation 3.29 [30]. For this research effort, the simulated aircraft trajectory is a wings level flight.

$$\mathbf{f}^{\mathrm{b}} = \begin{bmatrix} f^{\mathrm{b}}_{\phi} \\ f^{\mathrm{b}}_{\theta} \\ f^{\mathrm{b}}_{\psi} \end{bmatrix} = \mathbf{C}^{\mathrm{b}}_{\mathrm{n}}\left(\frac{\Delta v}{\Delta t}\right) \tag{3.28}$$

$$\mathbf{f}^{\mathrm{n}} = \mathbf{C}^{\mathrm{n}}_{\mathrm{b}}\mathbf{f}^{\mathrm{b}} \tag{3.29}$$

3.5 Error State Motion Model Validation

To verify the INS error state motion model, it is incumbent to achieve a match between the simulated error ensemble statistics of the INS error model and the INS error theoretical statistics [20]. The theoretical or analytical statistics are the INS grade dependent theoretical results that would be expected of INS errors propagated over time. The theoretical statistics create a template that shows expected INS errant behavior over time. The form of the theoretical statistics can be inferred due to the Gaussian nature of the model's distribution where the mean is zero and the standard deviation follows the σ values listed in Table 3.1 [20].

The INS error state motion model's simulated error statistics are collected from propagating multiple runs of the error state motion model over time in Equation 3.20 and then determined by the ensemble mean and standard deviation [5]. If the ensemble statistics match the form of the theoretical statistics, the model can be considered sound as a means to simulate INS errors during a vehicle trajectory [20]. To prove the validity of the error state motion model in Equation 3.20, a Monte Carlo simulation of 10,000 runs was conducted for all three grades of INS based on the simulation parameters listed in Table 3.2. Figures 3.3-3.5 show the ensemble and theoretical statistics matching for the position state in three directions for a propagation of ten minutes. It is clear, the errors decrease exponentially with the change in the quality of INS grades from Commercial to Navigation Grade.

Table 3.2. Simulation Parameter for Error State Motion Model Validation [13].

Monte Carlo Simulation Parameters	
Propagation Time Step $(\Delta t)_k$	1s
Aircraft Initial Position	(0,0,0) m
Aircraft Initial Velocity	(200,0,0) $\frac{m}{s}$
Aircraft Initial Acceleration	(0,0,0) $\frac{m}{s^2}$

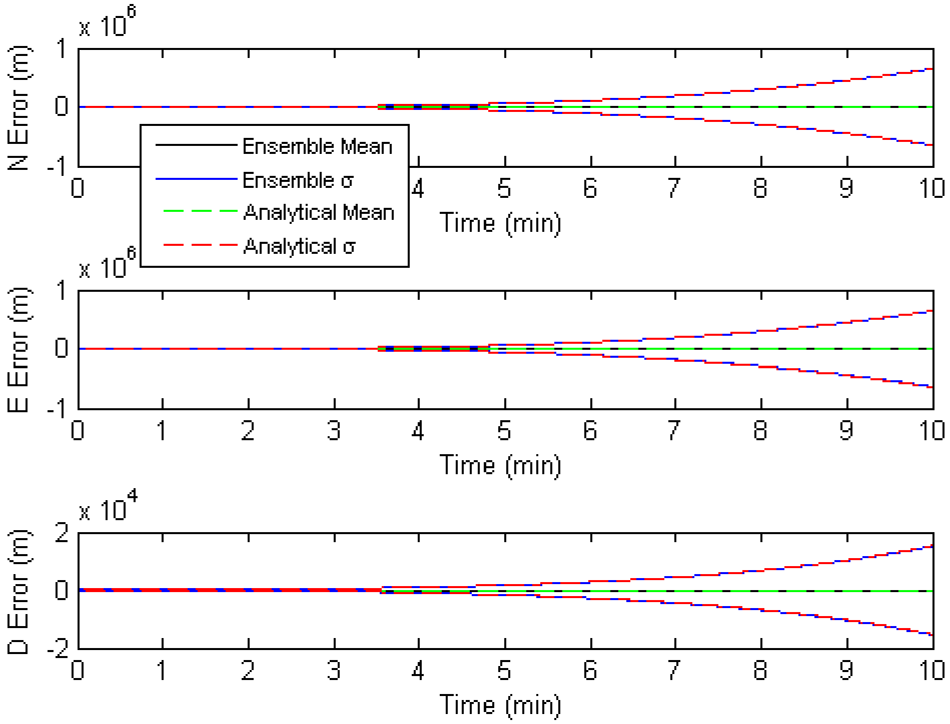

Figure 3.3. Monte Carlo Simulation of 10,000 runs for Commercial Grade INS Position Error for the n-frame North, East, Down axes respectively.

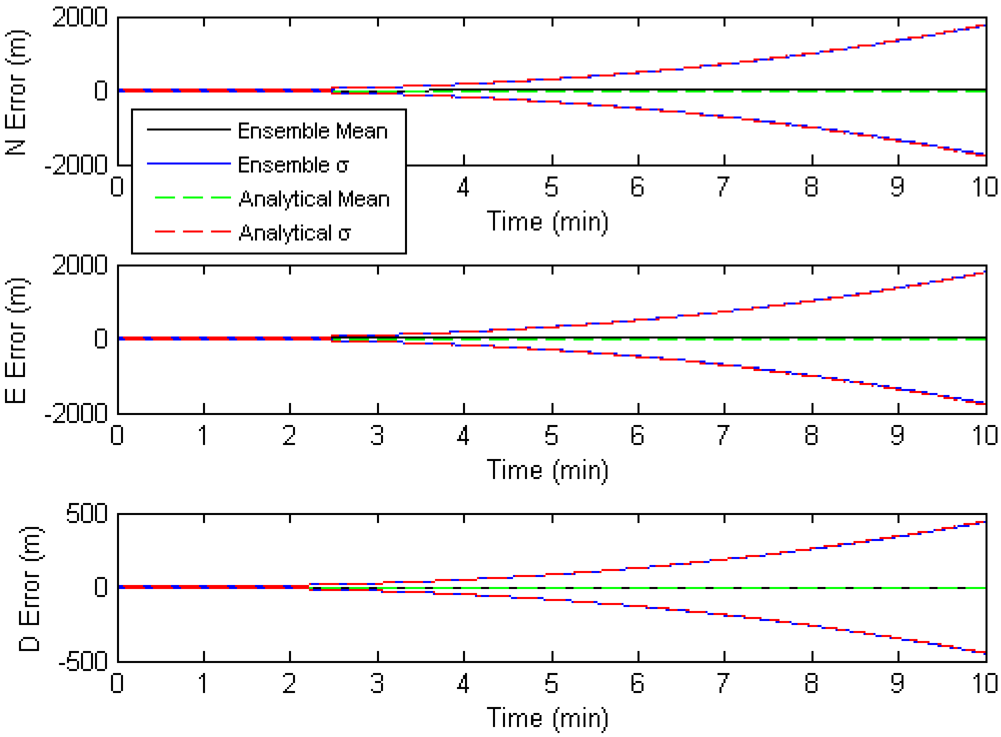

Figure 3.4. Monte Carlo Simulation of 10,000 runs for Tactical Grade INS Position Error for the n-frame North, East, Down axes respectively.

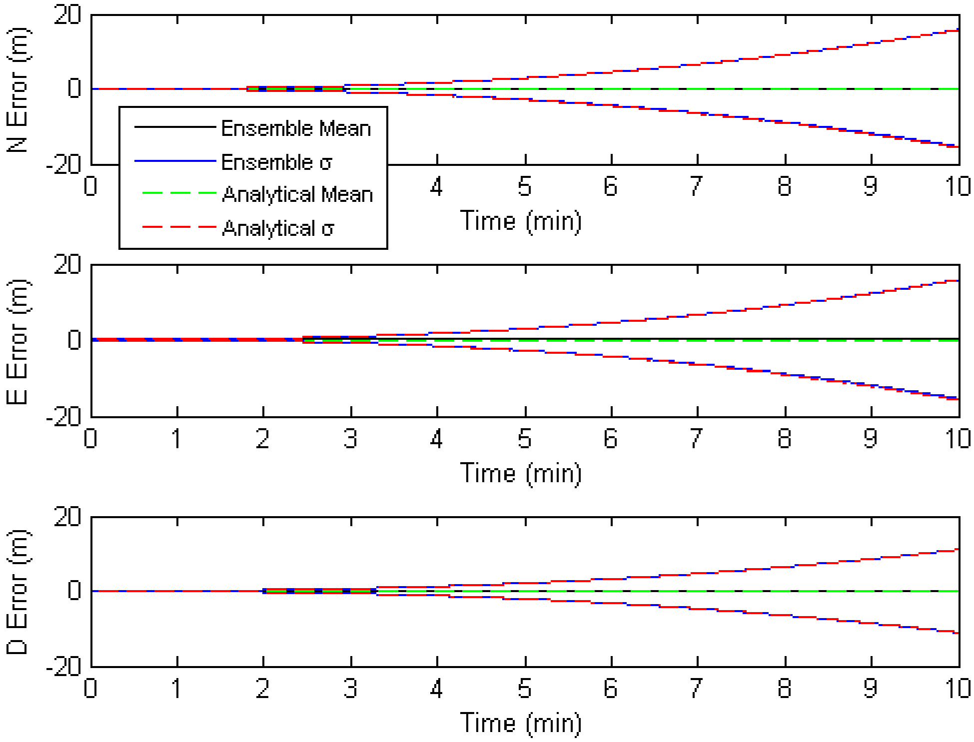

Figure 3.5. Monte Carlo Simulation of 10,000 runs for Navigation Grade INS Position Error for the n-frame North, East, Down axes respectively.

3.6 Measurement Model

For this research effort INS drift errors are corrected within an EKF through the use of lunar feature angle measurements obtained in the n-frame and a barometer.

Lunar Feature Angle Measurement Model.

Equation 3.30 shows the non-linear measurement model containing measurements $\mathbf{z}_{\text{opt},k}$, the measurement function $\mathbf{h}_{\text{opt}}(\cdot)$, and measurement noise $\mathbf{v}_{\text{opt},k}$ which is a white Gaussian noise process [21]. $\mathbf{R}_{\text{opt},k}$ is the measurement noise covariance matrix. The position states $\mathbf{p}_k$ are the input to the measurement function. The measurement function $\mathbf{h}_{\text{opt}}(\cdot)$ consists of two external angle measurements: azimuth η and elevation

ξ described in Equations 3.33 and 3.34 respectively. The angles are calculated based upon the relationship of the simulated vehicle position $\mathbf{p}_k$ to simulated lunar features T^{n} in the n-frame. $\mathbf{h}_{\mathrm{opt}}(\cdot)$ is constructed to allow for angles to be calculated based upon multiple features for batch updating denoted by index 1 to n with discrete times at index k.

$$\mathbf{z}_{\mathrm{opt},k} = \mathbf{h}_{\mathrm{opt}}(\mathbf{p}_k) + \mathbf{v}_{\mathrm{opt},k} \tag{3.30}$$

$$\mathbf{R}_{\mathrm{opt},k} = \mathrm{E}\big[\mathbf{v}_{\mathrm{opt},k}\mathbf{v}_{\mathrm{opt},k}^{\mathrm{T}}\big]_{2n\times 2n} \tag{3.31}$$

$$\mathbf{h}_{\mathrm{opt}}(\mathbf{p}_k) = \begin{bmatrix} \eta_{1,k} \\ \vdots \\ \eta_{n,k} \\ \xi_{1,k} \\ \vdots \\ \xi_{n,k} \end{bmatrix}_{2n\times 1} \tag{3.32}$$

η is determined by the slope of the vehicle position $(\mathbf{p}_{\mathrm{N}}, \mathbf{p}_{\mathrm{E}}, \mathbf{p}_{\mathrm{D}})$ in relation to the feature position $(T^{\mathrm{n}}_{\mathrm{N}}, T^{\mathrm{n}}_{\mathrm{E}}, T^{\mathrm{n}}_{\mathrm{D}})$ within the inverse tangent function along the horizontal E-N plane as shown in Equation 3.33 and Figure 3.6. The positive E-axis is 0π rads. ξ is determined based upon the slope of the vehicle position in relation to the feature position with the rise along the vertical D-axis and the run calculated as a line projection along the horizontal E-N plane as shown in Equation 3.34 and Figure 3.7.

$$\eta_k = \tan^{-1}\left(\frac{T^{\mathrm{n}}_{\mathrm{N}} - \mathbf{p}_{\mathrm{N},k}}{T^{\mathrm{n}}_{\mathrm{E}} - \mathbf{p}_{\mathrm{E},k}}\right) \tag{3.33}$$

$$\xi_k = \tan^{-1}\left(\frac{T^{\mathrm{n}}_{\mathrm{D}} - \mathbf{p}_{\mathrm{D},k}}{\sqrt{(T^{\mathrm{n}}_{\mathrm{E}} - \mathbf{p}_{\mathrm{E},k})^2 + (T^{\mathrm{n}}_{\mathrm{N}} - \mathbf{p}_{\mathrm{N},k})^2}}\right) \tag{3.34}$$

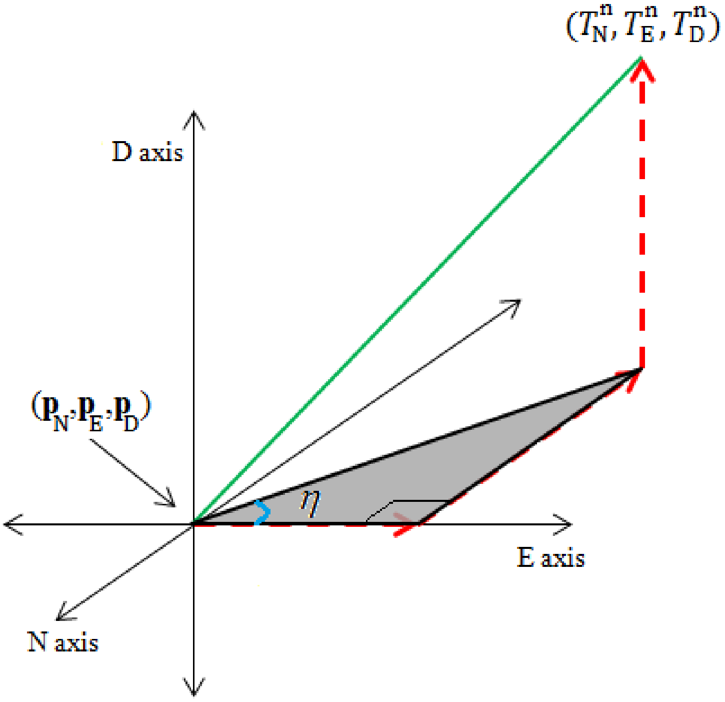

Figure 3.6. 3D Angle: E-N Plane.

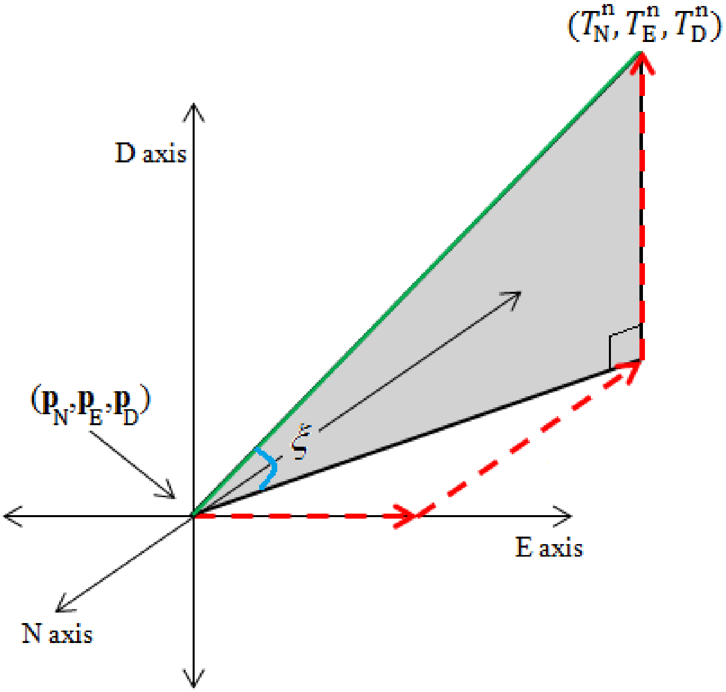

Figure 3.7. 3D Angle: D-axis and E-N Plane Projection.

For EKF estimation, simply inputing the non-linear measurement model into the filter will not work due to the linear nature of the Kalman gain and covariance update equations [21]. The angle measurements must be linearly approximated along the three orthogonal axes that comprise the n-frame. A first-order Taylor series expansion called a Jacobian is used to linearly approximate the non-linear measurement function as seen in Equation 3.36 [21]. Within the EKF algorithm, the Jacobian is determined for the estimated angles $\hat{\eta}$ and $\hat{\xi}$ which have been calculated based upon estimated position states $\hat{\mathbf{p}}_k$ shown in Equation 3.35.

$$\hat{\mathbf{p}}_k = \mathbf{p}_{\mathrm{INS},k} + \delta\hat{\mathbf{p}}_k \tag{3.35}$$

$$\mathbf{H}_{\mathrm{opt},k} = \frac{\partial}{\partial\hat{\mathbf{p}}_k}\mathbf{h}_{\mathrm{opt}}(\hat{\mathbf{p}}_k) \tag{3.36}$$

$\mathbf{H}_{\mathrm{opt},k}$ represents the measurement matrix comprised of Jacobians required for the EKF update equations. η and ξ only give observability along the position states.

$$\mathbf{H}_{\mathrm{opt},k} = \begin{bmatrix} \frac{\partial}{\partial\hat{\mathbf{p}}_{\mathrm{N},k}}\hat{\eta}_{1,k} & \frac{\partial}{\partial\hat{\mathbf{p}}_{\mathrm{E},k}}\hat{\eta}_{1,k} & 0 & 0 & \dots & 0 \\ \vdots & \vdots & \vdots & \vdots & \ddots & \vdots \\ \frac{\partial}{\partial\hat{\mathbf{p}}_{\mathrm{N},k}}\hat{\eta}_{n,k} & \frac{\partial}{\partial\hat{\mathbf{p}}_{\mathrm{E},k}}\hat{\eta}_{n,k} & 0 & 0 & \dots & 0 \\ \frac{\partial}{\partial\hat{\mathbf{p}}_{\mathrm{N},k}}\hat{\xi}_{1,k} & \frac{\partial}{\partial\hat{\mathbf{p}}_{\mathrm{E},k}}\hat{\xi}_{1,k} & \frac{\partial}{\partial\hat{\mathbf{p}}_{\mathrm{D},k}}\hat{\xi}_{1,k} & 0 & \dots & 0 \\ \vdots & \vdots & \vdots & \vdots & \ddots & \vdots \\ \frac{\partial}{\partial\hat{\mathbf{p}}_{\mathrm{N},k}}\hat{\xi}_{n,k} & \frac{\partial}{\partial\hat{\mathbf{p}}_{\mathrm{E},k}}\hat{\xi}_{n,k} & \frac{\partial}{\partial\hat{\mathbf{p}}_{\mathrm{D},k}}\hat{\xi}_{n,k} & 0 & \dots & 0 \end{bmatrix}_{2n\times 15} \tag{3.37}$$

For $\hat{\eta}$, the Jacobians along the north and east position states are represented below.

$$\mathbf{H}_{\mathrm{opt},\hat{\mathbf{p}}_{\mathrm{N},k}} = \frac{\partial}{\partial\hat{\mathbf{p}}_{\mathrm{N},k}}\hat{\eta}_{1,k} = \frac{-(T^{\mathrm{n}}_{\mathrm{E}} - \hat{\mathbf{p}}_{\mathrm{E},k})}{(T^{\mathrm{n}}_{\mathrm{E}} - \hat{\mathbf{p}}_{\mathrm{E},k})^2 + (T^{\mathrm{n}}_{\mathrm{N}} - \hat{\mathbf{p}}_{\mathrm{N},k})^2} \tag{3.38}$$

$$\mathbf{H}_{\mathrm{opt},\hat{\mathbf{p}}_{\mathrm{E},k}} = \frac{\partial}{\partial\hat{\mathbf{p}}_{\mathrm{E},k}}\hat{\eta}_{1,k} = \frac{(T^{\mathrm{n}}_{\mathrm{N}} - \hat{\mathbf{p}}_{\mathrm{N},k})}{(T^{\mathrm{n}}_{\mathrm{E}} - \hat{\mathbf{p}}_{\mathrm{E},k})^2 + (T^{\mathrm{n}}_{\mathrm{N}} - \hat{\mathbf{p}}_{\mathrm{N},k})^2} \tag{3.39}$$

For $\hat{\xi}$, the Jacobians along the north, east, and down position states are represented below.

$$\mathbf{H}_{\text{opt},\hat{\mathbf{p}}_{\text{N},k}} = \frac{\partial}{\partial \hat{\mathbf{p}}_{\text{N},k}} \hat{\xi}_{1,k} = \frac{-(\hat{\mathbf{p}}_{\text{N},k} - T^{\text{n}}_{\text{N}})(T^{\text{n}}_{\text{D}} - \hat{\mathbf{p}}_{\text{D},k})}{\sqrt{(T^{\text{n}}_{\text{E}} - \hat{\mathbf{p}}_{\text{E},k})^2 + (T^{\text{n}}_{\text{N}} - \hat{\mathbf{p}}_{\text{N},k})^2}\,((T^{\text{n}}_{\text{E}} - \hat{\mathbf{p}}_{\text{E},k})^2 + (T^{\text{n}}_{\text{N}} - \hat{\mathbf{p}}_{\text{N},k})^2 + (T^{\text{n}}_{\text{D}} - \hat{\mathbf{p}}_{\text{D},k})^2)} \tag{3.40}$$

$$\mathbf{H}_{\text{opt},\hat{\mathbf{p}}_{\text{E},k}} = \frac{\partial}{\partial \hat{\mathbf{p}}_{\text{E},k}} \hat{\xi}_{1,k} = \frac{-(\hat{\mathbf{p}}_{\text{E},k} - T^{\text{n}}_{\text{E}})(T^{\text{n}}_{\text{D}} - \hat{\mathbf{p}}_{\text{D},k})}{\sqrt{(T^{\text{n}}_{\text{E}} - \hat{\mathbf{p}}_{\text{E},k})^2 + (T^{\text{n}}_{\text{N}} - \hat{\mathbf{p}}_{\text{N},k})^2}\,((T^{\text{n}}_{\text{E}} - \hat{\mathbf{p}}_{\text{E},k})^2 + (T^{\text{n}}_{\text{N}} - \hat{\mathbf{p}}_{\text{N},k})^2 + (T^{\text{n}}_{\text{D}} - \hat{\mathbf{p}}_{\text{D},k})^2)} \tag{3.41}$$

$$\mathbf{H}_{\text{opt},\hat{\mathbf{p}}_{\text{D},k}} = \frac{\partial}{\partial \hat{\mathbf{p}}_{\text{D},k}} \hat{\xi}_{1,k} = \frac{-\sqrt{(T^{\text{n}}_{\text{E}} - \hat{\mathbf{p}}_{\text{E},k})^2 + (T^{\text{n}}_{\text{N}} - \hat{\mathbf{p}}_{\text{N},k})^2}}{(T^{\text{n}}_{\text{E}} - \hat{\mathbf{p}}_{\text{E},k})^2 + (T^{\text{n}}_{\text{N}} - \hat{\mathbf{p}}_{\text{N},k})^2 + (T^{\text{n}}_{\text{D}} - \hat{\mathbf{p}}_{\text{D},k})^2} \tag{3.42}$$

For this research effort, the standard deviation σ_{opt} for lunar feature angle measurement noise $\mathbf{v}_{\text{opt},k}$ is set as the angular resolution $\Delta\theta_{\text{q}}$ of features in an image constrained by lens diffraction as discussed in Section 2.5. To design the camera detector to the diffraction limit, an assumption was made based on a common optical design that sampling should be equal to the diffraction limited spot size. With this stipulation, the Airy disk diameter $2q_1$ can be assumed to equal the pixel size $\Delta\ell$ for the diffraction limited system used in this research effort as shown in Equation 3.43 and Figure 3.8. This assumption places the angular resolution within ±1 pixel. To obtain σ_{opt}, Equation 3.44 presents the relationship between the pixel size and the focal length used to derive $\Delta\theta_{\text{q}}$.

$$2q_1 \approx \Delta\ell \tag{3.43}$$

$$\Delta\theta_{\text{q}} \approx \frac{\Delta\ell}{2f} \tag{3.44}$$

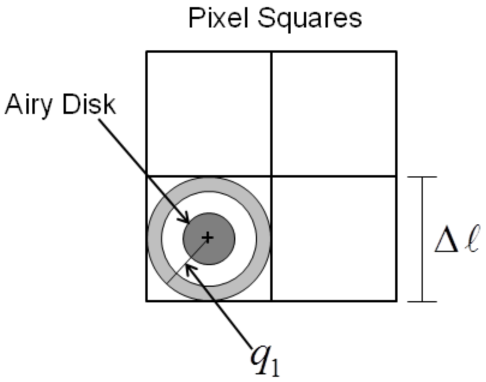

Figure 3.8. Diffraction Limited Spot diameter assumed equal to Pixel Size.

Barometer Measurement Model.

The down position state is completely observed by a barometer which measures the aircraft's altitude as shown in Equations 3.45 and 3.46 [5]. For this research effort, the barometer measurements are brought into the EKF every 60 seconds.

$$\mathbf{z}_{\text{baro},k} = \mathbf{H}_{\text{baro},k}\mathbf{x}_k + \mathbf{v}_{\text{baro},k} \tag{3.45}$$

$$\mathbf{H}_{\text{baro},k} = \begin{bmatrix} 0 & 0 & 1 & 0 & \dots & 0 \end{bmatrix}_{1\times 15} \tag{3.46}$$

The barometer measurement noise $\mathbf{v}_{\text{baro},k}$ is a white Gaussian process. The standard deviation σ_{baro} for the barometer measurement noise is set at ±5m. The measurement covariance matrix $\mathbf{R}_{\text{baro},k}$ is represented below.

$$\mathbf{R}_{\text{baro},k} = \mathrm{E}\big[\mathbf{v}_{\text{baro},k}\mathbf{v}_{\text{baro},k}^{\mathrm{T}}\big]_{15\times 15} \tag{3.47}$$

3.7 Feature Design and Implementation

To simulate features derived from the lunar surface, randomized azimuth and elevation angles are first generated in vectors $\boldsymbol{\theta}_{\text{feat}}$ and $\boldsymbol{\psi}_{\text{feat}}$ using the Equations 3.48 and 3.49 respectively. These equations represent a common practice in placing points at random locations along a spherical surface based on the spherical coordinate system equations. $\mathbf{m}_{\text{feat}}$ and $\mathbf{n}_{\text{feat}}$ are vectors containing random numbers with range between 0 and 1. The angles are then processed through the MATLAB® function *sph2cart* with the Moon's radius to gain cartesian coordinate feature positions $(T^{\text{e}}_{\text{X}}, T^{\text{e}}_{\text{Y}}, T^{\text{e}}_{\text{Z}})$ in the ECEF frame. The cartesian coordinates are then translated to the Moon's position in orbit based upon the orbital parameters in Section 2.6 providing an approximation of lunar surface features. Figures 3.9-3.11 present 1000 simulated lunar features as green x's and the Moon as a red spheroid.

$$\boldsymbol{\theta}_{\text{feat}} = \mathbf{m}_{\text{feat}}\pi \tag{3.48}$$

$$\boldsymbol{\psi}_{\text{feat}} = \sin^{-1}(-1 + 2\mathbf{n}_{\text{feat}}) \tag{3.49}$$

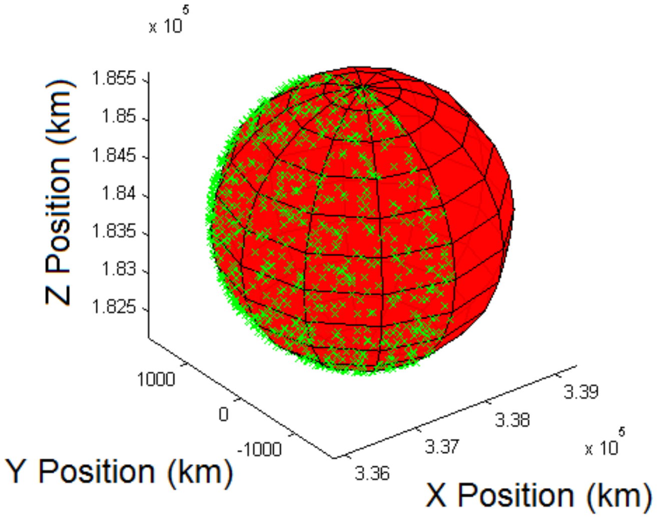

Figure 3.9. ECEF Frame: Moon and 1000 Random Lunar Features.

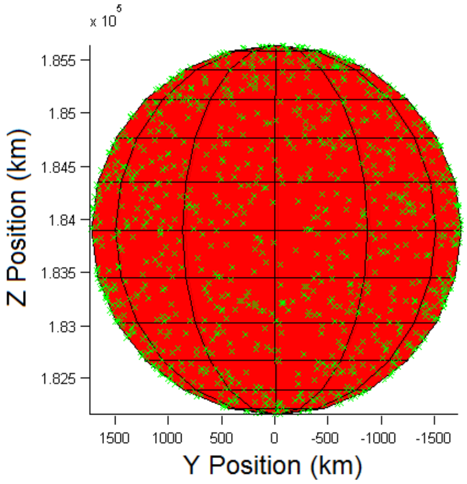

Figure 3.10. ECEF Frame: Y-Z Plane. Moon and 1000 Random Lunar Features.

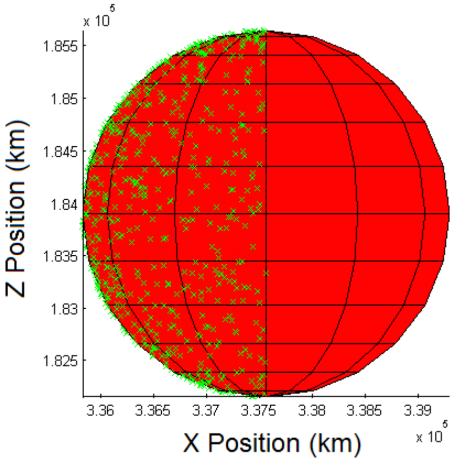

Figure 3.11. ECEF Frame: X-Z Plane. Moon and 1000 Random Lunar Features.

3.8 EKF Implementation

This section provides further details about the system algorithm setup and EKF implementation. To begin, orientation of the aircraft's truth trajectory $\mathbf{x}_k$ and the INS trajectory $\mathbf{x}_{\mathrm{INS},k}$ is needed in the context of traveling along the Earth's surface. For this reason, the algorithm requires a starting position in geodetic coordinates: latitude, longitude, and altitude (L, λ, h). The initial geodetic coordinate incorporation into the $\mathbf{C}_{\mathrm{n}}^{\mathrm{e}}$ DCM helps to orient the fixed n-frame of the aircraft's trajectory to the Earth's surface. Outside of EKF error state estimation propagation, the initial geodetic coordinate is solely used in the $\mathbf{C}_{\mathrm{n}}^{\mathrm{e}}$ DCM to orient the n-frame due to the small aircraft trajectory modeled. The resulting posture, places the fixed n-frame's N and E axes as a plane tangent to the Earth's surface resting atop the starting geodetic coordinate where the D-axis points toward the Earth's center.

An overall system representation for Lunar Vision Aided Navigation with Inertial Navigation System is shown in Figure 3.12. The figure shows the INS trajectory $\mathbf{x}_{\mathrm{INS},k}$ is rotated from the n-frame into geodetic coordinates and input into the EKF to estimate INS error states $\delta\hat{\mathbf{x}}_k$ and a trajectory estimate $\hat{\mathbf{x}}_k$ in the n-frame. The simulated lunar features are in the e-frame to best represent their orientation to Earth. The lunar features are randomized along the Moon's near side surface facing Earth. To perform the $\hat{\eta}$ and $\hat{\xi}$ angle calculations and the Jacobians in Equations 3.38-3.42 within the EKF, the features and the trajectory estimate need to both be within the same frame. To accomplish this, the lunar features are rotated into the n-frame based upon the initial geodetic coordinate. Once the EKF estimation is complete, the estimated trajectory $\hat{\mathbf{x}}_k$ can be rotated into the e-frame to ECEF coordinates or converted to geodetic coordinates to gain knowledge of the vehicle trajectory along the surface of the Earth.

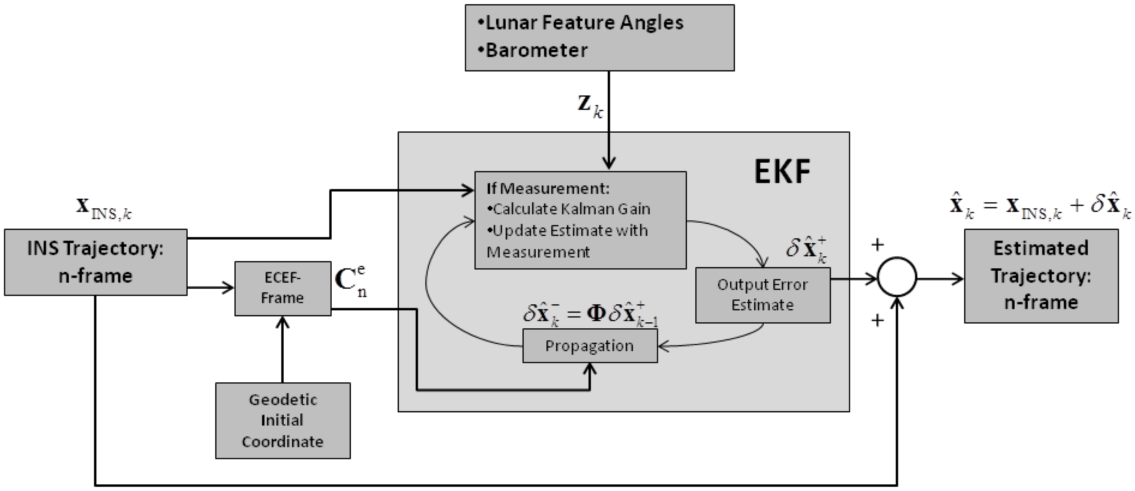

Figure 3.12. Lunar Vision Aided Navigation with Ineriital Navigation System [5].

It should be noted that based on the nature of the Jacobians described in Section 3.6, an angle obtained by a vehicle observing a feature at infinity within the same reference frame will appear to be constant at 90°. The lack of change in the observed angle will cause the Jacobians to converge to zero resulting in an observability loss of the vehicle's position error states. In this research effort, however, the fixed n-frame along the Earth's surface and the lunar feature finite distances allows for observability in the position states. The down position state is observed fully by a barometer. Thus, INS drift error is corrected in all position states. The loss of position state observability by a decrease in Jacobians based on feature distance will be presented Chapter 4. Also in Chapter 4, a singularity in the spherical coordinate system where this concept does not hold true will be shown as well.

3.9 Summary

Chapter 3 provided the research methodology to obtain the results in Chapter 4. The truth model, error state motion model, measurement model, and lunar feature model were presented. The error state motion model validation was shown, and the EKF implementation was discussed.

IV. Results and Analysis of the Theoretical Limits of Lunar Vision Aided Navigation with INS

4.1 Introduction

This chapter presents the results from the research methodology detailed in Chapter 3. The purpose of this research was to simulate and analyze INS drift correction by lunar feature angle measurements. Various scenarios were considered in order to better understand the impact that lunar feature aided navigation would theoretically have on INS drift correction. The affect of lunar feature aided navigation on different INS grades is shown in Section 4.2. Measurement noise effects from camera specifications on INS drift correction by lunar feature angle measurements are presented in Section 4.3. Feature quantity effects are shown in Section 4.4. Section 4.5 covers the effect of lunar features at increasing distances and different lunar orbit geometries. Section 4.6 presents the chapter summary.

It must be stated that for the scenarios in Chapter 4, lunar vision aided navigation with INS was simulated under an idealized set of parameters where measurement noise effects are only considered. Therefore, the results in Chapter 4 are not indicative of actual performance by lunar vision aided navigation with INS but present analysis on the trade spaces resulting from changes to INS grade, camera image array pixel sizes, camera lens focal length, lunar feature quantity, and lunar feature distance and geometry. The many assumptions which allow the aforementioned model simplification are detailed in Section 1.4.

For the following scenarios, unless stated otherwise, the parameters in Table 4.1 are set for the simulated trajectory runs. The default camera measurement noise standard deviation σ_{opt} is set at 0.011mrads based on the angular resolution $\Delta\theta_{\mathrm{q}}$ of a Prosilica GE1660C CCD camera with a 253mm focal length lens. A barometer aids the down position state with a measurement noise standard deviation σ_{baro} set at ±5m.

Table 4.1. Default Case Trajectory Parameters

Samples	Time	Start Pos* ($L\lambda h$)	INS	Prop* Time	# of Features	Camera Update	Baro Update
30	10min	(0°,0°,0m)	Tactical	1s	100	4s	60s

* Prop - Propagation, Pos - Position

Figures 4.1-4.4 present the default orientation of the Moon to the Earth in the ECEF frame. The blue sphere represents the Earth and the dark red smaller sphere represents the Moon. In the default orientation, the Moon is at its highest inclination to the Earth's equator at 28.58°. The Moon lies at an offset above the X-axis. In reference to the true trajectory in the n-frame along the Earth's surface, the course of the aircraft travels in a circle with radius 20km along the N-E plane for every sample in the default case. The height of the aircraft varies based upon the FOGM acceleration model detailed in Section 3.3.

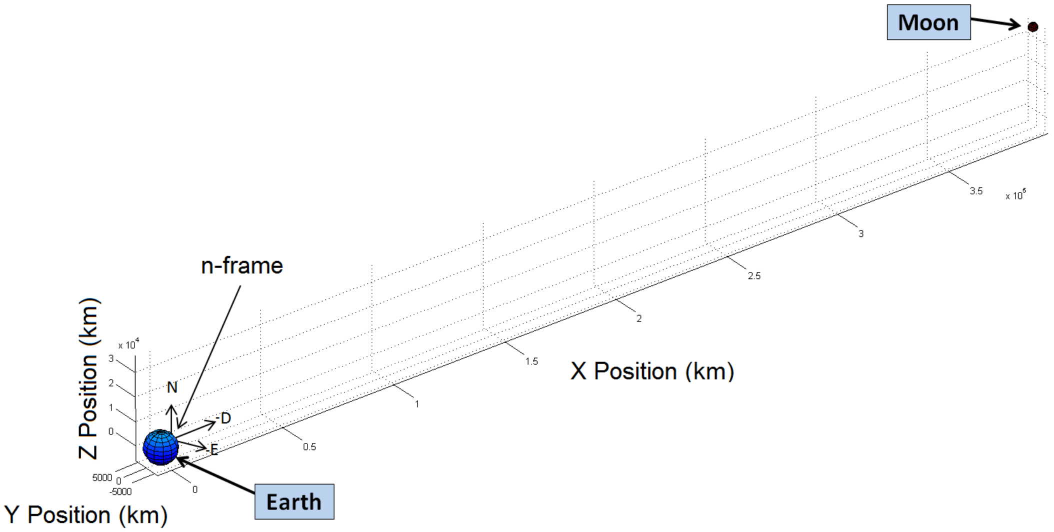

Figure 4.1. ECEF Frame. Earth and Moon with fixed local level n-frame (Not to Scale).

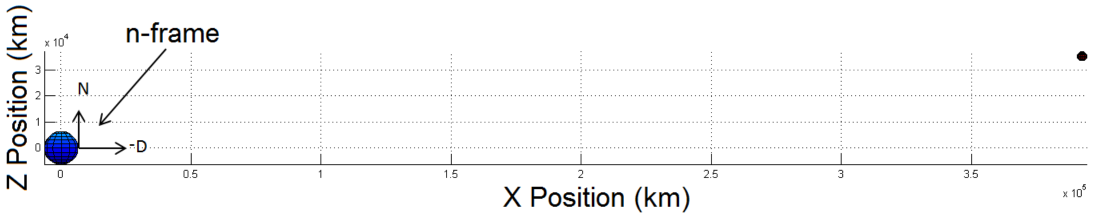

Figure 4.2. ECEF Frame: X-Z Plane. Earth and Moon with fixed local level n-frame (Not to Scale).

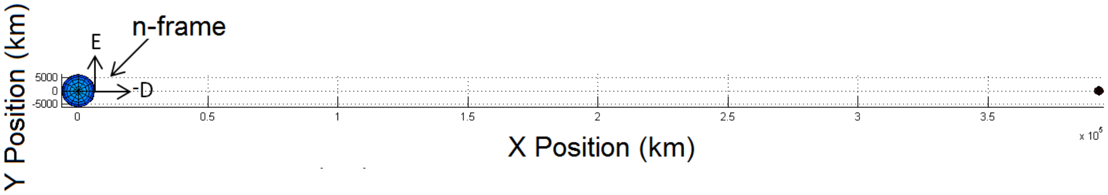

Figure 4.3. ECEF Frame: X-Y Plane. Earth and Moon with fixed local level n-frame (Not to Scale).

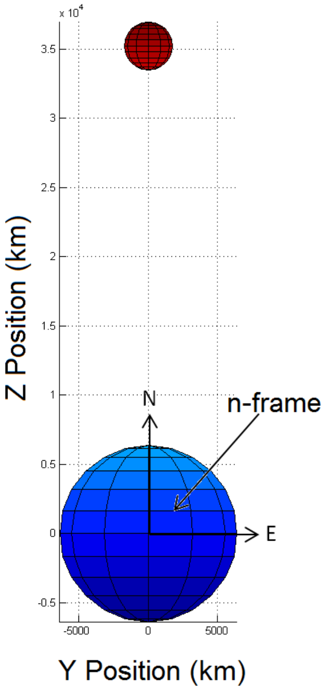

Figure 4.4. ECEF Frame: Y-Z Plane. Earth and Moon with fixed local level n-frame (Not to Scale).

4.2 INS Grade Testing

This section presents INS drift correction aided by lunar feature angles against varying grades of INS. All realizations were ran using the parameters in Table 4.1 with 100 features, and the camera measurement noise standard deviation was kept at 0.011mrads. Figures 4.5-4.7 show significant decrease between the position state error for a stand alone INS when compared to the position state errors from an INS aided by lunar vision angle measurements. In addition, the position state errors show significant decrease with each change in INS grade when comparing Figures 4.5b, 4.6b, and 4.7b. For the Commercial Grade INS in Figure 4.5b, the north position state error variance is at ±58.96m and the east position state error variance is at ±25.85m. The down position state error variance is sharply high at ±77.62m even with the barometer having full observability of the down position state. For the Navigation Grade INS in Figure 4.7b, the error significantly decreases for the position states with error variances at ±2.946m for the north position state, ±0.9805m for the east position state, and ±2.328m for down position state.

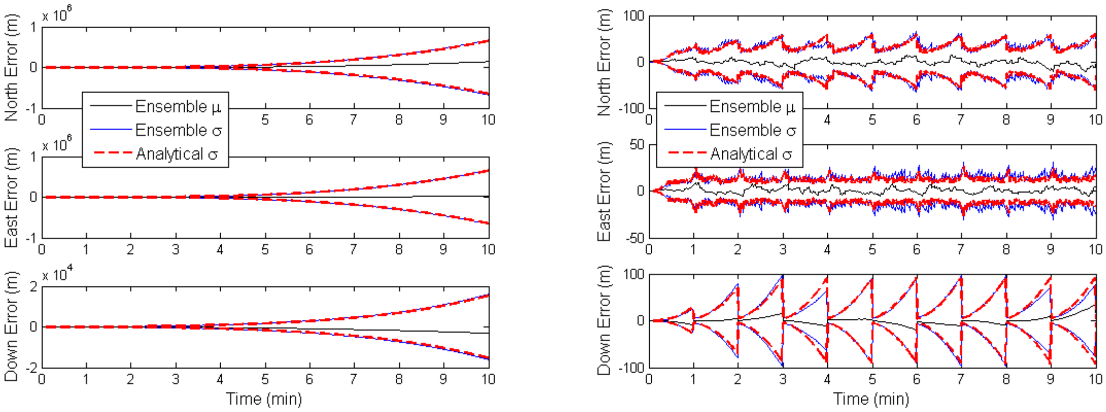

(a) No Lunar Vision Aiding

(b) Lunar Vision Aiding

Figure 4.5. Commercial Grade INS with 100 Features. Position State Error for the n-frame North, East, Down States respectively.

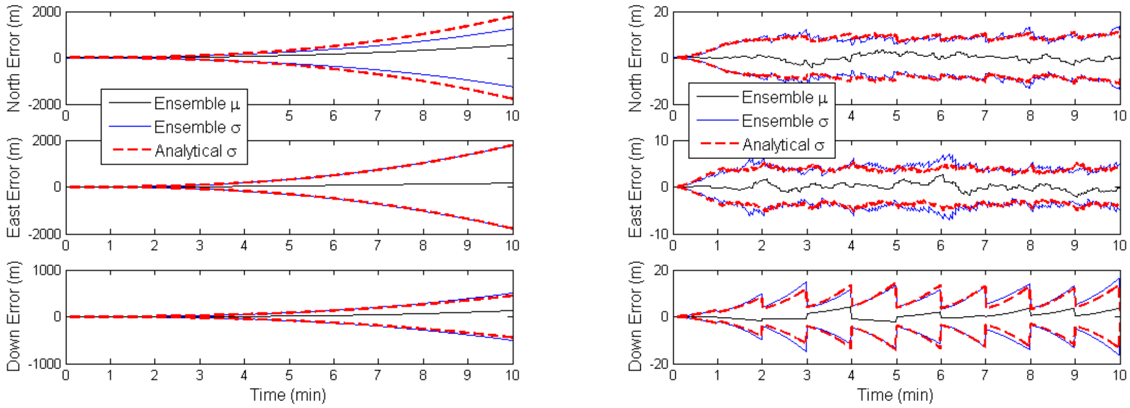

(a) No Lunar Vision Aiding

(b) Lunar Vision Aiding

Figure 4.6. Tactical Grade INS with 100 Features. Position State Error for the n-frame North, East, Down States respectively.

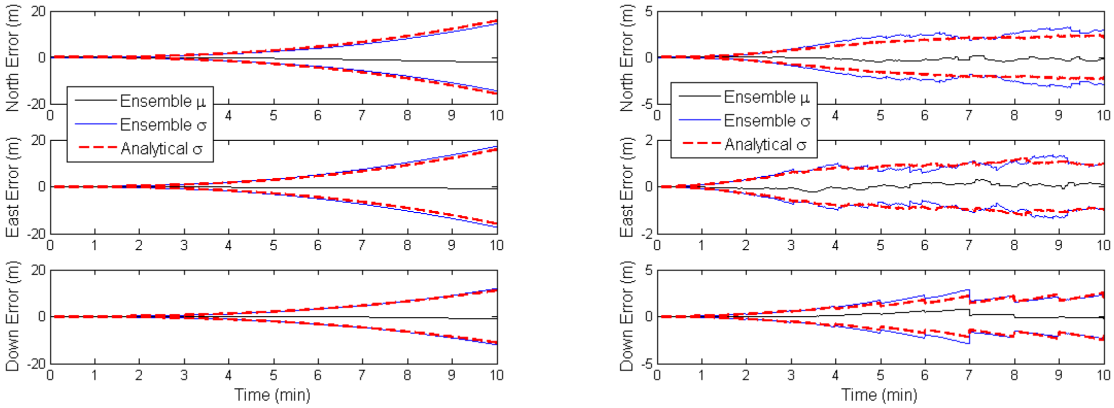

(a) No Lunar Vision Aiding

(b) Lunar Vision Aiding

Figure 4.7. Navigation Grade INS with 100 Features. Position State Error for the n-frame North, East, Down States respectively.

4.3 Camera Specifications Testing

The effect of camera measurement noise $\mathbf{v}_{\text{opt},k}$ on an EKF estimating INS errors aided by lunar feature angle measurements can be predicted. A relationship exists within an EKF whereby the measurement noise amount can cause the EKF to rely more on the current error state estimate or rather on the correction to the current error state estimate brought about by the incorporated measurement $\mathbf{z}_k$ as shown in Section 2.4.

An EKF incorporating measurements with high noise will cause a low Kalman gain. The low Kalman gain will decrease the amount of correction by the measurements causing the EKF to rely more on the current error state estimate. For this research effort, Figures 3.3-3.5 in Section 3.5 present INS error states without correction. For lower measurement noises, the error state estimates will be much closer to the true error states relating to higher accuracy in estimation. Lower measurement noises allow for a higher quality estimate correction and a Kalman gain which allows for the full proportion of the near accurate correction to update the current state estimate.

For this research effort, the standard deviation σ_{opt} of the camera measurement noise that is added to the observed angle measurements is obtained from the angular resolution $\Delta\theta_{\text{q}}$ of a diffraction limited system which is a fixed camera mounted to an aircraft body frame. It was assumed that the diameter of a diffraction limited spot $2q_1$ is set equal to the pixel size $\Delta\ell$ of the camera's image array so as to constrain the image uncertainty to ±1 pixels. Section 3.6 presented a relationship connecting pixel size $\Delta\ell$ to the angular resolution $\Delta\theta_{\text{q}}$. Table 4.2 presents a sweep of pixel sizes and the coinciding angular resolution to test INS drift correction by lunar feature-aided navigation against. The focal length is set at 253mm. To place the pixel sizes into perspective, camera image sensor pixel sizes were obtained from commercial camera

Table 4.2. Measurement Noise $\mathbf{v}_k$

Measurement Noise Level	$\Delta\ell$ (μm)	$\mathbf{v}_{\text{opt},k}$ (mrads)
1	1000	2
2	100	0.2
3	10	0.02
4	1	0.002

specifications. For the SCI High Accuracy Star Tracker 2 image sensor, the pixel size was 18μm. This is near the pixel size for the Prosilica GE1660C camera which was 5.5μm.

From the previous assertions, Figures 4.8-4.11 present the position state error in the n-frame with corrections from the angle measurements. An accompanying single run of an estimated trajectory tracking a true trajectory is presented as well in the right subfigure within Figures 4.8-4.11. All of the trajectories shown are based upon the parameters listed in Table 4.1.

With each decrease in pixel size and measurement noise, the position state error decreases for the north and east position states. In Figure 4.8a, north position state error variance is ±396m and east position state error variance is ±216.5m based on a measurement noise of 2mrads and pixel size at 1000μm. In contrast, Figure 4.11a presents north position error variance at ±8.33m and ±1.54m for the east position state for a measurement noise of 0.002mrads and pixel size 1μm. Based upon this information, the results confirm the predicted increase in state error estimation accuracy based upon decreasing pixel size within this system model.

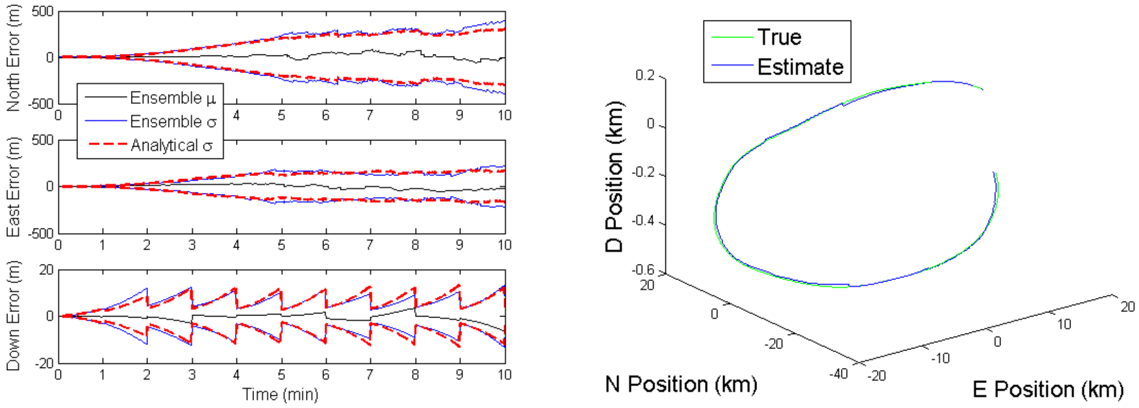

(a) Position State Error for the n-frame North, East, Down axes respectively

(b) Estimated vs. True Trajectory

Figure 4.8. Pixel Size: 1000μm and Measurement Noise: 2mrads.

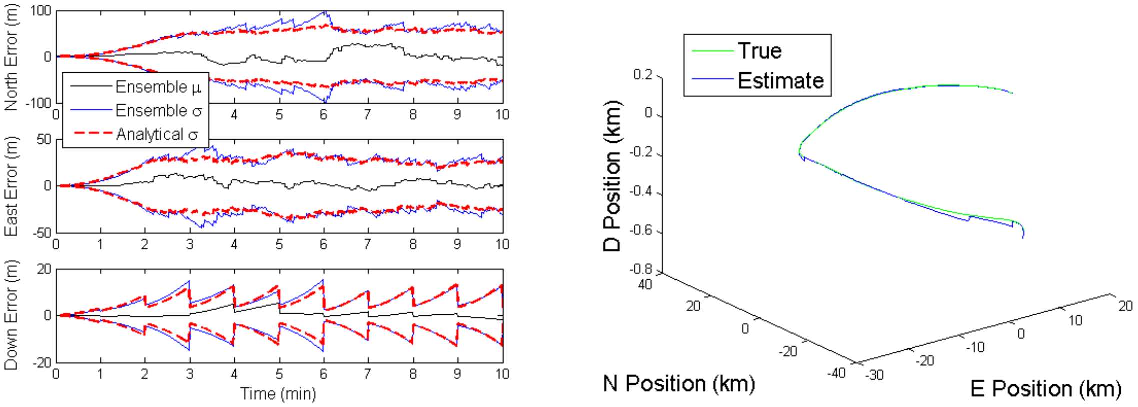

(a) Position State Error for the n-frame North, East, Down axes respectively

(b) Estimated vs. True Trajectory

Figure 4.9. Pixel Size: 100μm and Measurement Noise: 0.2mrads.

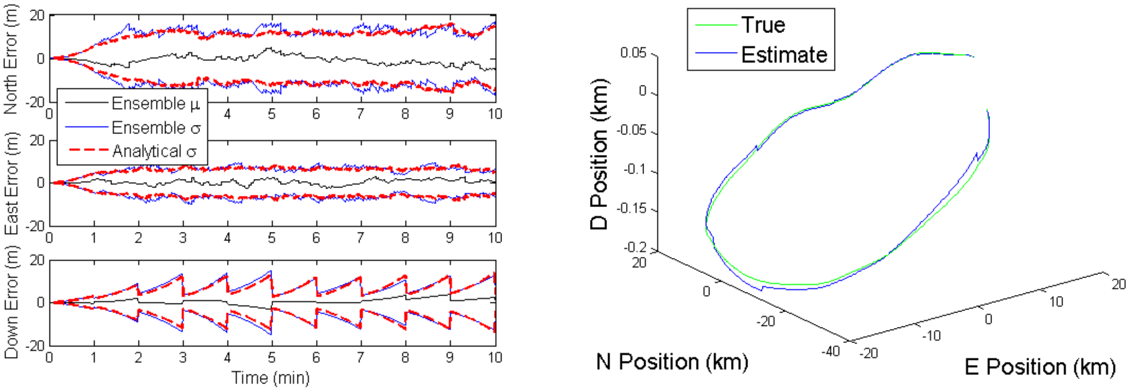

(a) Position State Error for the n-frame North, East, Down axes respectively

(b) Estimated vs. True Trajectory

Figure 4.10. Pixel Size: 10μm and Measurement Noise: 0.02mrads.

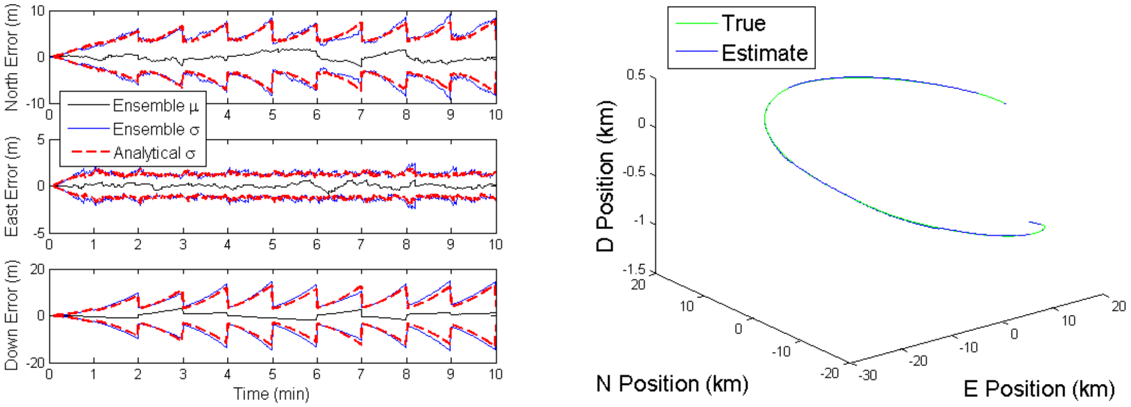

(a) Position State Error for the n-frame North, East, Down axes respectively

(b) Estimated vs. True Trajectory

Figure 4.11. Pixel Size: 1μm and Measurement Noise: 0.002mrads.

Commercial Camera Lenses.

For the below scenarios, the parameters from a commercial camera and various lenses were obtained to observe their behavior in INS drift correction by lunar vision aided navigation. The trajectory runs followed the parameters listed in Table 4.1. The camera used in the simulations was a Prosilica GE1660C CCD Camera with a pixel size listed in the maintenance guide as 5.5μm×5.5μm. From the relationship established in Section 3.6 between lens focal length f and the angular measurement noise standard deviation σ_{opt}, a pattern can be shown that as f increases the σ_{opt} decreases. This results in a better trajectory estimation within this model. Table 4.3 presents the lens parameters for lenses that are compatible with the c-mount 2/3" optical format of the Prosilica GE1660C CCD camera.

The image array is rectangular and has an associated rectangular field of view (FOV) with width angle α_{w} and height angle α_{h}. Based on the field of view equations in Section 2.5, the planar area of the observed world scene by the camera can be calculated as shown in the last column listing the observed world scene width $\mathbf{w}_{\text{scene}}$

and height $\mathbf{h}_{\text{scene}}$ parameters. The first two lens FOV areas listed can completely view the Moon's planar projection within their width and height parameters. The Moon's planar projection in the world scene viewed by the camera appears as a circle with diameter 3475km. The FOV area of the Cinetel III Telephoto Lens falls short of completely viewing the planar projection of the Moon. However, the zoom capabilities of the Cinetel III Telephoto Lens with focal length 1000mm allows for a much closer view of the Moon's features leading to a smaller measurement noise $\mathbf{v}_{\text{opt},k}$ and a tighter estimate.

Table 4.3. Commercial Lens Parameters

Camera Lens	**Focal Length (mm)**	σ_{opt}	**f-number**	**Lens Diameter (mm)**	$\alpha_{\text{h}}(^\circ)$	$\alpha_{\text{w}}(^\circ)$	**FOV Area (km)**
Tamron 23FM50SP	50	0.055	f/1.4	35.7	7.6	10.06	$67,654.4\times50,740.8$
Fujinon 22x Telephoto Zoom Lens	253	0.011	f/1.6	158.12	1.5	2	$13,370.4\times10,027.83$
Cinetel III Telephoto Lens	1000	0.003	f/5.6	178.57	0.4	0.5	3,382.72×2,537.04

Figures 4.12-4.14 present the position state error based upon the Prosilica GE1660C CCD Camera with the lenses listed in Table 4.3 and the associated measurement noise σ listed in the respective figure captions. In Figure 4.12a the north position state error variance is at ±28.67m and the east position state error variance is at ±11.25m. With the decrease in measurement noise and the increase in focal length to obtain a closer view of the Moon's features, Figure 4.14a shows the north position state error variance decreasing to ±6.42m and the east position state error variance decreasing to ±2.347m.

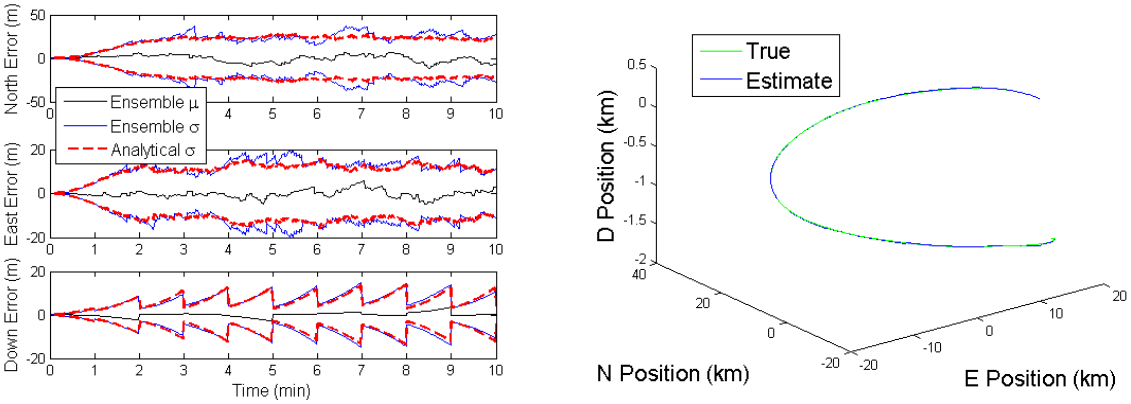

(a) Position State Error for the n-frame North, East, Down axes respectively

(b) Estimated vs. True Trajectory

Figure 4.12. Focal Length: 50mm and Measurement Noise σ: 0.055mrads.

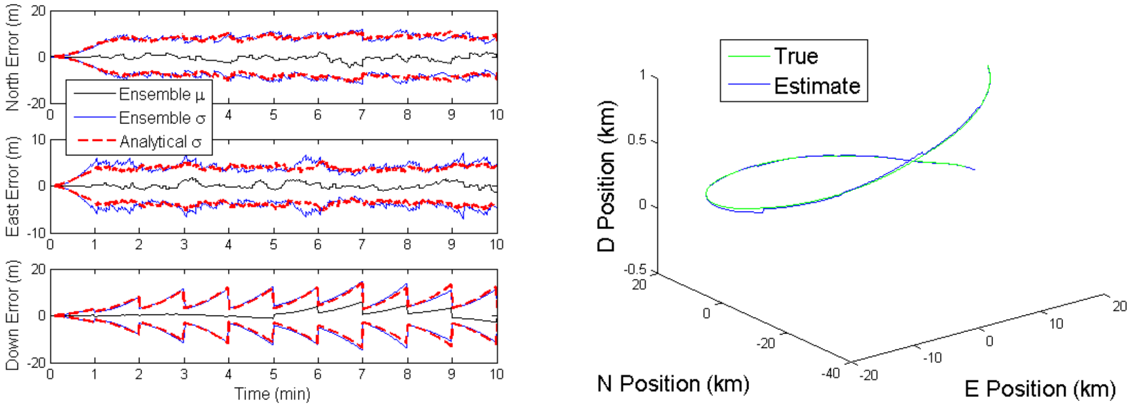

(a) Position State Error for the n-frame North, East, Down axes respectively

(b) Estimated vs. True Trajectory

Figure 4.13. Focal Length: 253mm and Measurement Noise σ: 0.011mrads.

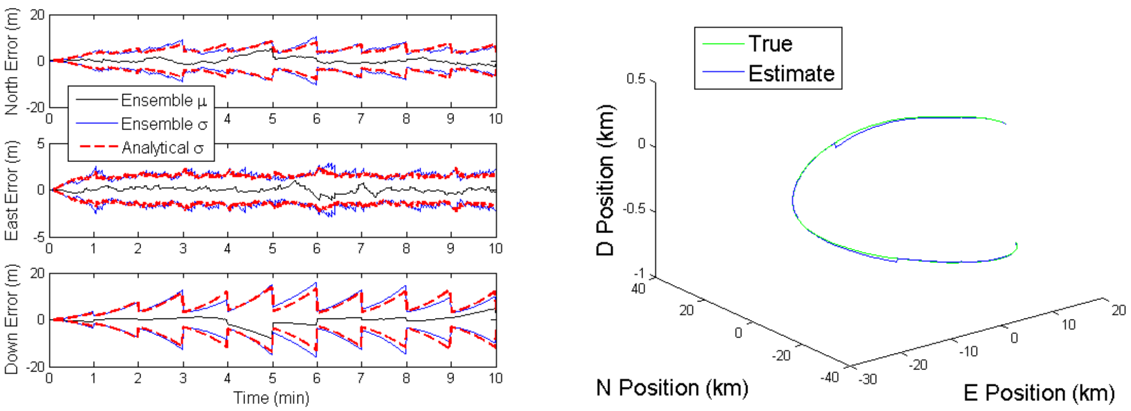

(a) Position State Error for the n-frame North, East, Down axes respectively

(b) Estimated vs. True Trajectory

Figure 4.14. Focal Length: 1000mm and Measurement Noise σ: 0.003mrads.

4.4 Feature Quantity Testing

The following section explores the accuracy of the trajectory estimation predicated on the amount of lunar features observed. Based upon the EKF algorithm, as a batch angle measurement update increases in the number of angles measured, the measurement model $\mathbf{z}_k$ increases and allows for multiple angles to be used in creating the estimate correction and provides multiple position state observabilities in the measurement matrix $\mathbf{H}_k$. The combination of the Kalman gain and the residual built upon multiple measured angles provides an increasingly accurate correction to the estimated error states resulting in a more accurate track of the true trajectory by the estimated trajectory.

From Figures 4.15-4.22, a pattern can be seen in the increase in accuracy as the amount of lunar features increases. For the single feature in Figure 4.15, it can be viewed as the green x along the lower portion of the red sphere facing the ECEF Y-axis. In Figure 4.16a, the north position state error variance at 1 feature is ±273.9m and the east position state error variance is ±114m. The error variance significantly decreases to ±7.435m for the north position state error variance, and the east position state error variance decreases to ±1.326m as shown in Figure 4.22a. The decrease in the error variance for the position states confirms the previous prediction that the increase in features improves the EKF error estimate. The trajectory track in Figure 4.22b shows what appears to be a loose track of the true trajectory when compared to the trajectory estimation with less features in Figure 4.18b. However, the associated position state error plots in Figure 4.22a for 1000 features confirms the substantial decrease in position state error with the increase to 1000 features. The drift in Figure 4.22b can then be attributed to only the down position state which is observed by a barometer which provides the same down position error correction for all of the feature quantity testing scenarios.

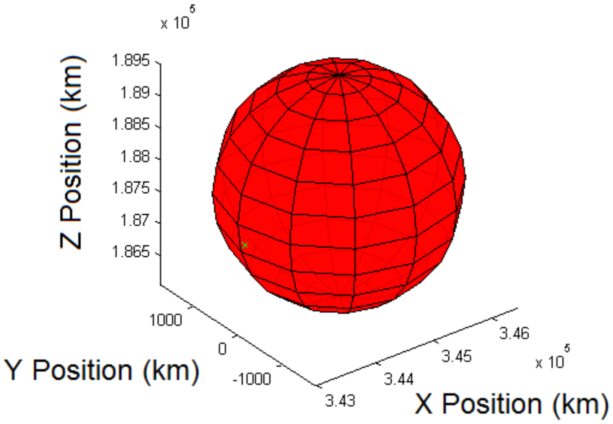

Figure 4.15. ECEF Frame. Moon and 1 Random Feature.

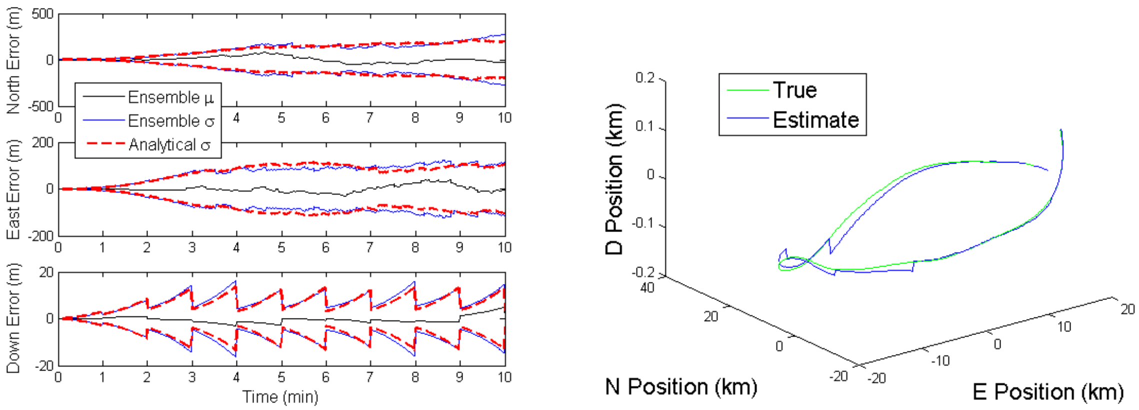

(a) Position State Error for the n-frame North, East, Down axes respectively

(b) Estimated vs. True Trajectory

Figure 4.16. Feature Quantity: 1.

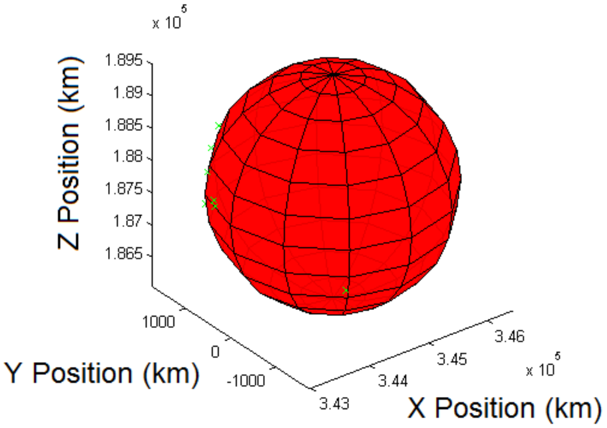

Figure 4.17. ECEF Frame: Moon and 10 Random Features.

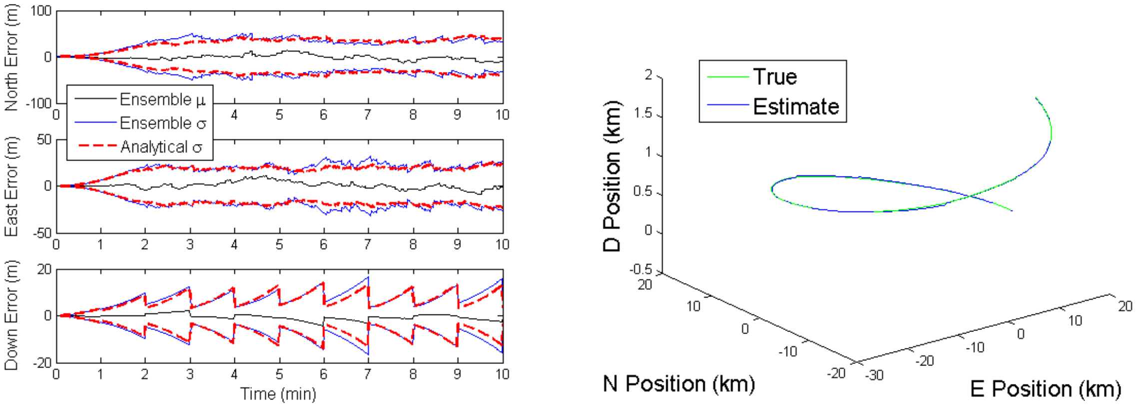

(a) Position State Error for the n-frame North, East, Down axes respectively

(b) Estimated vs. True Trajectory

Figure 4.18. Feature Quantity: 10.

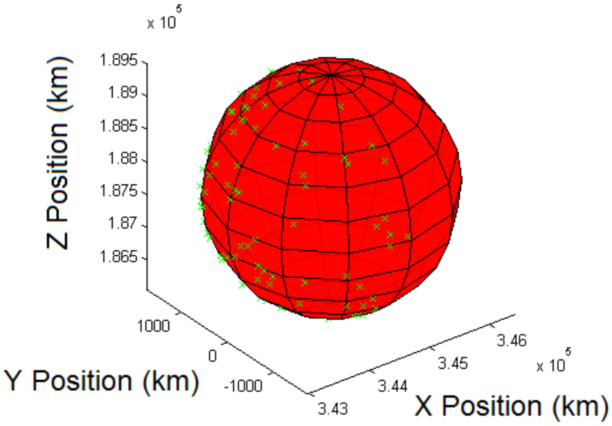

Figure 4.19. ECEF Frame. Moon and 100 Random Features.

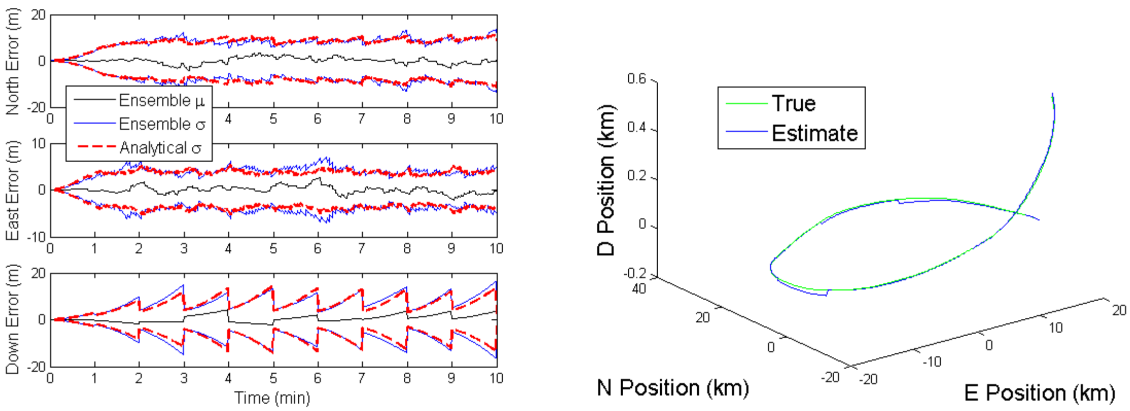

(a) Position State Error for the n-frame North, East, Down axes respectively

(b) Estimated vs. True Trajectory

Figure 4.20. Feature Quantity: 100.

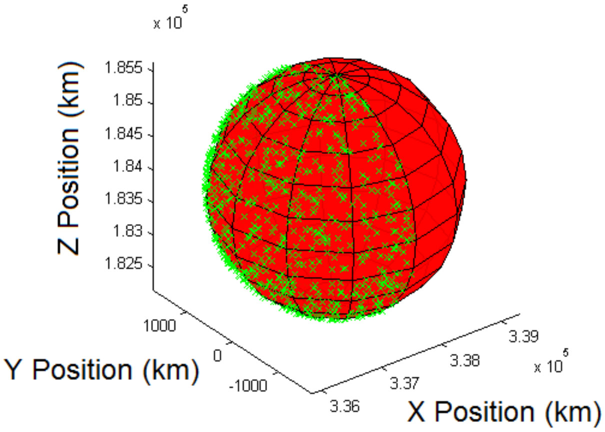

Figure 4.21. ECEF Frame. Moon and 1000 Random Features.

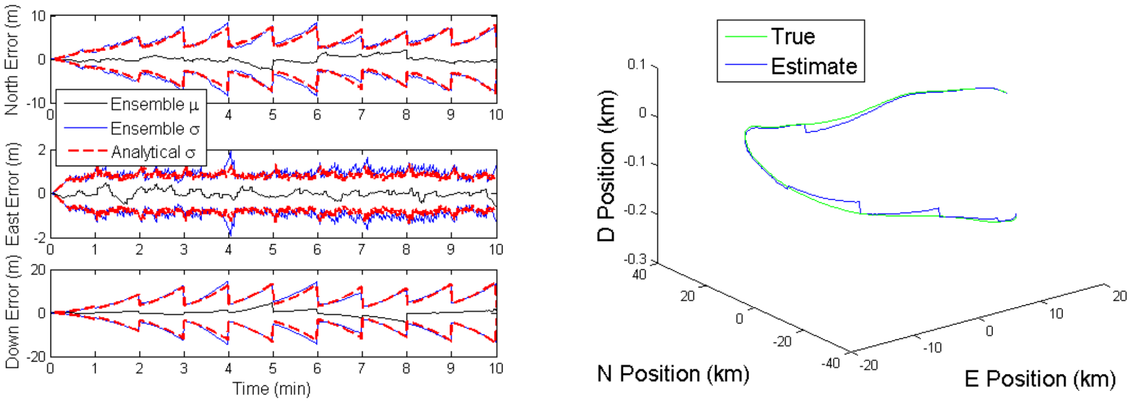

(a) Position State Error for the n-frame North, East, Down axes respectively

(b) Estimated vs. True Trajectory

Figure 4.22. Feature Quantity: 1000.

4.5 Feature Distance and Geometry Testing

The following set of scenarios that were conducted are in reference to performing INS drift correction aided by lunar features placed at various distances and lunar geometries to show the effect upon the n-frame position state estimates. All trajectory runs are based on parameters established in Table 4.1.

Feature Distance Testing.

In this research effort, an EKF incorporates lunar feature angle measurements as a correction to INS errors. As discussed in Section 3.8, feature distances can effect the amount of information the measurements provide about the states to the EKF for error state correction. This is due to the fact that Jacobians based on change in angle with respect to traveled distances are used to provide linear observability of the position states. Measured angles of a feature at infinity within the same reference frame all converge to 90°. The differences between the measured angles of a feature at infinity become indiscernible. The resulting calculated Jacobians converge to zero providing no observability of the position states in the measurement matrix $\mathbf{H}_{\text{opt},k}$ and no error state correction. Feature distances and orientation causing unobservability of each position state distinctly can occur as well when features are placed straight along an n-frame axis at a great distance. For features located at a far distance along an n-frame axis, no change in angle occurs with respect to the distance traveled along the said axis resulting in a lack of observability and correction along the particular position state.

The following scenarios seek to show that though features at infinity cause unobservability, the features located at the Moon's distance still provide usable Jacobian values. Also, the effect of feature distances located along an n-frame axis causing unobservability for the associated position state distinctly will be shown. For the following simulations, the Sun's distance is considered infinity for simulation. The ECEF frame axes are denoted by X ,Y, Z and the fixed local level n-frame axes are N, E, D as discussed in Section 2.3.

n-frame N-axis Distance Testing.

Figures 4.24-4.29 show the results of INS drift correction aided by lunar features placed along the north axis as shown in Figure 4.23. The orientation of the features in Figure 4.23 in no way represents the orientation of the Moon's orbit around the Earth. The orientation of the features along the ECEF Z-axis is set up to provide insight into INS drift correction behavior aided by lunar features located along the N-axis of the n-frame. Figure 4.24a confirms the assertion that the features directly along a single axis will cause a decrease in observability of the position state along that axis. The position state error variance in Figure 4.24a shows a much higher error variance for the north position state than the east position state. This is due to the lack of angular changes of the aircraft's north position with respect to the features along the N-axis which causes a low observability of the north position state by the Jacobian. The pattern is repeated in Figure 4.25a for the features being moved along the positive ECEF Z-axis to the Sun's distance. Also, at this distance, the north position state error variance grows to the form of the uncorrected drift error variance for the north position state error simulated in Section 3.5 for a Tactical Grade INS. The east position state error also begins to diverge back to the original uncorrected drift shown in Section 3.5 for a Tactical Grade INS as well.

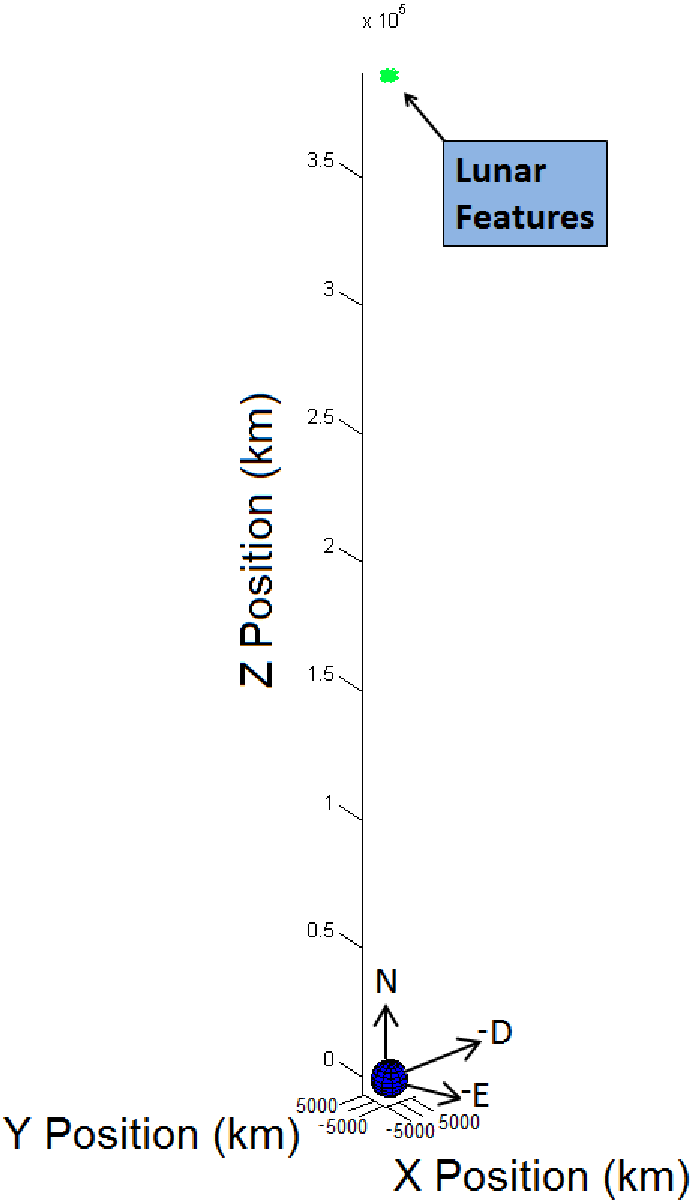

Figure 4.23. ECEF Frame. Features along n-frame N-axis and ECEF Z-axis (Not to Scale).

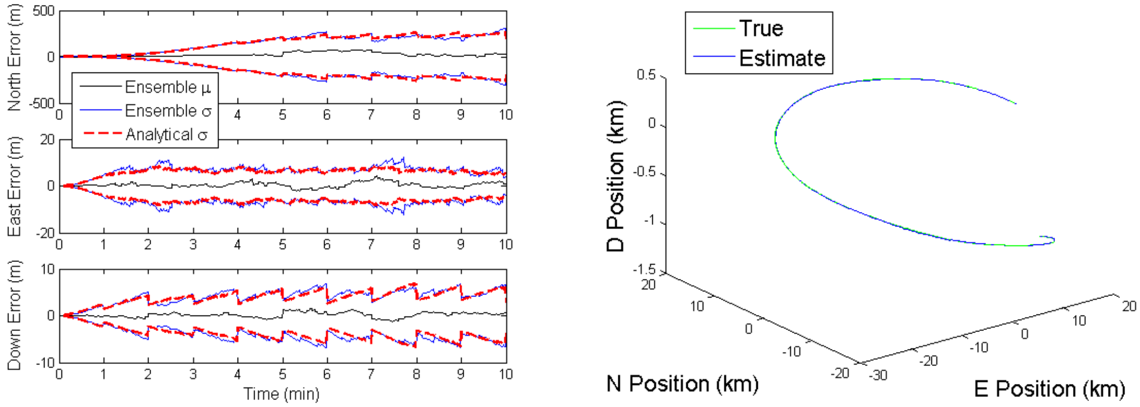

(a) Position State Error for the n-frame North, East, Down axes respectively

(b) Estimated vs. True Trajectory

Figure 4.24. Features Moon Distance along N-axis and ECEF Z-axis.

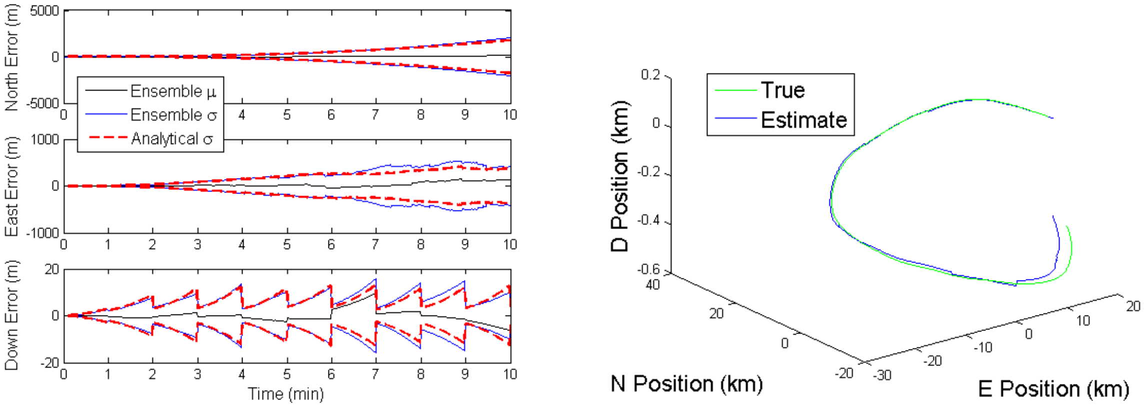

(a) Position State Error for the n-frame North, East, Down axes respectively

(b) Estimated vs. True Trajectory

Figure 4.25. Features at Sun Distance along N-axis and ECEF Z-axis.

The ensemble statistics for the azimuth angle Jacobians in Figures 4.26-4.27 also show the decrease in observability by order of magnitude for the north position error state with the increase in distance along the N-axis. For the elevation angle Jacobian ensemble statistics in Figures 4.28-4.29, all three position error states loose observability by an order of magnitude with the change in distance to the Sun's distance.

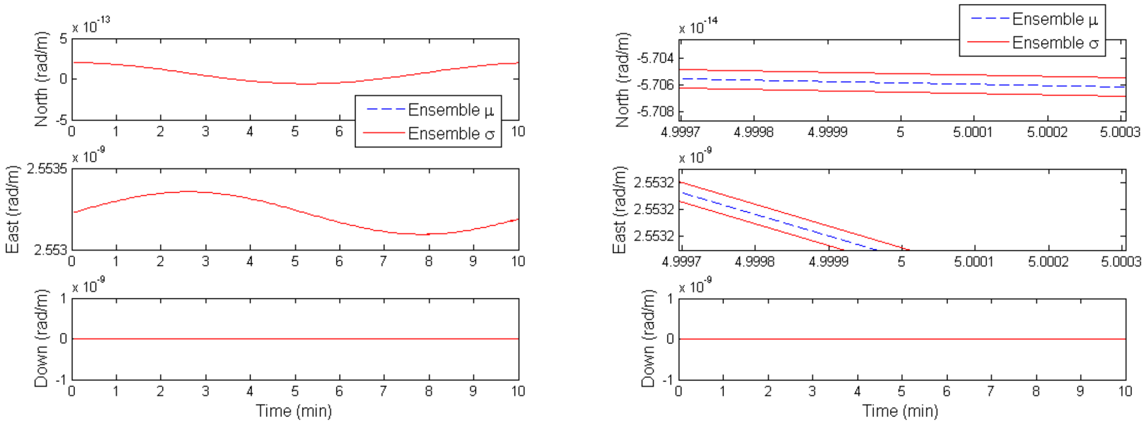

(a) Azimuth Angle Jacobians for the n-frame North, East, Down axes respectively

(b) Scaled View of Figure 4.26a

Figure 4.26. Features at Moon Distance along N-axis and ECEF Z-axis.

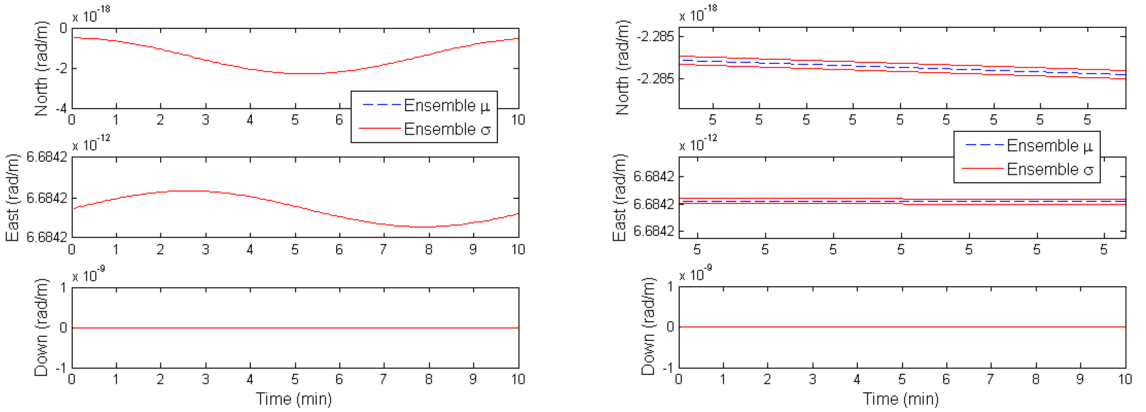

(a) Azimuth Angle Jacobians for the n-frame North, East, Down axes respectively

(b) Scaled View of Figure 4.27a

Figure 4.27. Features at Sun Distance along N-axis and ECEF Z-axis.

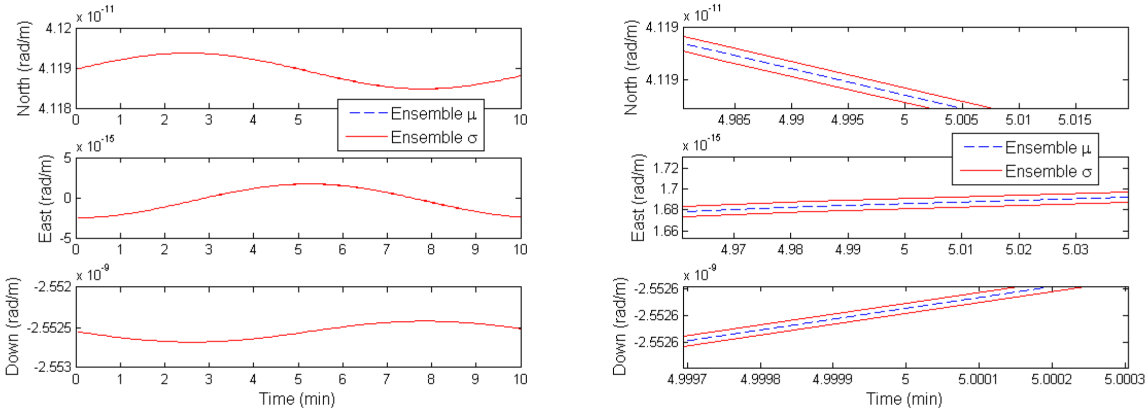

(a) Elevation Angle Jacobians for the n-frame North, East, Down axes respectively

(b) Scaled View of Figure 4.28a

Figure 4.28. Features at Moon Distance along N-axis and ECEF Z-axis.

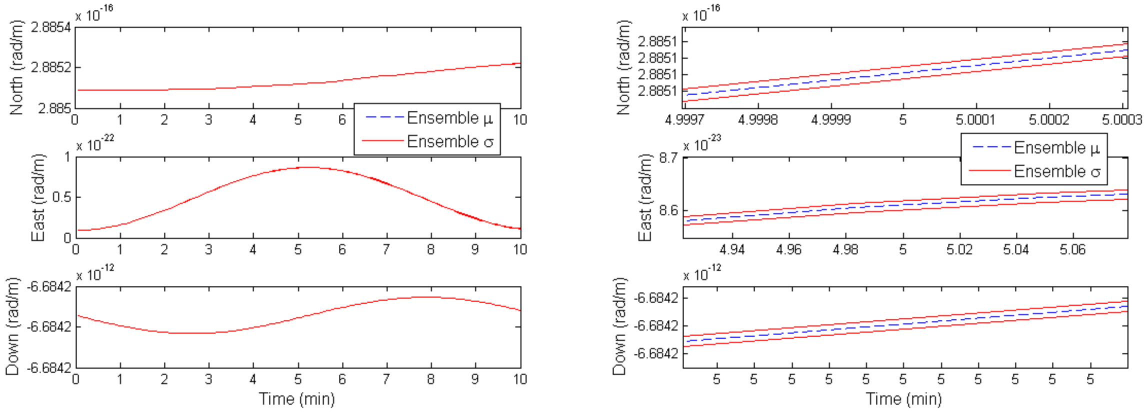

(a) Elevation Angle Jacobians for the n-frame North, East, Down axes respectively

(b) Scaled View of Figure 4.29a

Figure 4.29. Features at Sun Distance along N-axis and ECEF Z-axis.

n-frame E-axis Distance Testing.

For the next two scenarios features were placed along the n-frame E-axis at the Moon's distance for the first scenario and then at the Sun's distance for the second scenario to observe the INS drift correction with lunar features directly along the east axis. Figure 4.30 shows the orientation of the features with respect to the n-frame E-axis which coincides with the ECEF Y-axis for this set of scenarios.

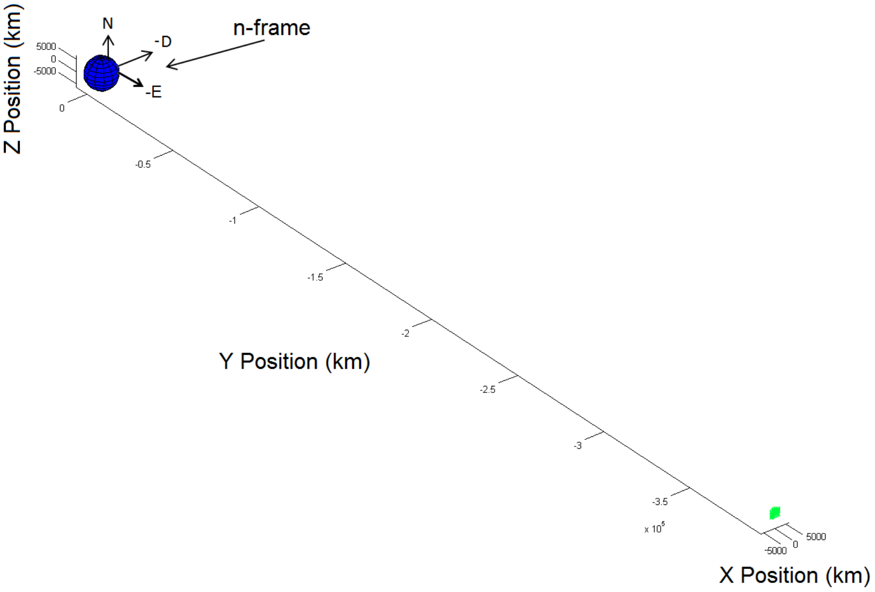

Figure 4.30. ECEF Frame. Features along n-frame E-axis and ECEF Y-axis (Not to Scale).

Figures 4.31a and 4.32a confirm the claim that the correction to INS errors by lunar feature angular measurements will decrease at great distances. Both position state error variances in Figure 4.32a are near the simulated uncorrected Tactical Grade INS position state error variance presented in Section 3.5. Figure 4.31a also confirms the relationship of the lack of position state observability with features at the lunar distance along the E-axis causing a larger variance for the the east position state error with an approximately 240m greater error variance compared to the north position state error variance. The azimuth angle Jacobian ensemble statistics in Figures 4.33 and 4.34 confirm a decrease in observability at the greater distance of the features along the E-axis with the drop in observability by an order of magnitude for the east position state Jacobian. The elevation Jacobians in Figures 4.35-4.36 also show an decrease by an order of magnitude for the three position state errors.

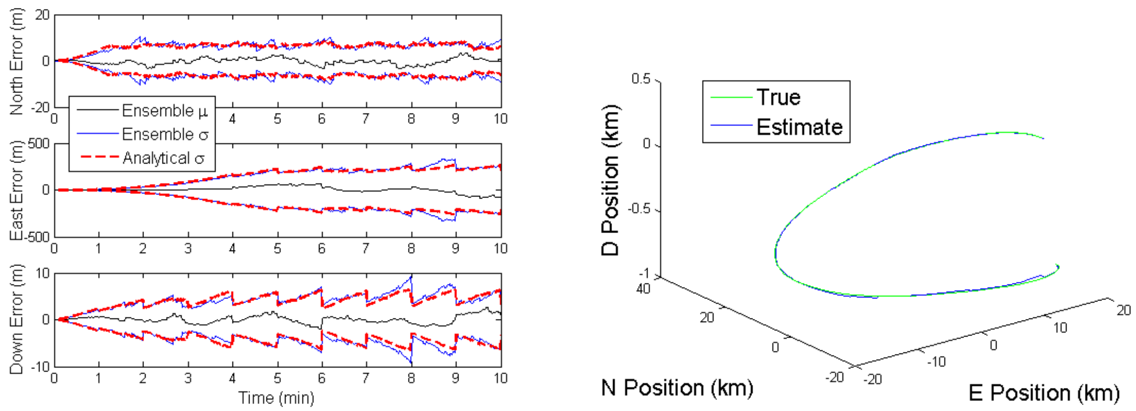

(a) Position State Errors for the n-frame North, East, Down axes respectively

(b) Estimated vs. True Trajectory

Figure 4.31. Features at Moon Distance along E-axis and ECEF Y-axis.

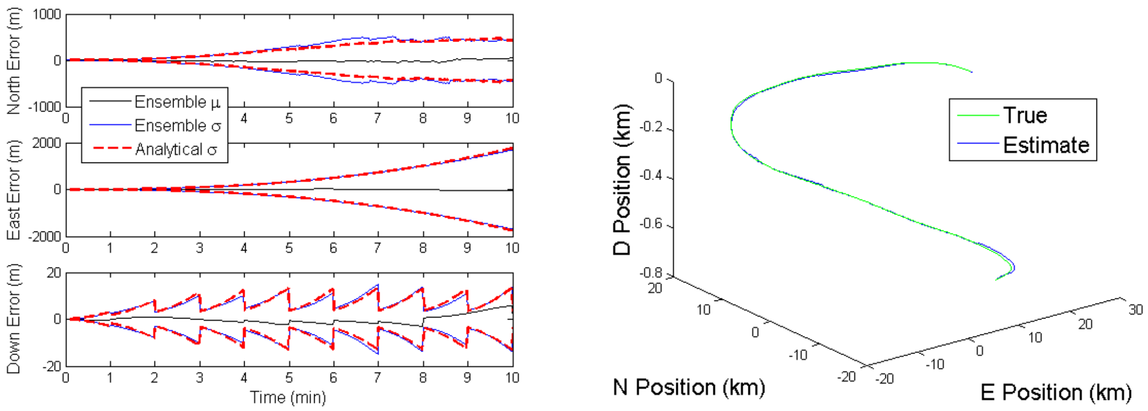

(a) Position State Errors for the n-frame North, East, Down axes respectively

(b) Estimated vs. True Trajectory

Figure 4.32. Features at Sun Distance along E-axis and ECEF Y-axis.

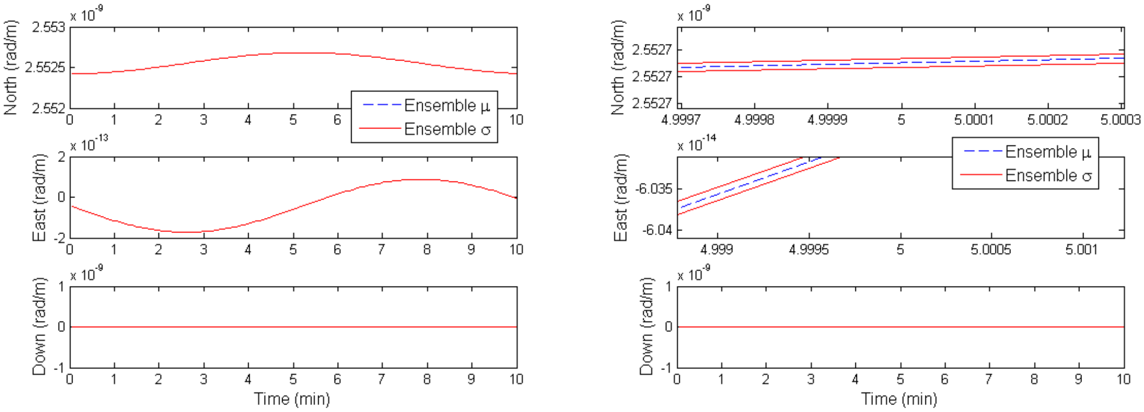

(a) Azimuth Angle Jacobians for the n-frame North, East, Down axes respectively

(b) Scaled View of Figure 4.33a

Figure 4.33. Features at Moon Distance along E-axis and ECEF Y-axis.

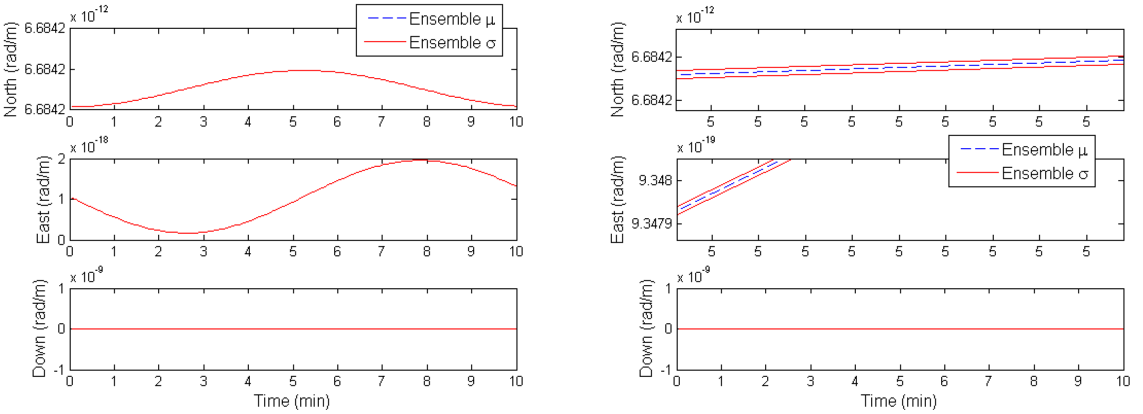

(a) Azimuth Angle Jacobians for the n-frame North, East, Down axes respectively

(b) Scaled View of Figure 4.34a

Figure 4.34. Features at Sun Distance along E-axis and ECEF Y-axis.

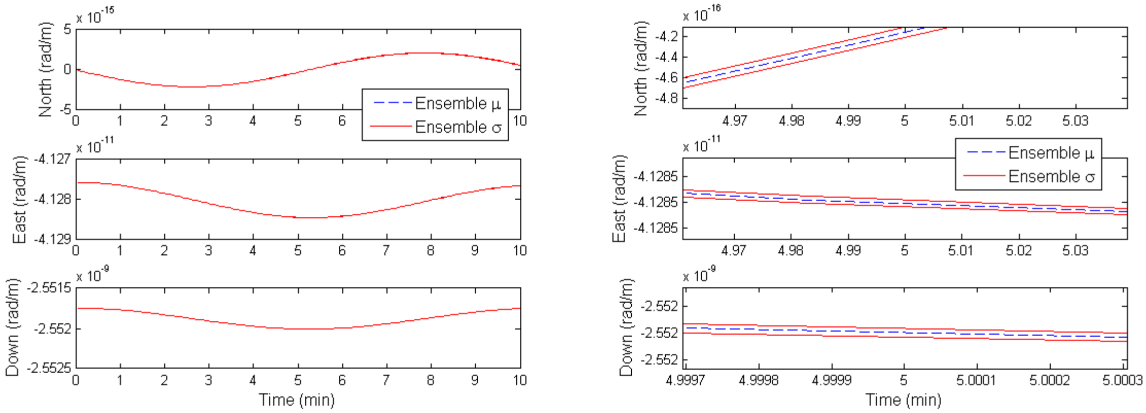

(a) Elevation Angle Jacobians for the n-frame North, East, Down axes respectively

(b) Scaled View of Figure 4.35a

Figure 4.35. Features at Moon Distance along E-axis and ECEF Y-axis.

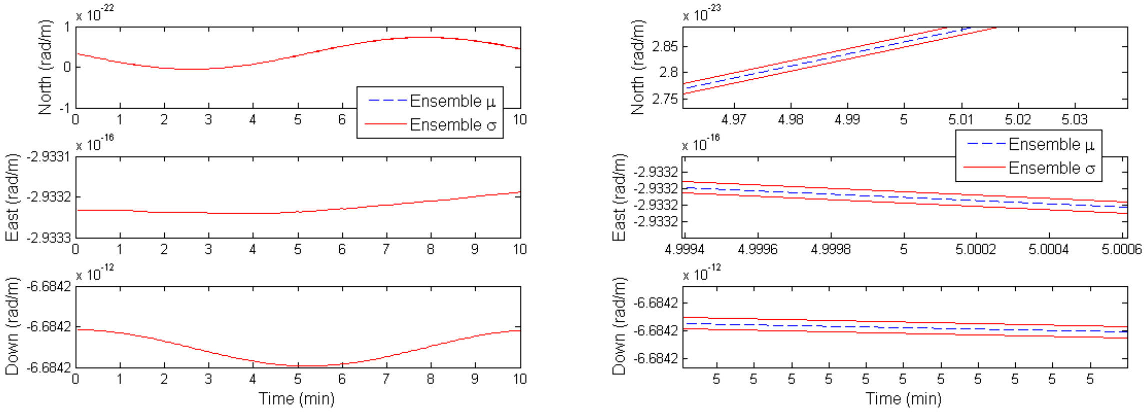

(a) Elevation Angle Jacobians for the n-frame North, East, Down axes respectively

(b) Scaled View of Figure 4.36a

Figure 4.36. Features at Sun Distance along E-axis and ECEF Y-axis.

n-frame D-axis Distance Testing.

For this set of scenarios, lunar features were placed along the D-axis at great distances to observe the INS error correction under such circumstances. The location of the lunar features along the ECEF X-axis for this set of scenarios coincides directly with the n-frame D-axis as the initial location of the aircraft's trajectory is located at 0°lat 0°lon and stays within a small range over its course as shown in Figure 4.37. This feature orientation with respect to the aircraft provides for a special case in position state observabilities provided by the Jacobians due to the nature of the spherical coordinate system angles. The azimuth angle Jacobians are solely calculated for the north and east position states with observabilities along the planar surface of the E-N plane independent of the down position state observability. The E-N plane is perpendicular to the D-axis, essentially, still holding Jacobians with observability of the north and east position states independent of the feature distances along the D-axis. The elevation angle Jacobians are, however, tied to the position of the features along the D-axis based upon the nature of the elevation angle holding observabilties along all three position states.

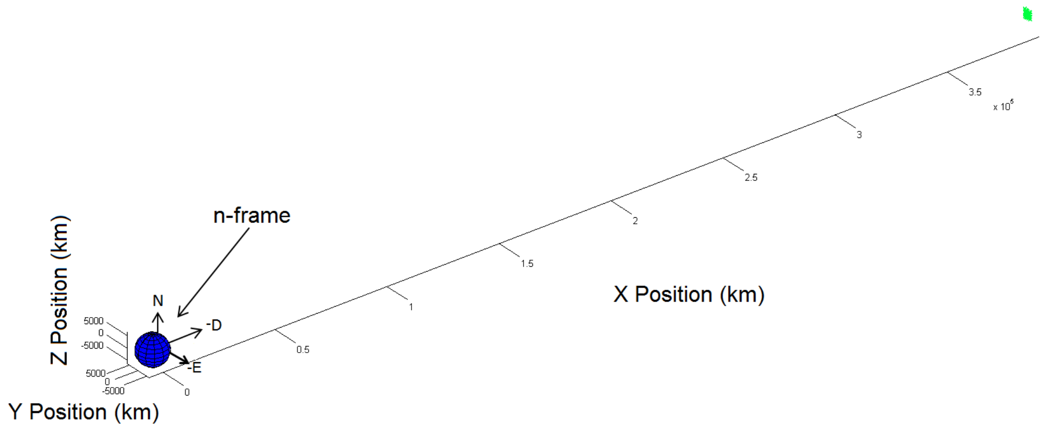

Figure 4.37. ECEF Frame. Features along n-frame D-axis and ECEF X-axis (Not to Scale).

Figures 4.38a and 4.39a present the results of the INS drift correction based upon lunar features directly above the n-frame along the D-axis coinciding with the ECEF X-axis. Both sets of error variance for the north and east position states stay within ±0.35m when the features are moved from the lunar distance above n-frame to the Sun's distance. The behavior is reiterated in the ensemble statistics of the Jacobians.

The north and east position state's azimuth angle Jacobians with features at lunar and solar distances in Figures 4.40 and 4.41 respectively do not show a dramatic change in observability with the change in distance along the D-axis. On the other hand, the position state observabilities from the elevation angle Jacobians in Figures 4.42 and 4.43 do show a greater decrease by an order of magnitude for the all three position states, but the most dramatic decrease is seen in the change for the observability of the down position state by the elevation angle Jacobian.

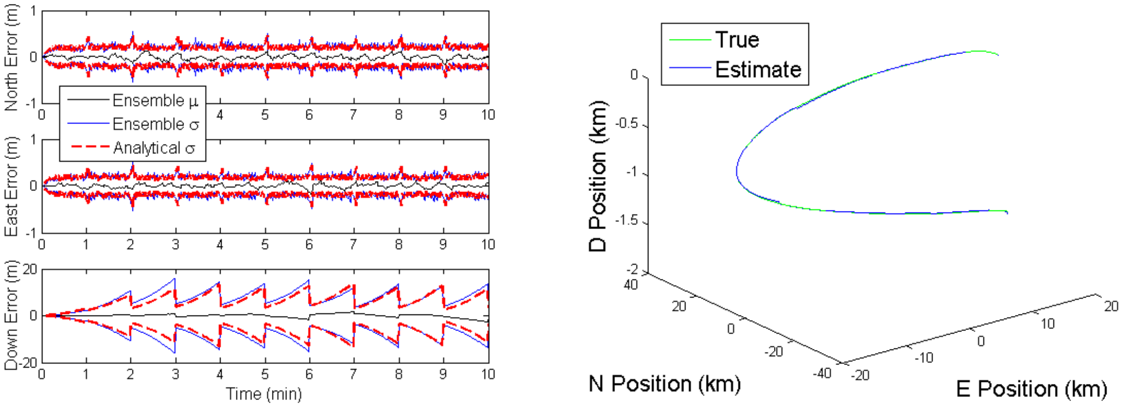

(a) Position State Errors for the n-frame North, East, Down axes respectively

(b) Estimated vs. True Trajectory

Figure 4.38. Features at Moon Distance along D-axis and ECEF X-axis.

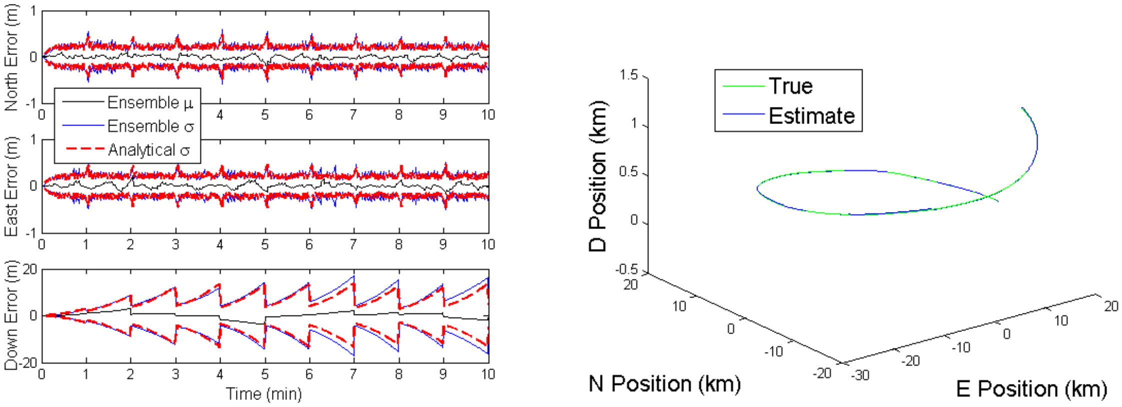

(a) Position State Errors for the n-frame North, East, Down axes respectively

(b) Estimated vs. True Trajectory

Figure 4.39. Features at Sun Distance along D-axis and ECEF X-axis.

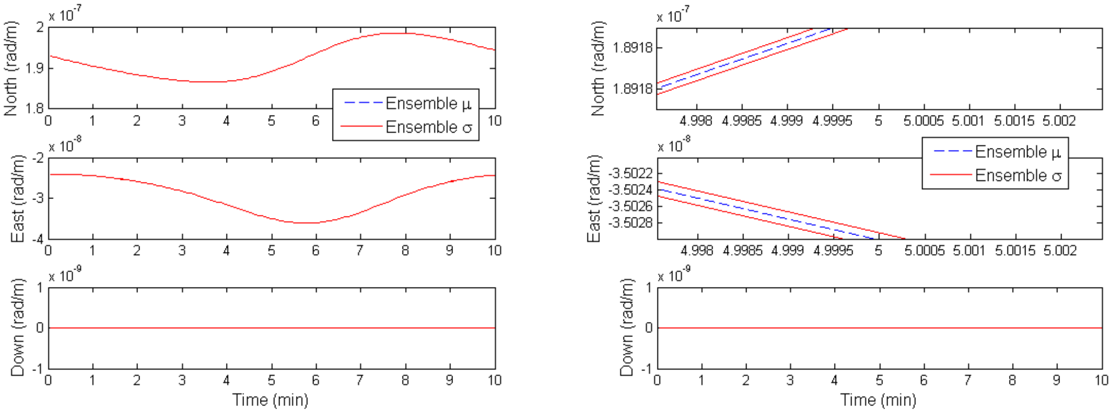

(a) Azimuth Angle Jacobians for the n-frame North, East, Down axes respectively

(b) Scaled View of Figure 4.40a

Figure 4.40. Features at Moon Distance along D-axis and ECEF X-axis.

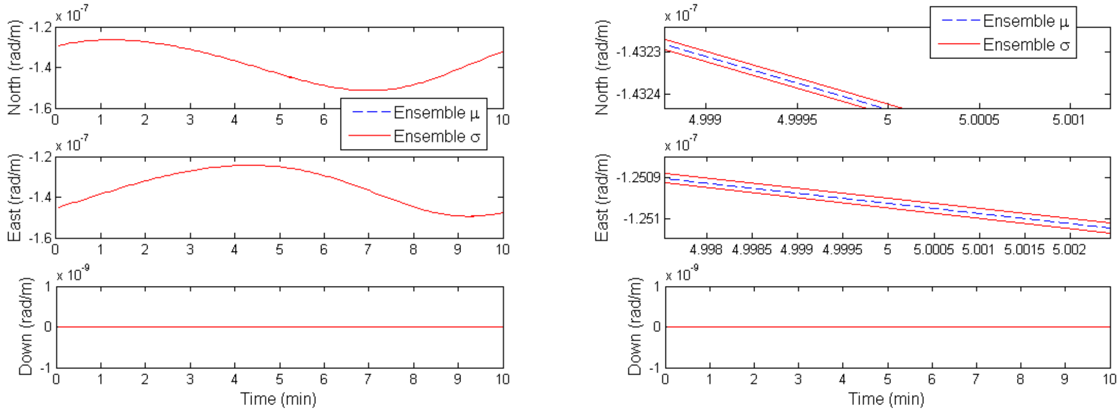

(a) Azimuth Angle Jacobians for the n-frame North, East, Down axes respectively

(b) Scaled View of Figure 4.41a

Figure 4.41. Features at Sun Distance along D-axis and ECEF X-axis.

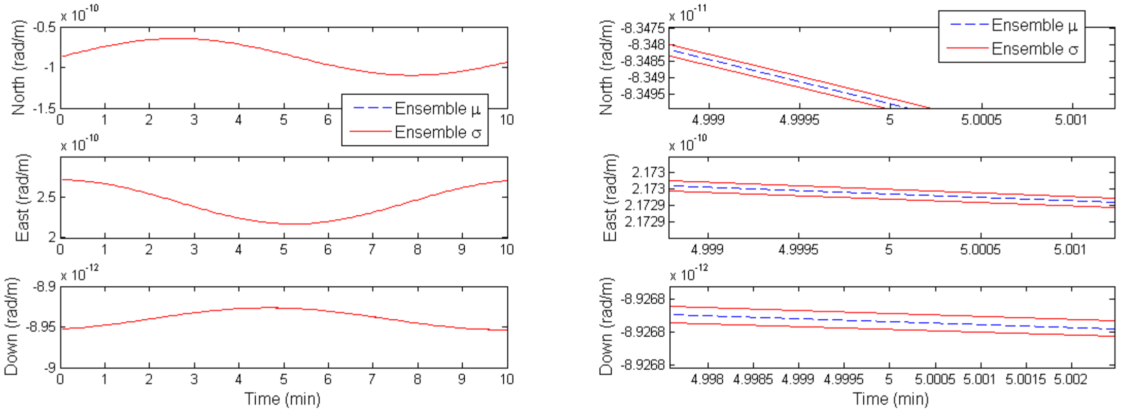

(a) Elevation Angle Jacobians for the n-frame North, East, Down axes respectively

(b) Scaled View of Figure 4.42a

Figure 4.42. Features at Moon Distance along D-axis and ECEF X-axis.

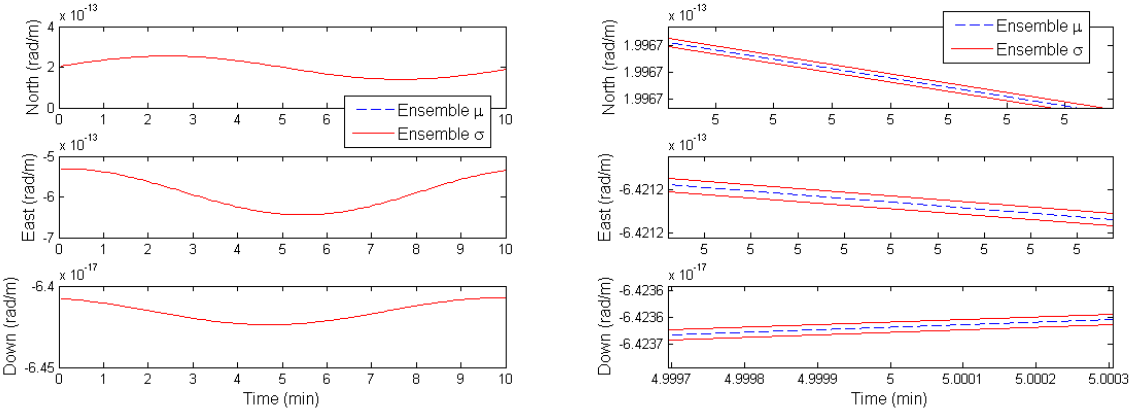

(a) Elevation Angle Jacobians for the n-frame North, East, Down axes respectively

(b) Scaled View of Figure 4.43a

Figure 4.43. Features at Sun Distance along D-axis and ECEF X-axis.

Lunar Orbital Geometry Testing.

The following set of scenarios presents the results of performing INS drift correction aided by lunar feature angle measurements under different lunar geometries obtained from lunar orbit characteristics detailed in Table 2.1. The previous section showed that features located at great distances along an n-frame axis will cause minimal INS drift correction for the associated position state error. With this in mind, the error state estimation and correction performance of the EKF under different lunar orientations can be predicted. As mentioned in Section 2.6, the two main categories of lunar celestial geometry that will be looked at are:

1. Lunar feature location at inclination with respect to the Earth's equator plane.
2. Lunar feature location along the lunar orbit path with respect to the Earth's center and Prime Meridian.

Inclination to Equator.

Different lunar inclinations to the equator are shown in Figure 4.44 providing the frame for the following scenarios:

1. Lunar features at the highest inclination to equator.
2. Lunar features above the equator and at the zenith of the trajectory.
3. Lunar features at the lowest inclination to equator.

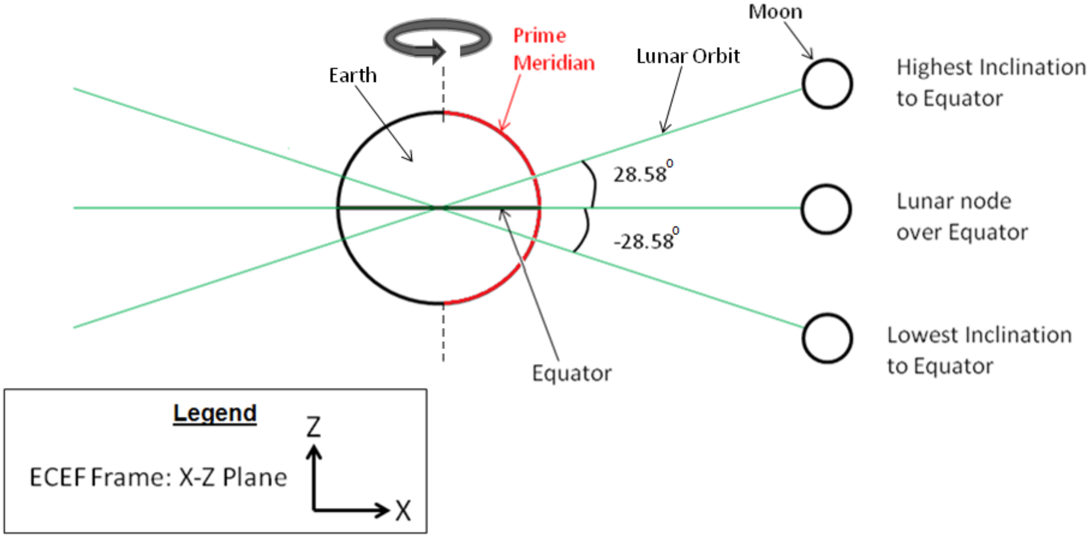

Figure 4.44. Lunar Inclinations to Equator.

For the lunar features at the highest inclination to the equator, Figures 4.45-4.47 show the orientation of the simulated lunar features with respect to the ECEF frame and the n-frame. Figure 4.48a shows a greater error variance in the north position state at ±12.13m along with lower variance for the east position state error at ±3.981m.

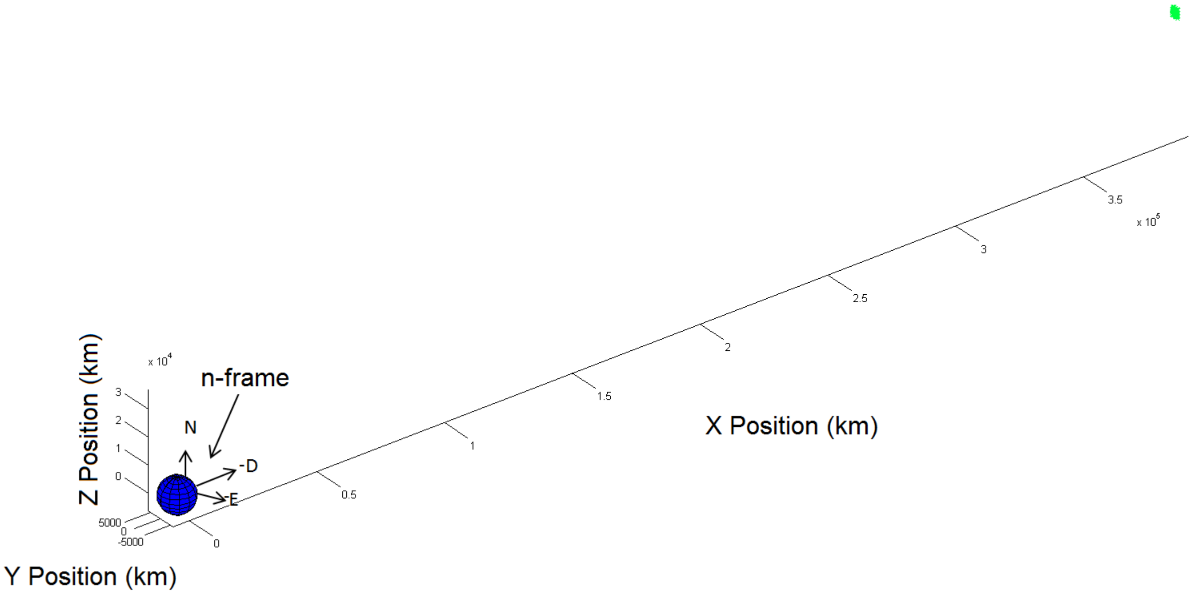

Figure 4.45. ECEF Frame. Highest Lunar Inclination to Equator (Not to Scale).

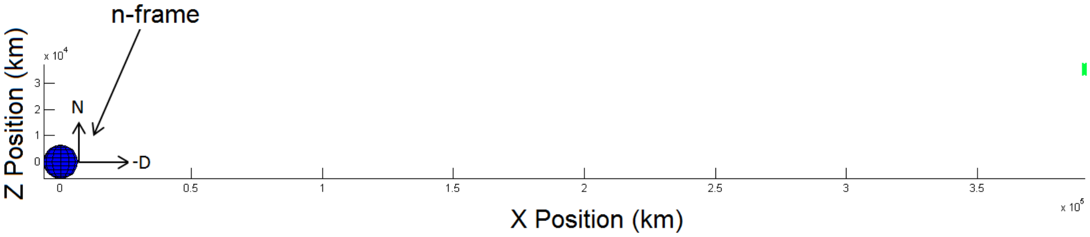

Figure 4.46. ECEF Frame: X-Z Plane. Highest Lunar Inclination to Equator (Not to Scale).

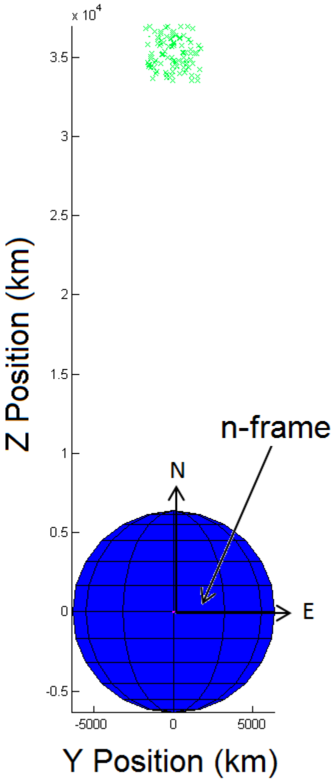

Figure 4.47. ECEF Frame: Y-Z Plane. Highest Lunar Inclination to Equator (Not to Scale).

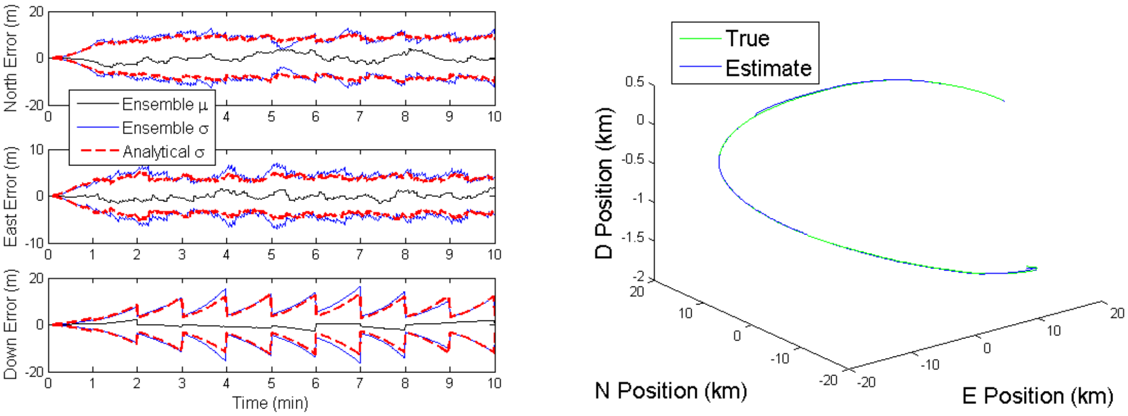

(a) Position State Error for the n-frame North, East, Down axes respectively

(b) Estimated vs. True Trajectory

Figure 4.48. Features at Highest Lunar Inclination to Equator.

Figures 4.49 and 4.50 present the scenario where lunar features are located straight above the equator and the trajectory zenith. The position state errors are shown in Figure 4.51a. Both the east and north position error states are within ±0.33m. The geometry of the angles straight above the trajectory provide for excellent observability of the north and east position states which lie along the N-E plane with the features lying directly along the D-axis above. This follows the special case of the spherical coordinate system angle calculations mentioned in the previous n-frame D-axis distance testing subsection.

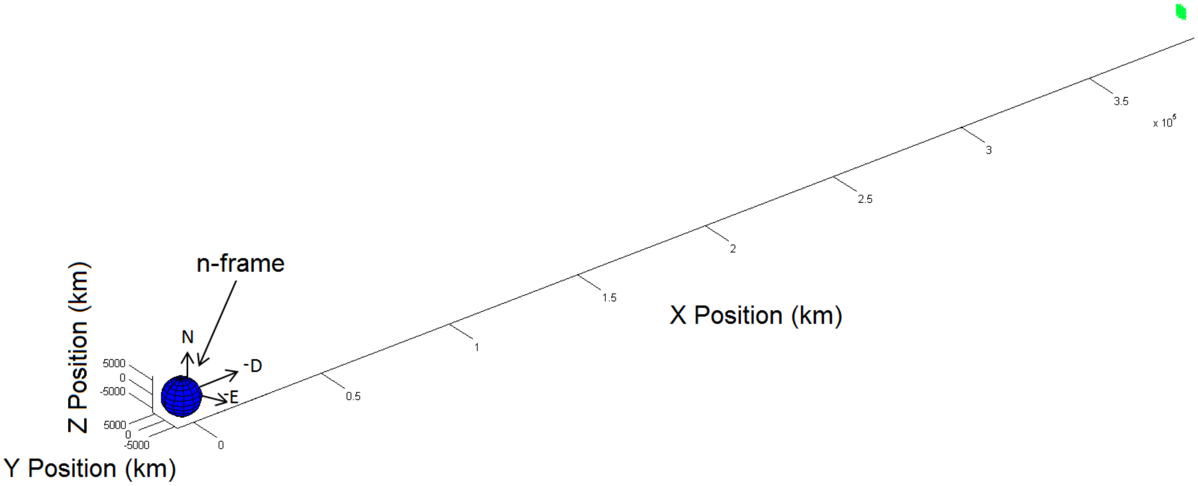

Figure 4.49. ECEF Frame: Inclination to Equator at 0° (Not to Scale).

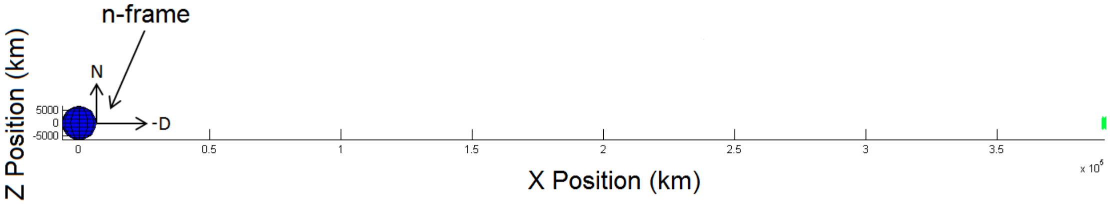

Figure 4.50. ECEF Frame: X-Z Plane. Inclination to Equator at 0° (Not to Scale).

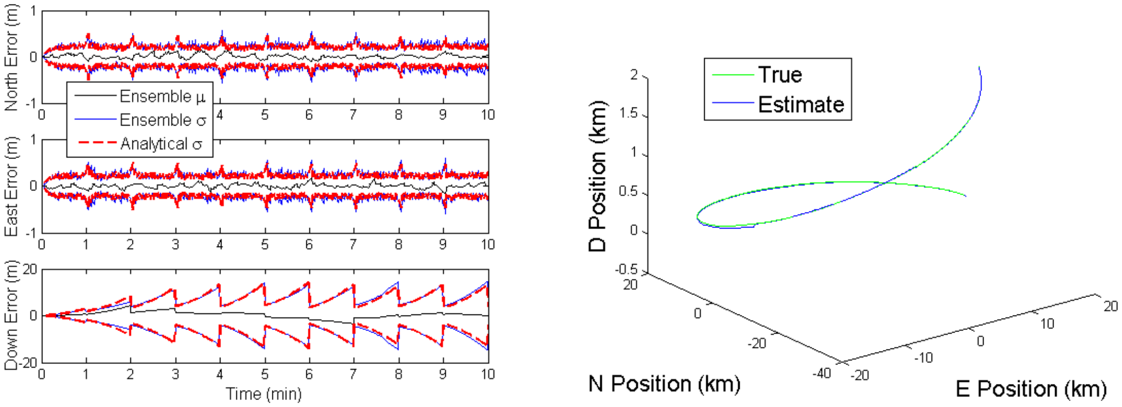

(a) Position State Error for the n-frame North, East, Down axes respectively

(b) Estimated vs. True Trajectory

Figure 4.51. Features above Equator and at Trajectory Zenith.

The next scenario involves the behavior of the position state estimates aided by lunar feature measurements located at the lowest inclination to the equator represented by Figure 4.52. The results can be seen in Figures 4.53a. It is interesting to note that the north and east position state error variance for lunar features at the highest inclination to the equator in Figure 4.48a follows a similar error variance pattern for the position state errors for the lunar features at the lowest inclination to the equator. This can be explained by both scenario sets having features located at $+28.58°$ or $-28.58°$along the same plane used in both scenarios allowing for similar Jacobians to be calculated for the position states.

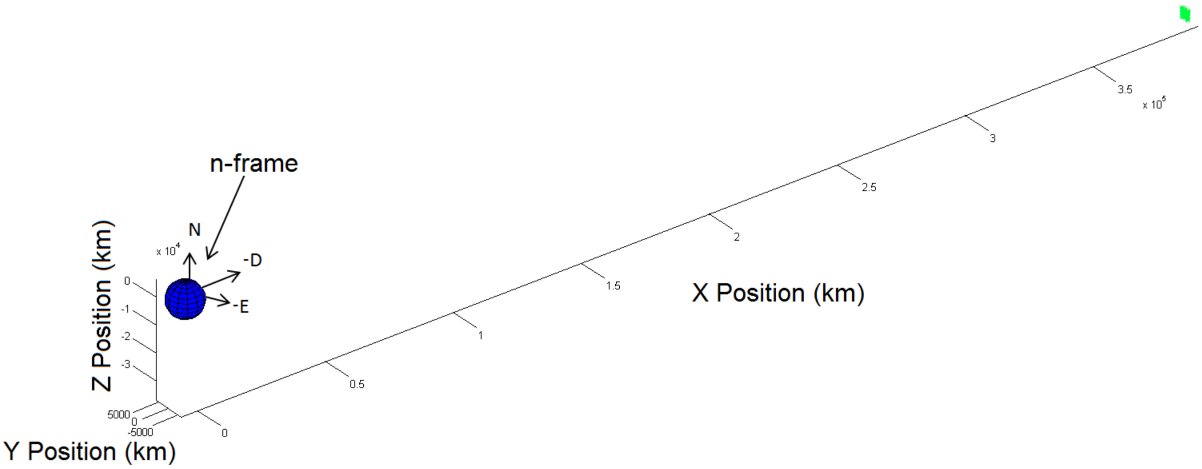

Figure 4.52. ECEF Frame: Lowest Inclination to Equator (Not to Scale).

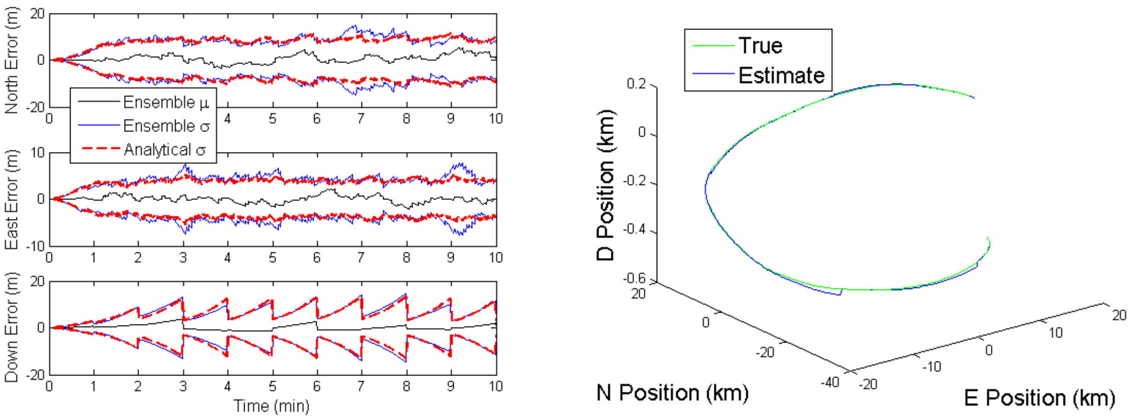

(a) Position State Error for the n-frame North, East, Down axes respectively

(b) Estimated vs. True Trajectory

Figure 4.53. Features at Lowest Lunar Inclination to Equator.

Lunar Feature Position Along the Orbit with respect to the Prime Meridian.

The following scenarios are constructed to understand the behavior of the INS drift correction aided by lunar features that are located at positions along the lunar orbit with respect to the Earth's center and Prime Meridian as represented in Figure 4.54. The first scenario is represented in Figure 4.55 where the location of the trajectory is at 0°lat 0°lon and the lunar features lie along the Moon's orbit at 90°W of the Prime Meridian still maintaining the default high inclination to the equator discussed in Section 4.1. Based upon the behavior of the EKF and the measured angles, the estimated east position state will have a higher error variance than the north position state from what was discovered in the feature distance testing with regards to angle observability of position states.

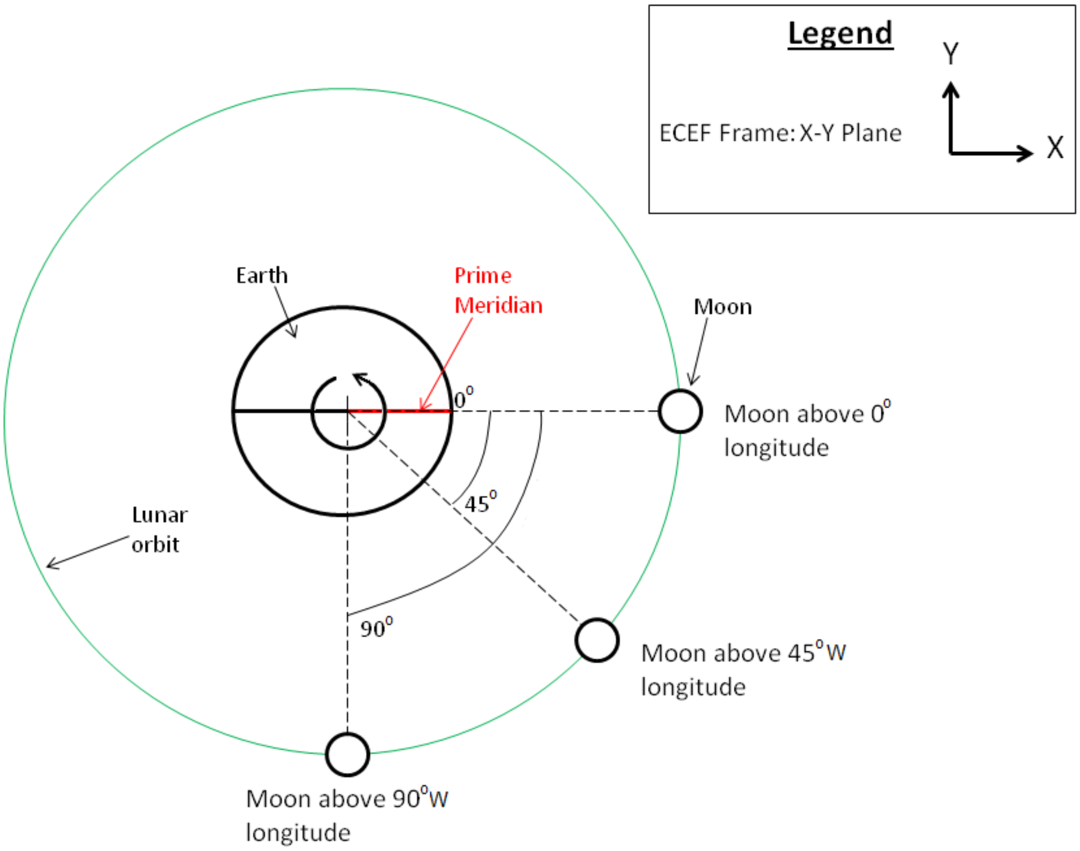

Figure 4.54. Lunar feature orientations to Earth longitude.

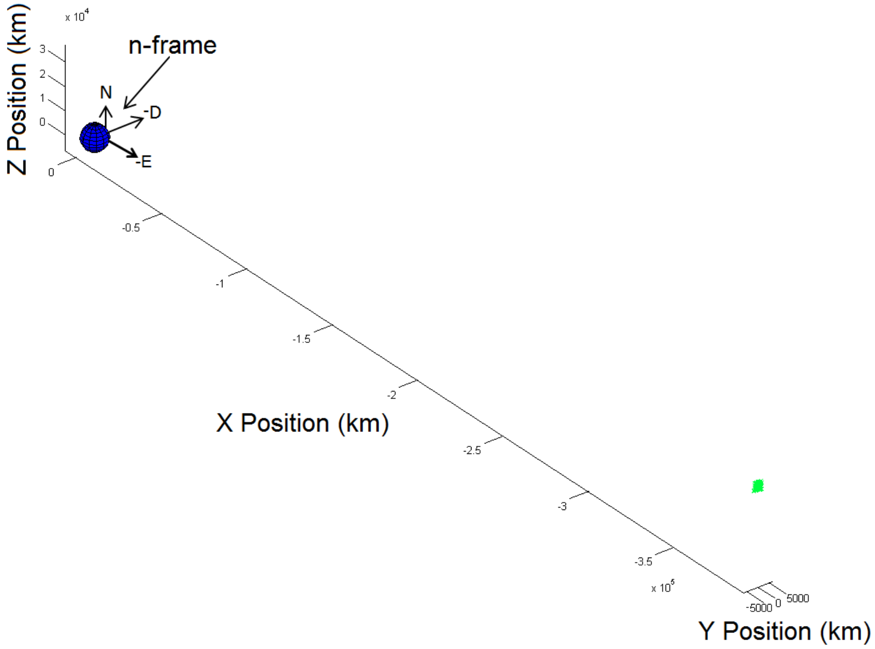

Figure 4.55. ECEF Frame: Lunar features at 90°W (Not to Scale).

The results from the scenario can be viewed in Figures 4.56a. As expected, the error variance for the east position state is much larger at ±228.2m than the north position state at ±123.7m.

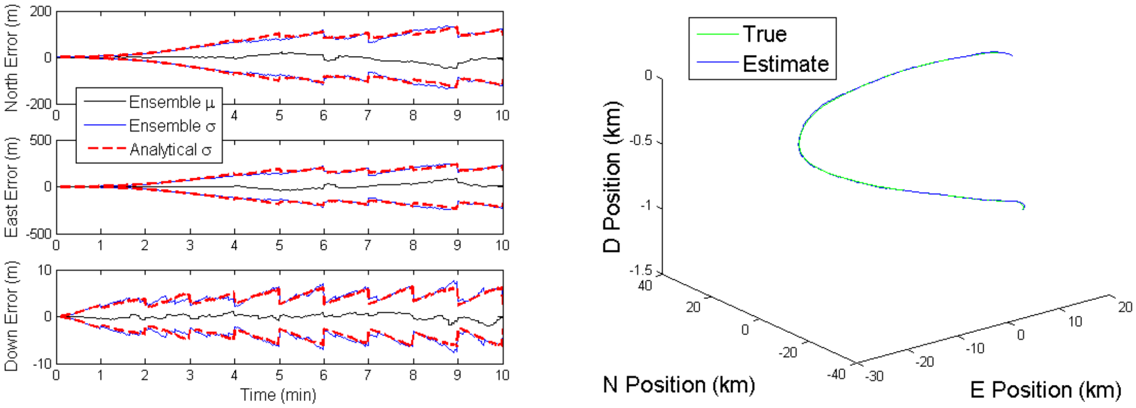

(a) Position State Error for the n-frame North, East, Down axes respectively

(b) Estimated vs. True Trajectory

Figure 4.56. Lunar features at 90°W of the Prime Meridian and Highest Inclination to Equator.

The next scenario involved the lunar features being placed along the Moon's orbit at 45°W of the Prime Meridian and at the highest inclination to the equator 28.58° as shown in Figure 4.57. The results can be viewed in Figures 4.58a. The results show a decrease in error variance for the north and east position states from the results in the previous scenario with lunar features located at 90°W. Figure 4.58a shows the north position state now has ±13.97m and the east position state has ±16.71m error variance.

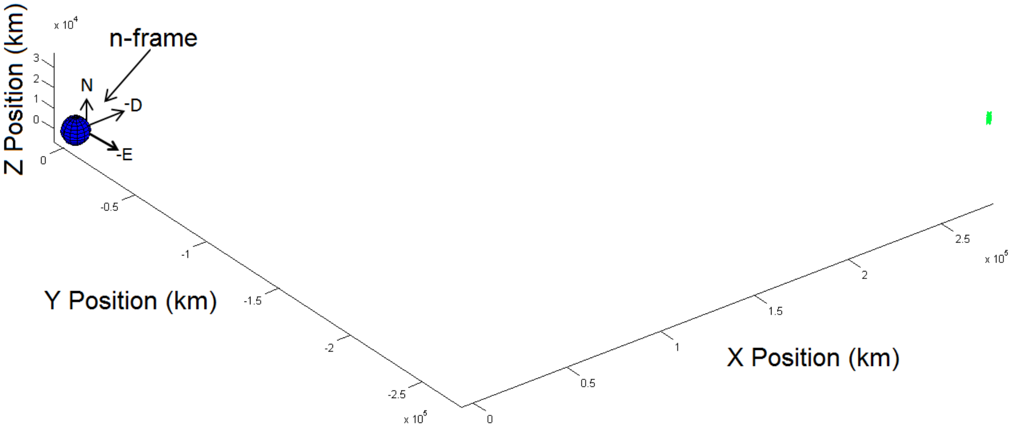

Figure 4.57. ECEF Frame: Lunar features at 45°W and Highest Inclination to Equator (Not to Scale).

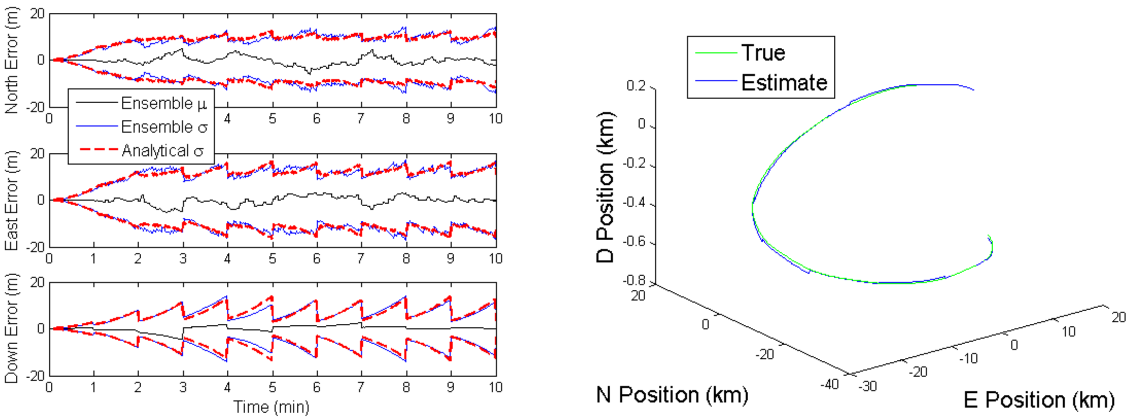

(a) Position State Error for the n-frame North, East, Down axes respectively

(b) Estimated vs. True Trajectory

Figure 4.58. Lunar features at 45°W of the Prime Meridian and Highest Inclination to Equator.

The scenario for the features above the Prime Meridian and at the highest inclination to the equator holds the same orientation for the trajectory and features represented in Figures 4.45-4.47. With the features at this location, the error variance for the north position state decreased to ±12.13m, and the east position state error variance decreased to ±3.981m as shown in Figure 4.48a.

4.6 Summary

Chapter 4 presented the results of the research methodology defined in Chapter 3. The performance of an EKF to estimate the error of an INS with the aiding of lunar features was investigated under various scenarios. Section 4.1 laid out the default trajectory parameters and the default orientation between the lunar features, aircraft trajectory, and Earth in the ECEF frame and n-frame. Section 4.2 showed the effect of aiding by lunar feature angle measurements on different INS grades. Section 4.3 tested INS drift correction aided by lunar feature angle measurements under different camera specifications. Section 4.4 looked at INS drift correction aided by lunar features of different quantities. The effects of lunar feature distance and geometry on lunar vision aided navigation with INS was explored in Section 4.5. Section 4.6 provided a summary for the chapter.

V. Conclusions

5.1 Introduction

This research effort presented the theoretical limits of a non-GPS precision navigation method consisting of an INS aided by lunar feature angle measurements where only measurement noise effects were considered. The following sections summarize the research methods and results of the scenarios from Chapters 3 and 4 respectively and conclude with suggested future work.

5.2 Conclusions

The purpose of this research effort was to establish the feasibility of a precision navigation method by which INS drift error could be corrected through the use of measured lunar feature angles. To accomplish this task, an EKF algorithm was implemented to process an INS trajectory and estimate the INS error states. Corrections to the INS error states were made during the EKF update stage with lunar feature angle measurements. Through the use of Jacobians, the lunar feature angle measurements provided position state observability based on the change in the measured lunar feature angles with respect to the change in distance along the position states. A barometer was simulated to aid the down position error state with an update rate of 60 seconds. Four total categories of scenarios were accomplished to observe the behavior of the INS drift corrections under different lunar feature conditions.

The first scenario set showed marked improvement in the navigation solution error at 1σ for an INS aided by lunar feature angle measurements compared to a stand alone INS. Also, the scenario set showed that the increase in INS grade quality led to improved position state estimation. Table 5.1 presents the position state error results for the first scenario set. The use of Commercial Grade INS in the EKF with

100 lunar feature angle measurements brought about position state error variance of ±58.96m for the north position state and ±25.85m for the east position state. When using the Navigation Grade INS, the position state error decreased significantly to ±2.946m for the north position state error variance and ±0.9805 for the east position state error variance.

Table 5.1. Feasibility Table for Lunar-Aided Navigation with respect to INS grade. Navigation Solution Error at 1σ listed in the right three columns were collected at 10min. Parameters are with respect to a trajectory traveled in a circle with a radius 20km radius with starting location at 0°lat 0°lon.

INS	Camera Noise (mrads)	Focal Length (mm)	# of features	Distance (km)	Lunar Geometry	Error Variance (m)		
						N	E	D
Commercial	0.011	253	100	384,400	Highest Inclination to Equator	58.96	25.85	77.62
Tactical						13.5	4.914	16.43
Navigation						2.946	0.9805	2.328

The second set of scenarios looked at measurement noise effects from camera specifications upon INS drift corrections by lunar feature angle measurements. A sweep of the measurement noise $\mathbf{v}_{\text{opt},k}$ based on different camera image sensor pixel sizes $\Delta\ell$ was conducted. As shown in Table 5.2, at the largest pixel size 1000μm which equated to a measurement noise of 2mrads, the error variance for the north position state was ±396m and ±216.5m for the east position state. Decreasing the pixel size to 1μm and the associated noise to 0.002mrads caused the INS error solution to improve to an error variance of ±8.33m for the north position state and ±1.54m for the east position state.

Table 5.2. Feasibility Table for Lunar-Aided Navigation with INS with respect to camera image sensor pixel size. Navigation Solution Error at 1σ listed in the right three columns were collected at 10min. Parameters are with respect to a trajectory traveled in a circle with a radius 20km radius with starting location at 0°lat 0°lon.

INS	Pixel Size (μm)	Focal Length (mm)	# of features	Distance (km)	Lunar Geometry	Error Variance (m)		
						N	E	D
Tactical	1000	253	100	384,400	Highest Inclination to Equator	396	216.5	13.18
	100					54.04	31	12.53
	10					16.97	6.473	12.68
	1					8.33	1.54	14.43

Parameters from a commercial camera were obtained to see the effects of different lens focal lengths on the measurement noise and position state error corrected by lunar feature angle measurements. Overall, the results in Table 5.3 pointed to the increase in lens focal length decreasing the position state error and increasing the performance of the EKF in estimating the true trajectory.

Table 5.3. Feasibility Table for Lunar-Aided Navigation with INS with respect to Lens Focal Length. Navigation Solution Error at 1σ listed in the right three columns were collected at 10min. Parameters are with respect to a trajectory traveled in a circle with a radius 20km radius with starting location at 0°lat 0°lon.

INS	Camera Noise (mrads)	Focal Length (mm)	# of features	Distance (km)	Lunar Geometry	Error Variance (m)		
						N	E	D
Tactical	0.055	50	100	384,400	Highest Inclination to Equator	28.67	11.25	10.55
	0.011	253				7.62	4.805	11.36
	0.003	1000				6.42	2.347	9.88

The third scenario set showed that an increase in the lunar feature quantity decreased position state error resulting in a stronger trajectory estimate. The results of the third scenario set are presented in Table 5.4. At one measured lunar feature, the error variance was at ±273.9m for the north position state and ±114m for the east position state. At 1000 features, the INS solution was corrected to an error variance of ±7.435m for the north position state and ±1.326m for the east position state.

Table 5.4. Feasibility Table for Lunar-Aided Navigation with INS with respect to Feature Quantity. Navigation Solution Error at 1σ listed in the right three columns were collected at 10min. Parameters are with respect to a trajectory traveled in a circle with a radius 20km radius with starting location at 0°lat 0°lon.

INS	Camera Noise (mrads)	Focal Length (mm)	# of features	Distance (km)	Lunar Geometry	Error Variance (m)		
						N	E	D
Tactical	0.011	253	1	384,400	Highest Inclination to Equator	273.9	114	14.56
			10			33.09	26.61	15.69
			100			13.5	4.914	16.43
			1000			7.435	1.326	13.31

The next set of scenarios encompassed the effects of feature distance and different lunar orbit geometries on INS drift correction. In Section 4.5, the feature distance scenario set showed that features at distances approaching infinity will cause a lack of observabilty of the position states resulting in an increased position state error. Also, the feature distance set of scenarios in Section 4.5 confirmed the assertion that a lack of observability will occur for a distinct position state when features lie at far distances along the respective position axis. However, for the increased feature distance along the n-frame D-axis at the trajectory's zenith, minimal effect occurred to the position state errors. Also, at this orientation, the north and east position state error variances were both shown to be extremely small ±0.35m. This was due in part to the azimuth Jacobians providing observabilities of the north and east position states independent of the down position state. The error results for the distance scenarios are not listed in a table as the feature locations are not set at realistic orbit parameters. The error results from the distance scenarios can be found in Section 4.5.

For the scenario set dealing with INS drift correction based on lunar features at different orbital geometries, features were placed at different inclinations to the equator and at different locations along the lunar orbit with the respect to the Prime Meridian. The lunar geometries are based on orbital parameters listed in Table 2.1. During the changes in feature locations at different lunar geometries, the location of the true trajectory maintained a circular path with a 20 km radius holding a starting position at 0°lat 0°lon. Table 5.5 shows the position state error results for the lunar surface features placed at different lunar inclinations with respect to the Earth's equator. The position state error for the north and east position states were shown to be minimally changed when the inclination of the feature locations at 28.58° was mirrored and the features were placed on the Moon's orbit at the lowest inclination to the equator. This is due to the similar change in angles occurring at both feature locations causing similar Jacobians which provide the observability of the states to aid in error state estimation correction.

Table 5.5. Feasibility Table for Lunar-Aided Navigation with INS with respect to lunar surface features placed at different Lunar Inclinations to Earth's equator. Navigation Solution Error at 1σ listed in the right three columns were collected at 10min. Parameters are with respect to a trajectory traveled in a circle with a radius 20km radius with starting location at 0°lat 0°lon.

INS	Camera Noise (mrads)	Focal Length (mm)	# of features	Distance (km)	Lunar Geometry	Error Variance (m)		
						N	E	D
Tactical	0.011	253	100	384,400	Highest Inclination to Equator	12.13	3.981	11.88
					At Zenith & Over Equator	0.322	0.3275	14.64
					Lowest Inclination to Equator	8.104	4.098	11.4

With features placed at different locations along the lunar orbit with respect to the Prime Meridian and maintaining the highest inclination to the equator at 28.58°, the INS error correction was shown in Table 5.6 to improve as the features approached the zenith of the trajectory. With the lunar features located at 90°W of the Prime Meridian, the north position state error variance was ±123.7m and the east position state error variance was ±228.2m. With the change of the feature locations to 45°W of the Prime Meridian, the north and east position state error variances decreased to ±13.97m and ±16.71m respectively. The decrease in error continued as the feature locations were moved to the lunar orbit position lying above the Prime Meridian with an inclination of 28.58° to the equator. The north position error state variance decreased to ±12.13m and the east position state variance decreased to ±3.981m.

Table 5.6. Feasibility Table for Lunar-Aided Navigation with INS with respect to lunar surface features placed along different lunar orbit positions and at the highest inclination to the Equator's equator. Navigation Solution Error at 1σ listed in the right three columns were collected at 10min. Parameters are with respect to a trajectory traveled in a circle with a radius 20km radius with starting location at 0°lat 0°lon.

INS	Camera Noise (mrads)	Focal Length (mm)	# of features	Distance (km)	Lunar Geometry	Error Variance (m)		
						N	E	D
Tactical	0.011	253	100	384,400	90°W of Prime Meridian	123.7	228.2	6.02
					45°W of Prime Meridian	13.97	16.71	11.37
					Over Prime Meridian	12.13	3.981	11.88

In conclusion, this research effort presented the theoretical limits of a viable non-GPS precision navigation method able to operate when GPS is unavailable. The method is based on lunar feature angle measurements aiding an INS. Although measurement noise was only considered to effect the model, the results in Chapter 4 showed that INS drift correction provided by lunar feature angle measurements can theoretically greatly improve a navigation solution compared to a stand-alone INS.

5.3 Future Work

With the conclusion of this research effort, below are areas that are worth exploring in continuing to pursue lunar vision-aided navigation:

1. Conduct INS drift correction with lunar feature angle measurements under realistic noise parameters considering error in feature extraction and matching techniques, and the error for a camera's alignment to the local navigation frame.

2. Observe the simulated INS drift correction aided by feature angles extracted from lunar feature images. Capture real world lunar images with a camera to understand the relationship between camera resolution and the observed lunar images.

3. Implement a feature detection and extraction algorithm such as SIFT or SURF on lunar images to find out which lunar surface characteristics (seas, craters, etc.) present the most robust source of features to use for angle measurements. Investigate feature detection and extraction performance under different visibility scenarios such as moon phases, occlusion, librations, etc.

Bibliography

1. *Industry: A Monthly Magazine Devoted to Science, Engineering and Mechanic Arts.* nos. 54-65. 1893.

2. Alkhaldi, Humood. *Integration of a Star Tracker and Inertial Sensors Using an Attitude Update.* Masters thesis, Air Force Institute of Technology, Sept 2014.

3. Anderson, E.W. “navigation.”, Encyclopedia Britannica Inc., 2013. `http://www.britannica.com/EBchecked/topic/407011/navigation`.

4. Bandeira, L., J. Saraiva, and P. Pina. “Impact Crater Recognition on Mars Based on a Probability Volume Created by Template Matching”. *Geoscience and Remote Sensing, IEEE Transactions on*, 45(12):4008–4015, Dec 2007.

5. Brown, R.G. and P.Y.C. Hwang. *Discrete Kalman Filter Basics, 4th Edition.* J. Wiley and Sons, 2012.

6. Chu, Zhu D.Q. Udomkesmalee G., C. and M.I. Pomerantz. “Realization of autonomous image-based spacecraft pointing systems: planetary flyby example”. *Proc. SPIE*, 2221:27–40, 1994.

7. DeAntonio, Udomkesmalee G. Alexander J.W. Blue R.C. Dennison E.W. Sevaston G.E., L. and M. Scholl. “Star-tracker-based, all-sky, autonomous attitude determination”. *Proc. SPIE*, 1949:204–215, 1993.

8. Enright, John. “Moon-Tracking Modes for Star Trackers”. *Journal of Guidance, Control, and Dynamics*, 33(1):171–185, 2010.

9. Groves, P.D. *Principles of GNSS, Inertial, and Multisensor Integrated Navigation Systems.* GNSS technology and applications series. Artech House, 2008.

10. Hecht, E. *Optics*. Pearson Education. Addison-Wesley, 2002.

11. Heiken, G., D. Vaniman, and B.M. French. *Lunar Sourcebook: A User's Guide to the Moon*. Cambridge University Press, 1991.

12. Kaplan, E. and C. Hegarty. *Understanding GPS: Principles and Applications, Second Edition*. Artech House, 2005.

13. Kauffman, Kyle J. *RADAR Based Navigation in Unknown Terrain*. Ph.D. thesis, Air Force Institute of Technology, Dec 2012.

14. Leroy, Bertrand, Gérard Medioni, E Johnson, and Larry Matthies. "Crater detection for autonomous landing on asteroids". *Image and Vision Computing*, 19(11):787–792, 2001.

15. Liebe, Carl C. "A New strategy for Tracking Planetary Terrains". *Proc. SPIE*, 2221:41–55, 1994.

16. Liebe, C.C. "Pattern recognition of star constellations for spacecraft applications". *Aerospace and Electronic Systems Magazine, IEEE*, 8(1):31–39, Jan 1993.

17. Liebe, C.C. "Tracking of planetary terrains". *Aerospace and Electronic Systems Magazine, IEEE*, 9(2):9–18, Feb 1994.

18. Liebe, C.C. "Star Trackers for Attitude Determination". *Aerospace and Electronic Systems Magazine, IEEE*, 10(6):10–16, Jun 1995.

19. Liebe, C.C., S. Mobasser, Y. Bae, C.J. Wrigley, J.R. Schroeder, and A.M. Howard. "Micro Sun sensor". *Aerospace Conference Proceedings, 2002. IEEE*, volume 5, 5–2263–5–2273 vol.5. 2002.

20. Maybeck, Peter S. *Stochastic Models, Estimation, and Control, Vol I.* Mathematics in Science and Engineering. Academic Press, Inc., 1979.

21. Maybeck, Peter S. *Stochastic Models, Estimation, and Control, Vol 2.* Mathematics in Science and Engineering. Academic Press, Inc., 1982.

22. Mclendon, James W. "Information Warfare: Impacts and Concerns". *Battlefield of the Future (21st Century Warfare Issues, Air War College Studies in National Security No. 3)*, (3):185–186, Sept 1998.

23. Mortari, Daniele. "Moon-Sun attitude sensor". *Journal of spacecraft and rockets*, 34(3):360–364, 1997.

24. Park, Keunjoo and Daniele Mortari. "Planet or Moon image processing for spacecraft attitude estimation". *Journal of Electronic Imaging*, 17(2):023020–023020–11, 2008.

25. Rip, M.R., J.M. Hasik, and Naval Institute Press. *The Precision Revolution: GPS and the Future of Aerial Warfare.* Naval Institute Press, 2002.

26. Robinson, M. "LROC Lunar Near Side Image", Arizona State University, 2010. `http://wms.lroc.asu.edu/lroc/view_rdr/WAC_GLOBAL`.

27. Simonsen, K.S., D. Nathans, M.L. Suycott, J. Wohlfiel, A. Turner, and B. Crumplar. "GPS: Our Strongest Ally or Weakest Link?" *CHIPS-the Department of the Navy Information Technology Magazine*, Spring 2002.

28. Titterton, D., J.L. Weston, and Institution of Electrical Engineers. *Strapdown Inertial Navigation Technology, 2nd Edition.* IEE radar, sonar, navigation, and avionics series. Institution of Engineering and Technology, 2004.

29. Udomkesmalee, G. and L. DeAntonio. "Detection of planetary terrain features". *Proc. SPIE*, 2466:31–40, 1995.

30. Veth, Michael J. *Fusion of Imaging and Inertial Sensors for Navigation*. Ph.D. thesis, Air Force Institute of Technology, Sept 2006.

31. Williams, D.R. "Earth Fact Sheet", NASA, June 2013. `http://nssdc.gsfc.nasa.gov/planetary/factsheet/earthfact.html`.

32. Williams, D.R. "Sun Fact Sheet", NASA, June 2013. `httphttp://nssdc.gsfc.nasa.gov/planetary/factsheet/sunfact.html`.

33. Williams, D.R. "Moon Fact Sheet", NASA, April 2014. `http://nssdc.gsfc.nasa.gov/planetary/factsheet/moonfact.html`.

34. Williams, J.E.D. *From Sails to Satellites*. Oxford University Press, 1992.

REPORT DOCUMENTATION PAGE

Form Approved
OMB No. 0704–0188

1. REPORT DATE *(DD–MM–YYYY)*	**2. REPORT TYPE**	**3. DATES COVERED** *(From — To)*
26–03–2015	Master's Thesis	Oct 2013 — Mar 2015

4. TITLE AND SUBTITLE

Theoretical Limits of Lunar Vision Aided Navigation with
Inertial Navigation System

5a. CONTRACT NUMBER

5b. GRANT NUMBER

5c. PROGRAM ELEMENT NUMBER

6. AUTHOR(S)

Jones, David W., Captain, USAF

5d. PROJECT NUMBER

5e. TASK NUMBER

5f. WORK UNIT NUMBER

7. PERFORMING ORGANIZATION NAME(S) AND ADDRESS(ES)

Air Force Institute of Technology
Graduate School of Engineering and Management (AFIT/EN)
2950 Hobson Way
WPAFB OH 45433-7765

8. PERFORMING ORGANIZATION REPORT NUMBER

AFIT-ENG-MS-15-M-020

9. SPONSORING / MONITORING AGENCY NAME(S) AND ADDRESS(ES)

Intentionally left blank

10. SPONSOR/MONITOR'S ACRONYM(S)

11. SPONSOR/MONITOR'S REPORT NUMBER(S)

12. DISTRIBUTION / AVAILABILITY STATEMENT

Distribution Statement A: Approved for Public Release; Distribution Unlimited.

13. SUPPLEMENTARY NOTES

This material is declared a work of the U.S. Government and is not subject to copyright protection in the United States.

14. ABSTRACT

The precision navigation capabilities of the Global Positioning System (GPS) are used extensively within US military operations. However, GPS is highly vulnerable to intentional and unintentional external interference. Therefore, a need exists to develop a non-GPS precision navigation method to operate in GPS degraded environments. This research effort presents the theoretical limits of a precision navigation method based on an inertial navigation system (INS) aided by angle measurements with respect to lunar surface features observed by a fixed camera. To accomplish this task, an extended Kalman filter (EKF) was implemented to estimate INS drift errors and bring in simulated lunar feature angle measurements to correct error estimates. The research scope focused solely on the feasibility of lunar vision aided navigation with INS where only measurement noise effects from a simulated CCD camera and barometer were considered. Various scenarios based on camera specifications, lunar feature quantity, INS grade, and lunar orbital parameters were conducted to observe the INS drift correction by lunar feature angle measurements. The resulting trade spaces presented by the scenarios showed theoretical substantial improvement in the navigation solution with respect to a stand alone INS.

15. SUBJECT TERMS

Navigation, Lunar, INS, EKF, Computer Vision

16. SECURITY CLASSIFICATION OF:			**17. LIMITATION OF ABSTRACT**	**18. NUMBER OF PAGES**	**19a. NAME OF RESPONSIBLE PERSON**
a. REPORT	**b. ABSTRACT**	**c. THIS PAGE**			Dr. Kyle J. Kauffman (ENG)
					19b. TELEPHONE NUMBER *(include area code)*
U	U	U	U	126	(937) 255-3636, x4683; kyle.kauffman@afit.edu

Standard Form 298 (Rev. 8–98)
Prescribed by ANSI Std. Z39.18